Combined computational-experimental study on plasma and plasma catalysis for N_2 fixation

Hamid Ahmadi Eshtehardi

Dissertation submitted for the degree of Doctor in Engineering Sciences and Technology and Doctor in Science: Chemistry

Promotors: Prof. Dr. Annemie Bogaerts and Prof. Dr. Marie-Paule Delplancke

University of Antwerp
Faculty of science
Department of Chemistry

ULB ECOLE POLYTECHNIQUE DE BRUXELLES
École polytechnique de Bruxelles
4MAT department

To my little Ario

Table of contents

List of abbreviations

1D	One-dimensional
2D	Two-dimensional
3D	Three-dimensional
ADM	Axial dispersion model
APGD	Atmospheric pressure glow discharge
ATP	Adenosine triphosphate
a_v	External surface area per unit volume of the catalyst ($\mathrm{m}^2\ \mathrm{m}^{-3}$)
A_{bed}	Cross section surface area of the catalyst bed (m^2)
A_r	Reactor cross section surface area (m^2)
BASF	Baden Aniline and Soda Company
CAS	Cryogenic air separation
CAPEX	Capital expenditure
CEJ	Chemical Engineering Journal
CSTR	Continuously stirred-tank reactor
C	Concentration ($\mathrm{mol\ m}^{-3}$)
C_0	Concentration at time zero ($\mathrm{mol\ m}^{-3}$)
C_i	Concentration of species *i* in the gas phase ($\mathrm{mol\ m}^{-3}$)
$C_{i,s}$	Concentration of species *i* in the solid phase ($\mathrm{mol\ m}^{-3}$)
C_{pg}	Heat capacity of the gas phase ($\mathrm{J kg}^{-1}\mathrm{K}^{-1}$)
$C_{p,bed}$	Heat capacity of the catalyst bed ($\mathrm{J kg}^{-1}\mathrm{K}^{-1}$)
C_T	Number of sites per unit volume of the catalyst
DBD	Dielectric barrier discharge
DC	Direct current

DNA	Deoxyribonucleic acid
DRM	Dry reforming of methane
D_z	Axial dispersion coefficient ($\mathrm{m^2 s^{-1}}$)
D_p	Equivalent spherical diameter of the packing (m)
D_m	Average molecular diffusivity ($\mathrm{m^2 s^{-1}}$)
D_i	Effective diffusion coefficient ($\mathrm{m^2 s^{-1}}$)
D_{Amix}	Molecular diffusion coefficient of species *A* in the gas mixture ($\mathrm{m^2 s^{-1}}$)
D_{AB}	Binary molecular diffusion coefficient ($\mathrm{m^2 s^{-1}}$)
D_{Kn}	Knudsen's diffusion coefficient ($\mathrm{m^2 s^{-1}}$)
d_{pore}	Diameter of catalyst pores (m)
d_p	Diameter of catalyst particles (m)
d_{bed}	Diameter of the catalyst bed (m)
d_r	Reactor diameter (m)
EC	Energy cost ($\mathrm{MJ mol^{-1}}$)
EEDF	Electron energy distribution function
$E(t)$	Residence time distribution function
E_a	Activation energy (eV)
F_{A0}	Molar flow rate of species A into the reactor ($\mathrm{mol\ s^{-1}}$)
F_A	Molar flow rate of species A out of the reactor ($\mathrm{mol\ s^{-1}}$)
f_p	Fixed bed friction factor
GA	Gliding arc
G_{rp}	Modified Reynolds' number of the fixed bed
G_s	Mass velocity of the gas phase ($\mathrm{kg\ m^{-2} s^{-1}}$)
HB	Haber-Bosch

HV	High voltage
h_f	Heat transfer coefficient ($\mathrm{W\ m^{-2}K^{-1}}$)
IC	Integrated circuit
ICP	Inductively coupled plasma
IPCC	Intergovernmental Panel on Climate Change
$j_{D,i}$	Chilton-Colburn's factor for mass transfer
j_H	Chilton-Colburn's factor for heat transfer
$k_{g,i}$	Gas-to-solid mass transfer coefficient ($\mathrm{m^{-3}m^{-2}s^{-1}}$)
k_f	Forward reaction rate coefficient
k_r	Backward reaction rate coefficient
LPG	Liquified petroleum gas
LTE	Local thermal equilibrium
L	Length of the catalyst bed (m)
MFC	Mass flow controller
MFM	Mass flow meter
MW	Microwave
M	Molecular weight ($\mathrm{g\ mol^{-1}}$)
NDIR	Non-dispersive infrared
NDUV	Non-dispersive ultraviolet
NF	Nitrogen fixation
Nu	Nusselt's number
P	Power (W)
PB	Packed bed
PDE	Partial differential equation

Pe	Peclet's number
Pe_{cell}	Peclet's number in the calculation cell
PFR	Plug flow reactor
PR	Production rate ($\mathrm{g\ h^{-1}}$)
PSU	Power supply unit
Pr	Prandtl number
p	Pressure (Pa)
p°	Standard pressure (Pa)
$\bar{p}_i$	Partial pressure of species i (Pa)
$\bar{p}_i^{inst.}$	Instantaneous partial pressure of species i (Pa)
q_{in}	Inlet gas volumetric flow rate ($\mathrm{m^3 s^{-1}}$)
q	Actual gas volumetric flow rate ($\mathrm{m^3 s^{-1}}$)
Q	total gas volumetric flow rate ($\mathrm{L min^{-1}}$)
RE	Renewable energy
RET	Renewable energy transition
RF	Radio-frequency
RGA	Rotating gliding arc
RNA	Ribonucleic acid
RTD	Residence time distribution
$-r_A$	Reaction rate of species A ($\mathrm{mol\ m^{-3} s^{-1}}$)
r_i^{gas}	Rate of formation or destruction of species *i* in the gas phase ($\mathrm{mol\ m^{-3} s^{-1}}$)
r_i^{s}	Rate of formation or destruction of species *i* in the solid phase ($\mathrm{mol\ m^{-3} s^{-1}}$)
r_p	Radius of the catalyst particle (m)
R_j	Rate of reaction of species *i* ($\mathrm{mol\ m^{-3} s^{-1}}$)

R	Universal gas constant ($\mathrm{Pa\ m^3 mol^{-1} K^{-1}}$)
Re	Reynolds number
SEI	Specific energy input ($\mathrm{kJl^{-1}}$)
SOTA	State-of-the-art
S	Number of active sites on the catalyst surface (mol)
Sh	Sherwood's number
Sc	Schmidt's number
St	Stanton number
TISM	Tank In series model
TS	Transition state
t	Time (s)
t_{res}	Residence time (s)
T_s	Surface temperature of the catalyst (K)
$T°$	Standard temperature (K)
T_g	Gas temperature (K)
T_v	Vibrational temperature (K)
T_i	Ion temperature (K)
T_r	Rotational temperature (K)
T_e	Electron temperature (K)
u_s	Gas superficial velocity ($\mathrm{m\ s^{-1}}$)
VDF	Vibrational distribution function
V_p	Total volume of the catalyst particles ($\mathrm{m^3}$)
V_t	Total volume of the catalyst bed ($\mathrm{m^3}$)
WIPO	World Intellectual Property Organization

X	Conversion
x_i	Fraction of species i in the gas phase
z	Position from the inlet of the catalyst bed (m)

Greek letters

δ	Dirac's delta function
ε_b	Catalyst bed void fraction (porosity)
η_j	Effectiveness factor of reaction *j*
λ_z^f	Effective thermal conductivity $(\mathrm{W\ K^{-1}})$
λ_g	Average gas thermal conductivity $(\mathrm{W\ K^{-1}})$
λ_z^0	Axial thermal conductivity $(\mathrm{W\ K^{-1}})$
λ_g	Solid thermal conductivity $(\mathrm{W\ K^{-1}})$
μ_g	Gas dynamic viscosity $(\mathrm{kg\ m^{-1}s^{-1}})$
ρ_g	Gas phase density $(\mathrm{kg\ m^{-3}})$
ρ_{bed}	Density of the catalyst bed $(\mathrm{kg\ m^{-3}})$
ΔH_{rxn}	Enthalpy of reaction $(\mathrm{J\ mol^{-1}})$
ΔS°	Standard entropy of reaction $(\mathrm{J\ K^{-1}})$
$\Delta G°$	Standard Gibbs free energy $(\mathrm{J\ mol^{-1}})$
ΔP	Pressure drop (Pa)
τ_{cat}	Catalyst tortuosity
τ	Dimensionless time
$\Sigma_i \nu_i$	Special atomic diffusion volumes
ζ	Dimensionless position from the inlet of the catalyst bed
ϕ	Thiele's modulus

Summary

Molecular nitrogen forms 78% of the earth's atmosphere, and therefore, it is the most abundant molecule in the atmosphere; however, it is not directly accessible for living organisms for production of essential substances needed for life, and it must be dissociated into its atomic form. The process of converting nitrogen into the form that can be used by living organisms is called nitrogen fixation, which in nature occurs in the global nitrogen cycle. Since the manifestation of the industrial era, numerous industrial chemical technologies have been developed. Fertilizer production through the Haber-Bosch process (one of the greatest human inventions during the industrial revolution), has significantly contributed to the food production industry and has revolutionized the modern society. Simultaneously, the Haber-Bosch process is one of the biggest contributors to the emission of industrially produced greenhouse gases, which have resulted in climate change and its irreversible negative effects on the environment and human health. Therefore, there is a need to find a sustainable solution for such processes to slow down the global warming.

Plasma technology is very modular and can operate in moderate conditions. Additionally, it activates gas molecules by high energy electrons instead of heat, and it can convert intermittent renewable electricity into value added chemicals. Last but not least, the possibility of integrating plasma with a catalyst in "plasma catalysis" enables the selective production of desired products and can lead to improvements in the process efficiency. Therefore, in the past few years, plasma technology has started to be considered as a green alternative for fossil-based gas conversion processes. However, the industrialization of this process faces several challenges, such as the need for better insight in plasma-catalyst interactions, high energy consumption, as well as challenges for the development of industrial scale efficient reactors. In the framework of this thesis, we have tried to add to the state-of-the-art in plasma-based nitrogen fixation, by dealing with these three challenges, using a combined experimental and modelling work.

We start this thesis with a general introduction in chapter 1. In chapter 2, we discuss ideal chemical reactors, the concept of residence time distribution function in such reactors, and how to quantify the deviation of a real reactor from ideal conditions using the concept of back-mixing degree. Later, we introduce a 1D heterogeneous catalysis model with axial dispersion for a packed bed reactor and derive the governing equation of such a model (i.e., mass and energy balance in the gas and solid phase, as well as momentum balance across the catalyst bed). This chapter is closed by providing numerical correlations for the calculation of physical parameters used in this model.

In chapter 3, we apply such a model to the post-plasma catalytic stage of a radio-frequency inductively coupled plasma (RF-ICP) reactor for NO production, aiming to reveal the underlying mechanisms that are responsible for NO production in this reactor and investigate the effect of different operating conditions on the efficiency of the process. we investigate the effect of post-

plasma gas composition on the NO concentration in the gas phase, and my model shows that a higher O_2 fraction in the feed gas and N_2 dissociation fraction in the post-plasma gas flow result not only in a higher NO concentration, but also in a significant improvement in the energy cost of NO formation calculated by my model. Additionally, my simulations reveal the importance of designing a catalytic bed reactor resembling as much as possible a plug flow reactor. Finally, it shows how increasing the catalyst bed characteristic length and catalyst bed porosity also results in a higher NO concentration at the reactor outlet and a lower energy cost of NO formation.

In chapter 4, we present a design modification to a rotating gliding arc plasma reactor for NO_x (i.e., NO and NO_2) production, by coupling it with a specific nozzle, so-called "effusion nozzle", aiming to improve the energy cost of NO_x production in this reactor. Experimentally, my results show that coupling this reactor with this specific type of nozzle leads to 8% enhancement in the NO_x concentration at the reactor outlet, as well as 22.5% reduction in the process energy cost. In absolute terms we produce NO_x concentrations up to 5.9% at an energy cost down to 2.1 MJ/mol. Note that these values were the best results, at the date of my studies, for nitrogen fixation into NO_x at atmospheric pressure. However, these results are still far from the energy cost of 1.1-1.5 MJ/mol that is required for plasma-based nitrogen fixation to be competitive with current cost-efficient fossil-based processes. Nevertheless, they clearly show that improving the energy efficiency of plasma reactors is feasible through reactor design optimization.

In chapter 5, my colleague (Ivan Tsonev) and I try to tackle the challenge of upscaling plasma-based nitrogen fixation by developing a low current, high flow rate plasma reactor and we compare its results to its smaller counterpart operating with the same principle. In this way we scan a large range of specific energy input (SEI) and investigate the potential for upscaling the nitrogen fixation process. We observe two different trends of energy cost with SEI, and therefore, we apply a simple mathematical approach, based on thermodynamic equilibrium calculations, to estimate the flow rate passing through the plasma, as well as the gas temperature, in order to better explain our experimental observations. Experimentally, we achieve the lowest energy cost of 2.8 MJ/mol for NO_x production from air, which according to our thermodynamic equilibrium calculations is very close to the thermodynamic minimum (i.e., 2.7 MJ/mol for NO_x production from air).

Finally, in chapter 6, we close the thesis with a general conclusion to the previous chapters and suggest some topics for further investigation of plasma-based nitrogen fixation. In summary, in this thesis, we use a combination of mathematical and experimental approaches to tackle the challenges on the way for industrialization of plasma-based nitrogen fixation and we show that further improvement in this technology is feasible, although it still needs further effort, and this technology is a key potential for electrification of the chemical industry.

Samenvatting

Moleculaire stikstof vormt 78% van de atmosfeer van de aarde en is daardoor de meest voorkomende molecule in de atmosfeer; het is echter niet direct toegankelijk voor levende organismen voor de productie van essentiële stoffen die nodig zijn voor het leven, en het moet worden ontbonden tot zijn atomaire vorm. Het proces van het omzetten van stikstof in de vorm die door levende organismen kan worden gebruikt, wordt stikstoffixatie genoemd, wat in de natuur plaatsvindt in de wereldwijde stikstofcyclus. Sinds het begin van het industriële tijdperk zijn talloze industriële chemische technologieën ontwikkeld door de mens. De productie van kunstmest via het Haber-Bosch-proces (een van de grootste menselijke uitvindingen tijdens de industriële revolutie) heeft aanzienlijk bijgedragen aan de voedselproductie-industrie en heeft de moderne samenleving gerevolutioneerd. Tegelijkertijd is het Haber-Bosch-proces een van de grootste bijdragers aan de uitstoot van door de industrie geproduceerde broeikasgassen, die hebben geleid tot klimaatverandering en de onomkeerbare negatieve effecten op het milieu en de menselijke gezondheid. Daarom is er behoefte aan een duurzame oplossing voor dergelijke processen om de opwarming van de aarde te vertragen.

Plasmatechnologie is zeer modulair en kan werken onder milde omstandigheden. Bovendien activeert het gasmoleculen door middel van hoogenergetische elektronen in plaats van warmte, en het kan het fluctuerende hernieuwbare elektriciteit omzetten in waardevolle chemicaliën. Tenslotte maakt de mogelijkheid om plasma te integreren met een katalysator in "plasma-katalyse" de selectieve productie van gewenste producten mogelijk en kan het leiden tot verbeteringen in de procesefficiëntie. Daarom wordt plasmatechnologie de laatste jaren beschouwd als een groen alternatief voor gasconversieprocessen gebaseerd op fossiele brandstoffen. De industrialisatie van dit proces wordt echter geconfronteerd met een aantal uitdagingen, zoals nood aan beter inzicht in de fundamentele interactie tussen plasma en katalysator, hoog energieverbruik, evenals uitdagingen bij de ontwikkeling van efficiënte reactoren op industriële schaal. In het kader van deze scriptie hebben we geprobeerd bij te dragen aan de stand van zaken in plasma-gebaseerde stikstoffixatie, door de drie bovenstaande uitdagingen aan te pakken, met behulp van een gecombineerde experimentele en modelleringsaanpak.

We begin deze scriptie met een algemene inleiding in hoofdstuk 1. In hoofdstuk 2 bespreek we ideale chemische reactoren, het concept van de verdelingsfunctie van de verblijftijd in dergelijke reactoren, en hoe men de afwijking van een echte reactor van ideale omstandigheden kan kwantificeren met behulp van het concept van “mengingsgraad. Vervolgens introduceer we een 1D heterogeen katalysemodel met axiale dispersie voor een gepakte bedreactor en leid we de algemene vergelijking van een dergelijk model af (d.w.z. massabalans en energiebalans in de gas- en vaste fase, evenals impulsbalans over het katalysatorbed). Dit hoofdstuk wordt afgesloten door numerieke correlaties te verstrekken voor de berekening van fysische parameters die in dit model worden gebruikt.

In hoofdstuk 3 pas we zo'n model toe op de post-plasmakatalytische fase van een radiofrequent inductief gekoppeld plasma (RF-ICP) reactor voor de productie van stikstofmonoxide (NO), met als doel de onderliggende mechanismen die verantwoordelijk zijn voor de NO-productie in deze reactor bloot te leggen en het effect van verschillende bedrijfsomstandigheden op de efficiëntie van het proces te onderzoeken. We onderzoeken het effect van de samenstelling van het post-plasmagas op de NO-concentratie in de gasfase, en onze model toont aan dat een hoger O_2-gehalte in het toevoergas en een hogere N_2-dissociatiefractie in de post-plasmagasstroom niet alleen leiden tot een hogere NO-concentratie, maar ook tot een aanzienlijke verbetering van de energiekosten van NO-vorming zoals berekend door onze model. Bovendien tonen onze simulaties het belang aan van het ontwerpen van een katalytische bedreactor, die zoveel mogelijk lijkt op de omstandigheden van een plug flow reactor. Tot slot laten ze zien hoe het vergroten van de kenmerkende lengte en porositeit van het katalysatorbed ook leidt tot een hogere NO-concentratie aan de uitlaat van de reactor en lagere energiekosten voor NO-vorming.

In hoofdstuk 4 presenteer we een ontwerpaanpassing aan een roterende glijdende boogplasmareactor voor de productie van NO_x (dwz NO en NO_2), door deze te koppelen aan een specifieke nozzle, genaamd "effusienozzle", met als doel de energiekosten van NO_x-productie in deze reactor te verbeteren. Experimenteel laten onze resultaten zien dat het koppelen van deze reactor aan dit specifieke type nozzle leidt tot een verbetering van 8% in de NO_x-concentratie aan de uitlaat van de reactor, evenals een vermindering van 22,5% in de procesenergiekosten. In absolute termen produceer we NO_x-concentraties tot 5,9% bij een energiekost van slechts 2,1 MJ/mol. Merk op dat dit tot nu toe de beste resultaten waren in onze onderzoek naar stikstoffixatie tot NO_x bij atmosferische druk. Desalniettemin blijven deze resultaten nog duidelijk verwijderd van de energiekost van 1,1-1,5 MJ/mol die nodig is voor plasma-gebaseerde stikstoffixatie om te kunnen concurreren met de huidige kostenefficiënte processen gebaseerd op fossiele brandstoffen. Niettemin laten ze duidelijk zien dat het mogelijk is om de energie-efficiëntie van plasmareactoren te verbeteren door optimalisatie van het reactorontwerp.

In hoofdstuk 5 proberen mijn collega (Ivan Tsonev) en ikzelf het probleem van het opschalen van plasma-gebaseerde stikstoffixatie aan te pakken door een plasmareactor met een lage stroomsterkte en een hoge debietsnelheid te ontwikkelen, en we vergelijken de resultaten met zijn kleinere tegenhanger die op hetzelfde principe werkt. Op deze manier bestrijken we een groot bereik van SEI (specifieke energie-input) en onderzoeken we het potentieel om het stikstoffixatieproces op te schalen. We observeren twee verschillende trends in de energiekosten met betrekking tot SEI, en daarom passen we een eenvoudige wiskundige benadering toe, gebaseerd op thermodynamische evenwichtsberekeningen, om de stroomsnelheid door het plasma en de gastemperatuur te schatten, en zo onze experimentele waarnemingen beter te verklaren. Experimenteel behalen we de laagste energiekosten van 2,8 MJ/mol voor de productie van NO_x uit lucht, wat volgens onze thermodynamische evenwichtsberekeningen zeer dicht bij het thermodynamische minimum ligt (namelijk 2,7 MJ/mol voor de productie van NO_x uit lucht).

Ten slotte sluit we in hoofdstuk 6 de scriptie af met een algemene conclusie van de voorgaande hoofdstukken en stel we enkele onderwerpen voor voor verder onderzoek naar plasma-gebaseerde stikstoffixatie. Samengevat gebruik ik in deze scriptie een combinatie van wiskundige en experimentele benaderingen om de uitdagingen op weg naar de industrialisatie van plasma-gebaseerde stikstoffixatie aan te pakken, en we toonen aan dat verdere verbeteringen in deze technologie mogelijk zijn, zij het met verdere inspanning. Deze technologie is een belangrijk potentieel voor de elektrificatie van de chemische industrie.

1 Introduction

1.1 Nitrogen: History, importance for life and its natural fixation process

Historically, nitrogen-containing compounds, like “royal water”, were known since ancient Greece and the middle ages [1]. Nitrogen-containing compounds, such as potassium nitrate, were used in gunpowder production, forming one of the early applications of nitrogen compounds [2]. An air component uncapable of sustaining combustion was found, for the first time, in the research of Daniel Rutherford named as “noxious gas”, however, he did not distinguish that this component is composed of two atomic nitrogen that we know it today as a separate element [3]. In modern chemistry, nitrogen is known as a non-metal element with the atomic number 7, which belongs to group 15 of the periodic table. Molecular nitrogen forms 78% of the earth’s atmosphere, and therefore, it is the most abundant molecule in the atmosphere [4]. Atomic nitrogen is also one of the key components of proteins and genetic materials like DNA and RNA, making it a vital element for all living organisms [5].

The earth’s atmosphere is rich in molecular nitrogen; however, it is only the nitrogen in its atomic form that can be used by plants and animals for the production of proteins and genetic materials, hence, the atmospheric nitrogen cannot be directly used by living organisms [5]. The reason is the high energy barrier of nitrogen dissociation (i.e., 9.74 eV) [6,7]. The process in which the gas phase molecular nitrogen is converted into nitrogen atoms, hence making it accessible for plants and animals, is referred to as nitrogen fixation (NF) [5].

In nature, the NF process (i.e., the transfer of nitrogen from the atmosphere to plants and animals) occurs in the natural nitrogen cycle, and lightning strikes fix around 3 to 10 billion kilograms of nitrogen every year [8]. Additionally, bacteria, either aerobic or anaerobic, are also main agents of natural fixation of nitrogen in plants [5]. They attract these bacteria through the nodules in their roots where the molecular nitrogen is fixed using an enzyme called nitrogenase [5]. An example of NF nodules on a plant root is presented in Figure 1.1.

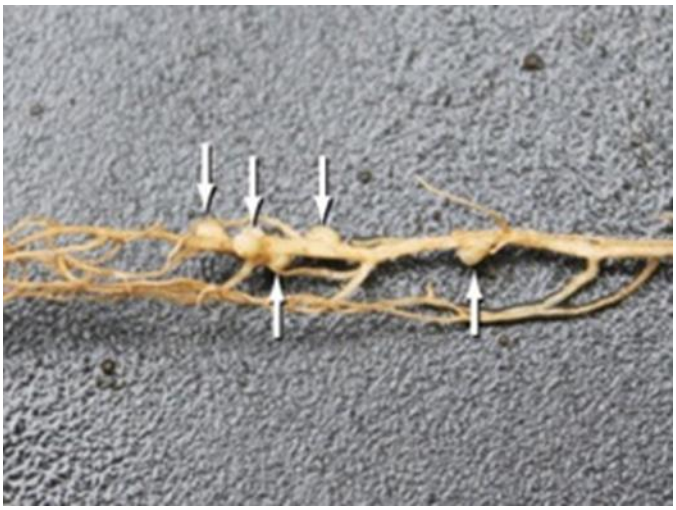

Figure 1.1. Nodules responsible for nitrogen fixation in plant roots. Adopted from [5].

1.2 Artificial nitrogen fixation by the Haber-Bosch Process: history, achievements, and challenges

Since the 1950s, the world population has rapidly grown from 2.5 billion to 7.98 billion in 2022, and according to estimations, the world population will be around 10.35 billion people by 2100 [9]. The Haber-Bosch (HB) process, invented in the first half of the 20th century, i.e., the start of the industrial production of fertilizers, was a main contributor to this rapid population raise [10]. A brief story behind the development of the HB process, which was a result of several years of research, cooperation and technical development, is presented below [11].

Decomposition of ammonia at high temperature under atmospheric pressure conditions, was the main obstacle that renowned scientists, such as W. H. Nernst, W. Ostwald, etc., were facing during their several years of research for using nitrogen and hydrogen to produce ammonia [11]. The concept of reaction rate, proposed for the first time by F. Haber, enabled the development of closed loop processes, which resulted in the invention of the world first pressurized catalytic process for ammonia production [11]. Because of this remarkable invention, Haber was awarded the Nobel Prize of Chemistry in 1919 [11]. Afterwards, extensive experimental research was conducted by Carl Bosch and his colleagues at Baden Aniline and Soda Company (BASF) aiming to find a suitable catalyst for ammonia production, and after several years of research, they found a catalyst mixture which could significantly improve the efficiency of catalytic ammonia production [11]. This resulted in the Nobel Prize of Chemistry for Carl Bosch because of his contribution in developing high-pressure chemical processes including ammonia synthesis [11]. Estimations of the United Nations Food and Agriculture Organization (FAO) state that more than 40% of the global food production is attributed to the use of fertilizers, and it is the origin of 50% of the nitrogen in our body [11,12]. This highlights the important influence of the HB process on

modern-day society, which has enabled human beings to produce more than enough food using the resource on earth [11].

In addition to fertilizers, ammonia finds applications as a green fuel in transportation and power generation, as well as in the military industry for the production of explosives [10,13,14]. Using ammonia, as a green fuel, enables the possibility to transport around 1.5 times more energy using the already developed infrastructures for transportation of liquified petroleum gas [14,15]. Additionally, the produced ammonia from the HB process can be oxidized to NO and NO_2 (by further oxidation of NO) in the Ostwald process, and dissolving the formed NO_2 in water leads to the production of nitric acid (HNO_3), which can again react with ammonia to form ammonium nitrate that has a broad application, ranging from fertilizers to explosives [16,17].

Nowadays the fossil-based production of reactive nitrogen by human beings is almost 10 times higher than their actual demand and this human activity has resulted in a large perturbation in the natural nitrogen cycle [18–21]. As a result, it can be argued that, despite the large positive impacts of the invention of fossil-based processes, like the HB process, they have also resulted in huge damages to the environment and human health [21]. 95% of the hydrogen production, required for industrial processes, is fossil based, resulting in the emission of a tremendous amount of greenhouse gases into the atmosphere [13]. Annually 400 Mt of CO_2 is emitted to the atmosphere by the HB process, meaning that this process is responsible for 1.2-1.5% of the global industrial CO_2 emissions [13,22]. Furthermore, since the HB process operates at high pressure and temperature, it consumes 30 GJ of energy per ton of ammonia, which accounts for the consumption of about 1-2% of the worldwide produced energy per annum [13,23,24].

1.3 Necessity of the transition to renewable energies

Utilization of renewable energies (REs) such as wind energy, for the movement of sail ships and operation of wind mills, dates back to ancient ages [25–27]. This period continued until the occurrence of the industrial revolution [27–29]. Industrial revolution is a period starting from the mid-18th century until today, during which significant technological advancements have occurred in the human civilization and can be divided into three different phases. The first industrial revolution started from the mid-18th century by the invention of steam engines and machine tools that significantly increased the efficiency of industries compared to before [30,31]. High capacity manufacturing of iron, the development of complex railroad networks, and introducing the telegraph and petroleum into the industry resulted in the manifestation of the technological revolution, starting from the late 19th century to the late 20th century [32]. Finally, advancements and innovations such as metal-oxide semiconductor field-effect transistors (MOSFET transistors) and integrated circuit (IC) chips, which helped in the development of micro-processors, computers and mobile phones, formed the basis of the digital revolution since the late 20th century until present, which is also referred to as the third industrial revolution [33].

From the perspective of cost efficiency, renewable energy based processes, because of the intermittent supply of REs, could not compete with the fossil-based technologies developed during the industrial revolution [27]. However, the accomplishments achieved through the industrial revolution led to significant malicious influences on the world's climate as a result of the large scale fossil fuel utilization [34]. A rapid rise of the global temperature was the outcome of intense human activities, which led to the emission of enormous amounts of greenhouse gases into the atmosphere through fossil-based processes developed in the industrialization era [34,35]. The energy demand becomes higher with increasing world population, and to slow down this demand and its subsequent effects on the global warming and energy security, human society feels the need for a shift to sustainable energies, which is called the renewable energy transition (RET) [36]. However, a successful RET has become one of the biggest challenges of the present century due to the reluctance of investors to invest in the REs market as one of the main reasons [37,38]. One of the most important measures for RET which is being followed by western countries, especially by the European commission, is the "*electrification of the process industry*", in which the main goal is the substantial reduction of greenhouse gases using the electrical power produced through REs [39–41].

1.4 Plasma Technology: A potential approach toward electrification of the chemical industry

In section 1.3, it was discussed that, due to the intense human activities, tremendous amounts of greenhouse gases are released in the atmosphere, resulting in climate changes [34]. Consequently, to slow down these negative effects, human society needs to shift from fossil-based to sustainable technologies [36]. To reach this goal, various innovative technologies such as plasma technology are suggested by scientists as alternatives for fossil-based processes [42]. Plasma is an intriguing approach for gas conversion as it operates at moderate operational conditions, activates gas molecules by high-energy electrons instead of heat, and is capable of converting the intermittent renewable electricity into value-added chemicals [42,43]. Additionally, the fast on/off characteristic of plasma and its possibility of integration with a catalyst, in so-called "*plasma catalysis*", introduces the flexibility of plasma for gas conversion at decentralized locations and for the selective production of chemicals, respectively [42,43].

Plasma is referred to as the "*fourth state of the matter*", and forms about 99% of the matter in the cosmos [44]. More specifically, plasma can be defined as an ionized gas with ionization degree ranging between 10^{-6}% (i.e., partially ionized gas) to 100% (i.e., fully ionized gas) [42,45]. Atoms, molecules, radicals, electronic, and vibrationally excited species are all present in partially ionized plasmas, making it a reactive medium suitable for various applications [42,45,46]. Based on the concept of thermal equilibrium, plasmas can be categorized as thermal or non-thermal, of which the characteristics are discussed in more detail in section 1.5 [42,45]. There is also a third category, the so called "*warm plasmas*", that has the properties of both thermal and non-thermal plasmas [17,42].

1.5 Thermal, non-thermal and warm plasmas for nitrogen fixation

As mentioned in section 1.4, the concept of thermal equilibrium can be used to categorize different types of plasmas. Because of the presence of different charged and neutral species, plasmas can have different temperatures [42,45]. In "*thermal plasmas*" the translational, rotational, vibrational, and electronic temperatures are the same everywhere inside the plasma, indicating that the plasma is in "*local thermodynamic equilibrium (LTE)*". When plasma has non-equal temperatures, it is in "*non-local thermodynamic equilibrium (non-LTE)*" and is referred to as a "*non-thermal*" plasma [42].

1.5.1 Thermal plasmas

Thermal plasmas are mainly characterized by high temperatures ranging between 4000 and 20,000 K [42,45]. Therefore, thermal plasma can be a very interesting solution for metallurgy and coating applications as it reaches temperatures between 1.7 and 8.7 times higher than the highest achievable temperatures by burning fossil fuels (2300 K) [42]. High temperatures in thermal plasmas accelerate the dissociation of nitrogen and oxygen molecules, followed by the thermal Zeldovich reactions (i.e., production of NO), making these reactions the most dominant mechanisms in the specific case of NF [6]. Thermal plasmas are in local thermodynamic equilibrium, meaning that the concentration of produced NO in thermal plasmas cannot be higher than 5% due to thermodynamic limitations [6,47]. The minimum energy consumption that can possibly be achieved for NF in thermal plasmas is about 0.86 MJ/mol, hence, this process is unable to compete with the HB process with an energy cost of 0.48 MJ/mol [6,48].

Even though thermal plasmas are in LTE conditions, meaning that temperature-related degrees of freedom are (locally) in equilibrium inside the plasma [42], chemical equilibrium is not necessarily reached in such plasmas. Chemical equilibrium refers to a state in a chemical mixture where the concentrations of reactants and products are constant and no change is observed in the system properties [49]. The reason is that, in addition to temperature, other system characteristics, such as reaction rates, the density of species, and energy transfer processes, can also influence the chemical equilibrium. High temperature and species density gradients, and short residence time of the species inside the plasma are some of the reasons that in many cases a chemical equilibrium cannot be achieved in a thermal plasma [50]. However, enhancing the collisions in a system, by operating the process under low pressures and/or high temperatures, can help in achieving chemical equilibrium in thermal plasmas.

1.5.2 Non-thermal plasmas

A potential difference applied between two electrodes leads to the generation of a non-thermal plasma and it was discussed earlier that these plasmas are in non-local thermodynamic equilibrium, hence, different temperatures exist, with the electron temperature being the highest and the gas temperature being the lowest and close to room temperature [42,45]. The most

important reaction mechanisms in non-thermal plasmas are ionization, dissociation, recombination, and excitation reactions, and their repeated occurrence results in the production of new ions, electrons, and neutral species, as well as the emission of light [42].

Because of the high energy demand to break the strong triple bonds in a nitrogen molecule, nitrogen dissociation is the rate-limiting step of the NF process [5–7]. Non-equilibrium effects can result in vibrational excitation of nitrogen molecules in non-thermal plasmas, leading to a lower reaction barrier of nitrogen dissociation [6,51]. Additionally, as the gas temperature in non-thermal plasmas is close to room temperature, integrating a catalyst with a plasma for further enhancing the process efficiency and the selective production of chemicals is of high interest [6,42,52].

1.5.3 Warm plasmas

There is a third type of plasmas, the so called "*warm plasmas*", which operate in the temperature range between 2000 and 4000 K, produce energetic electrons and excited species, and thus combine characteristics of thermal and non-thermal plasmas [17,42]. The high temperature in warm plasmas accelerates the thermal dissociation of nitrogen molecules [6]. Additionally, due to presence of non-equilibrium effects, electron impact and vibrational excitation of nitrogen molecules can help to further increase the NO production through the vibrationally-induced Zeldovich mechanism [17].

1.6 Plasma reactors

Numerous plasma systems, including radio frequency (RF), laser produced, corona, glow, (packed bed) dielectric barrier, (pulsed) (gliding) arc, plasma jets, and microwave (MW) discharges, have been investigated by scientists for NF [17]. In this section we discuss the characteristics of gliding arc (GA) and inductively coupled plasma (ICP) reactors, as they are the reactors used in this thesis.

1.6.1 Gliding arc plasma reactors

In a GA plasma reactor with classical configuration, gas breakdown occurs in between two diverging electrodes, as shown in Figure 1.2. This configuration is also known as a flat or 2D gliding arc [45].

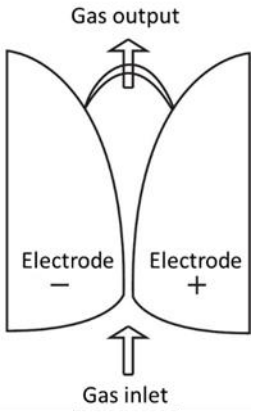

Figure 1.2. Gliding arc reactor in flat configuration, adopted from [45].

Imposing a potential difference between two electrodes results in the formation of an arc discharge (at the spot where the electrodes are at the closest distance from each other), which starts to move in the same direction as the gas flow [45]. As the arc moves, it becomes longer, because the distance between the electrodes increases, and it extinguishes where the distance between the electrodes is so long that plasma sustainment is impossible [45]. Figure 1.3 shows how an arc discharge in four noble gases (i.e., He, Ne, Ar, and Kr) moves in a 2D GA reactor.

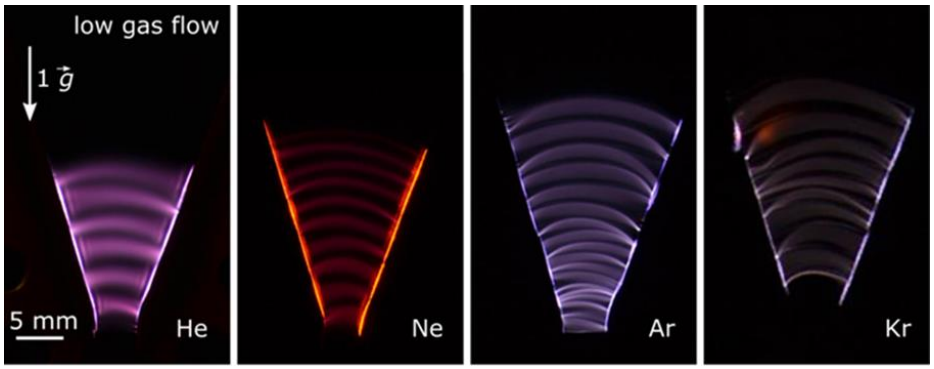

Figure 1.3. Time space evolution of the discharge in a GA plasma reactor operating with four noble gases (He, Ne, Ar, and Kr). Adopted from Potocnakova et al. [53].

Erosion of the electrodes and treatment of only a limited percentage of the gas by the plasma are the main limitations of 2D GA plasma reactors [54]. To solve this issue, recently, 3D GA plasma reactors (Figure 1.4) were introduced in which, due to the presence of a swirling flow, the lifetime of the electrodes is improved, and a higher portion of the gas is treated by plasma [45,54].

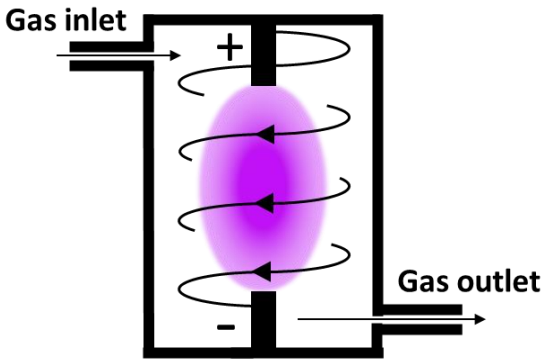

Figure 1.4. Schematic representation of a so-called 3D GA plasma reactor.

1.6.2 Radio frequency (RF) plasmas: inductively coupled plasma (ICP) reactors

In ICP reactors, the application of an electromagnetic field using an inductive coil leads to the generation of a non-equilibrium plasma inside or next to the inductive coil (Figure 1.5 a and b, respectively) [45,55,56]. The generated plasmas are non-thermal plasmas ($T_e \gg T_g$), and therefore, they operate at room temperature [42]. In such a case, aiming to further enhance the process efficiency and the selective production of chemicals, a catalyst can be integrated with the plasma, which makes ICP reactors a suitable option for plasma catalysis [6,17,43]. The catalytic stage can be either a packed bed (i.e., as in the case study of chapter 3) or a fluidized bed inside or downstream of the plasma.

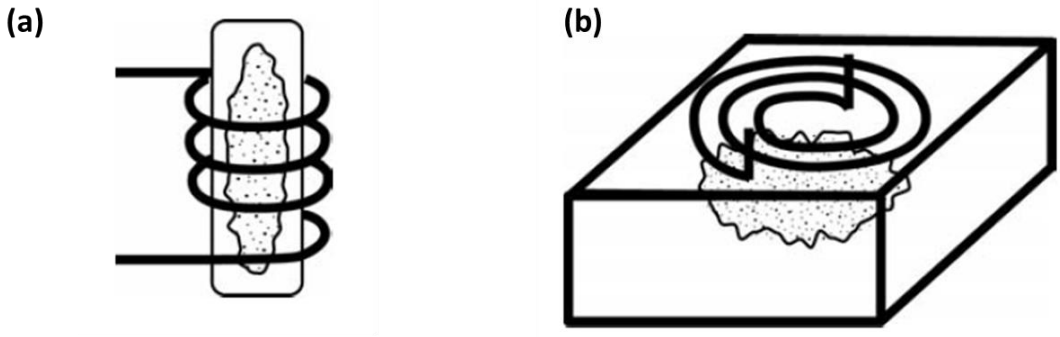

Figure 1.5. Schematics of an ICP discharge where the plasma is located inside the coil (a), and next to the plane coil (b). Adopted from [45].

1.7 Global chemical introduction of NO production from N_2 and O_2

In this thesis, we mainly focus on plasma-based fixation of N_2 by O_2 for the production of NO_x, (i.e. NO + NO_2). In general, we consider the Zeldovich mechanisms to be responsible for the

formation of NO. In the plasma afterglow, however, the plasma-produced NO can be further oxidized into NO_2, which explains why, later in chapter 4 and 5, we also measure traces of NO_2 in our experiments. The standard thermodynamic properties of the Zeldovich mechanism (i.e., standard enthalpy and entropy of the reactions) are summarized in Table 1.1.

Table 1.2. Standard thermodynamic properties of the Zeldovich mechanism.

Number	Reaction	$\Delta H°\ (kJ.mol^{-1})$	$\Delta S°\ (J.mol^{-1}K^{-1})$	reference
R_1	$N_2 + O \rightleftharpoons NO + N$	313.79	11.393	[57]
R_2	$O_2 + N \rightleftharpoons NO + O$	-133.21	13.366	[57]
Sum	$N_2 + O_2 \rightleftharpoons 2NO$	180.58	24.759	[57]

Knowing the thermodynamic properties of the reaction and using the standard Gibbs free energy, $\Delta G°$, the equilibrium constant, K_{eq}, of the reaction can be calculated as [58]:

$$K_{eq} = \frac{k_f}{k_r} = \exp\left(-\frac{\Delta G°}{RT}\right), \qquad \Delta G° = \Delta H° - T\Delta S° \tag{1.1}$$

Figure 1.6 illustrates the equilibrium constant of the overall reaction for the production of NO in a temperature range from 300 to 6000 K.

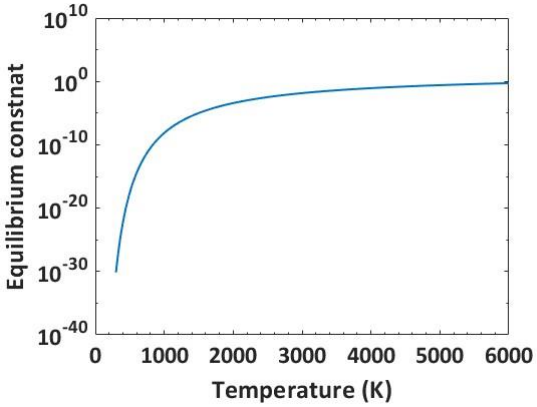

Figure 1.6. Equilibrium constant as a function of temperature for the Zeldovich mechanism.

According to Figure 1.6, the equilibrium constant of the overall reaction is smaller than 1. Given that $K_{eq} = \frac{k_f}{k_r}$, it means that the back-reaction (i.e., recombination of NO back into N_2 and O_2 molecules) is generally thermodynamically more favorable than the forward reaction, and that energy is needed for the net reaction to proceed in the forward direction, which is supplied by the plasma power. Furthermore, Figure 1.6 also demonstrates that the equilibrium constant increases with temperature. Thus, with increasing temperature, the recombination of NO back

into N_2 and O_2 molecules becomes more limited, implying that at high temperatures, thermal NO production is favored. On the other hands, the very low values of the equilibrium constant at low temperatures suggest that non-thermal plasmas, due to operation at low gas temperatures, might not be very efficient for NO production, because a lot of energy is needed for (thermal) dissociation of N_2 molecules [17]. However, non-equilibrium effects, in these plasmas, can enhance the process through vibrational and electronic excitation of N_2 and O_2 molecules. The stored energy in formed excited N_2 and O_2 molecules can be used for surpassing the activation energy of reactions such as N_2 and O_2 dissociation, as well as the Zeldovich reactions (R_1 and R_2) towards the formation of NO, with activation energies of 940 and 494, 319 and 26.19 $\mathrm{kJ.mol^{-1}}$, respectively [7]. Therefore, we can conclude that a synergy between the relatively high gas temperatures, along with some non-equilibrium effects (i.e., vibrational and electronic excitation), as possibly offered by warm plasmas, can form a relatively optimized medium for plasma-based NO production.

1.8 Plasma-based nitrogen fixation toward NO production: Challenges and aim of this thesis

All the information covered in the previous sections conveys one main message: **humanity feels the urge of shifting to a sustainable society more than at any other time in its history**. It is a fact that electrification of the chemical industry plays a key role in this transition [41]. However, there are several challenges and obstacles in the way to electrify the current highly efficient fossil-based chemical processes, which are emitting a huge amount of greenhouse gases in our atmosphere every day and have resulted in disastrous impacts on the climate [34,35,41]. Artificial NF through the HB process is responsible for 1.2% of the annual greenhouse gas emissions to the atmosphere, resulting from human activities [13]. Therefore, it is one of the most important processes for which a sustainable replacement needs to be found.

HNO_3 can be easily formed by dissolving NO and NO_2 (i.e., NO_x) in water via the following reactions:

$$4NO + 3O_2 + 2H_2O \rightarrow 4HNO_3 \quad (1.2)$$

$$3NO_2 + H_2O \rightarrow 2HNO_3 + NO \quad (1.3)$$

Further treatment of the NH_3 (either from losses in livestock manure or produced, e.g., by the HB process), results in the production of NH_4NO_3 [17,59]. Therefore, a less volatile fertilizer with high nitrogen content per mass (35%) can be produced [60].

The possibility of producing fertilizers from air using renewable electricity, and simultaneously, no greenhouse gas emission, resulted in an increasing interest toward plasma technology in the past few years [6]. Additionally, the activation of nitrogen molecules by vibrational and electronic excitation reactions in plasma can lead to an energy-efficient process [6,42,45]. Last but not least,

the modularity (fast on/off characteristic) of plasma technology makes it capable of using intermittent renewable electricity on site for the production of fertilizers using air [6,17,43]. All these advantages offered by plasma technology make it a potential solution for the on-site production of fertilizers in small decentralized plants using air and renewable electricity, which leads to a considerable reduction in fertilizer production and transportation costs [6,17,43]. However, industrialization of plasma-based NF suffers from several challenges, including challenges of plasma catalysis for the selective production of desired species, the high energy cost of plasma-based NF compared to current industrial processes, and the design and development of scaled up and energy-efficient plasma reactors for industrial purposes [6].

The techno-economic study of Rouwenhorst et al. on plasma-based NF for NO_x production compared the energy consumption of this process in various plasma systems (with the best results obtained in warm plasmas, c.f., Figure 1.7) and showed that, if its energy consumption is reduced to 1.1-1.5 MJ/mol, this technology can compete with the current industrial combination of the HB process with the Ostwald process [17].

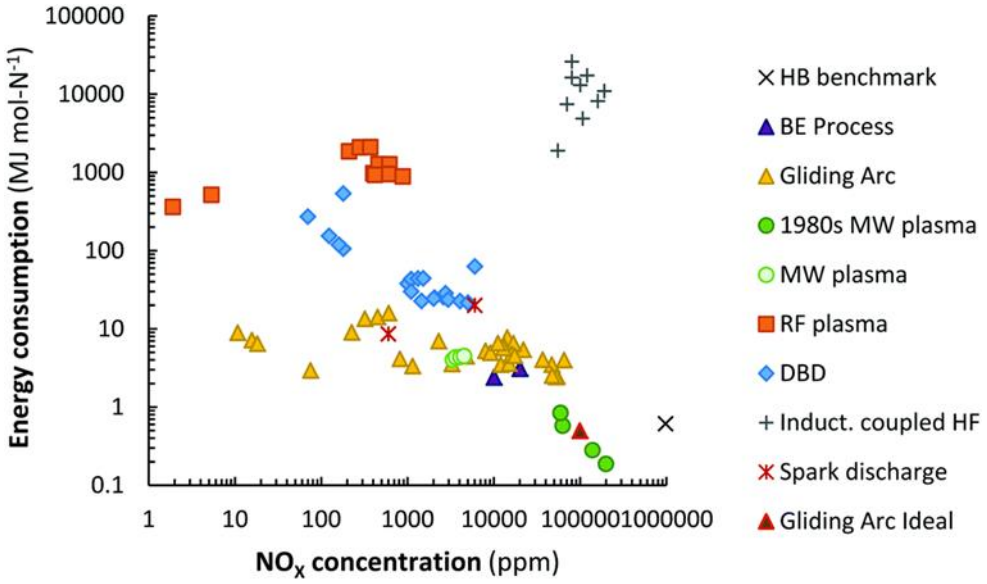

Figure 1.7. Energy cost evaluation for NO_x production in different plasma reactors. Adopted from Rouwenhorst et al. [17]. Note that the data for "Gliding Arc Ideal", as presented in the figure, is the potential lowest value that the energy cost can reach in an optimized GA plasma reactor, as reported by Vervloessem et al. [61]. Furthermore, MW plasmas at reduced pressure in the 1980s showed record values for the production of NO and its energy cost of formation, however these values have never been reproduced since then, and therefore, these results are presented separately [62–65].

Therefore, in the framework of this thesis we have tried to add to the state-of-the-art (SOTA) in plasma-based NO_x production and deal with its limitations using a combination of experimental and modelling work. Specifically, we focused on:

1.8.1 Implementing chemical reaction engineering approaches to investigate plasma-catalyst interactions

In chapter 2 of this thesis, we discuss the mathematical principles of ideal reactors and their Residence Time Distribution (RTD) function. The discussion will then be continued with how a real reactor deviates from an ideal case. Finally, we introduce a non-isothermal heterogeneous catalytic model with axial dispersion for a packed bed reactor. In chapter 3 we apply such a model to the post-plasma catalytic stage of an RF-ICP plasma reactor used for NF, aiming to reveal the underlying mechanisms to improve the process efficiency. Hence, in these chapters, we try to add to the SOTA of plasma catalysis using a computational approach by answering the general research question on **how can we better understand plasma-catalyst interactions, and study the impact of operational parameters on the process efficiency and mechanisms that are responsible for NO production?**

1.8.2 Energy efficiency enhancement of plasma-based NO_x synthesis

In chapter 4 of this thesis, we present an alternative design for a rotating gliding arc (RGA) plasma reactor. In this modification, we integrate the reactor with a specifically designed nozzle, referred to as the "effusion nozzle", and we try to investigate **how improving the reactor design can help enhancing the energy efficiency of plasma-based NO_x production?** To answer this research question, the efficiency of this modified reactor is investigated at different flow rates, input powers, and N_2/O_2 ratios, and we show how a small improvement in the design of a plasma reactor can lead to a clear improvement in the process energy consumption. This novel reactor design has been patented by World Intellectual Property Organization (WIPO) [66]. Hence, in this chapter, we deal with one of the limitations of the SOTA in NO_x synthesis by plasma, namely by improving the process efficiency.

1.8.3 Scaling up of plasma-based NO_x synthesis

In chapter 5 of the thesis, we try to tackle the challenge of developing a low current, high flow rate plasma reactor for NF toward NO_x production, aiming to answer the research question on **how can we design a scaled-up, energy-efficient reactor for plasma-based NF?** To reach this goal, we scan a large range of specific energy input (SEI), to investigate the potential of scaling up the plasma-based NF process. We show that operating at high flow rates allows us to increase the production rate (PR), even at low NO_x concentrations. Finally, we apply a simple approach, based on thermodynamic equilibrium calculations, to estimate the flow rate passing through the plasma region, as well as the gas temperature, in order to better explain our observed experimental results.

2 Heterogeneous catalysis model for fixed-bed reactors

2.1 Introduction

As mentioned in section 1.7, understanding the interactions between plasma and catalyst is one of the challenges to be addressed towards industrialization of plasma-based NF [6]. In this chapter, we introduce a modelling approach for a better understanding of these interactions. We start this chapter by describing ideal reactors and discussing the concept of residence time distribution (RTD) function of these reactors. We continue the chapter by discussing deviations of real reactors from ideal conditions, using the concept of back-mixing. Finally, we develop a 1D heterogeneous catalysis model with axial dispersion (i.e., accounting for the degree of back-mixing in a reactor) for a packed bed reactor and present solutions for evaluation of the parameters used in such models. Later, in chapter 3, we apply such a model for the catalytic stage of an RF-ICP reactor, which is located downstream of the plasma, aiming to better understand the interactions between plasma species and catalyst.

2.2 Ideal chemical reactors

By definition, an enclosed system, which enables the execution of chemical reactions is called a chemical reactor [67–69]. In general, models for chemical reactors can be categorized as ideal and non-ideal [68]. In this section we discuss the characteristics of chemical reactors at ideal conditions and explain how one can derive mathematical correlations to explain the behavior of such systems.

2.2.1 Continuously stirred-tank reactor (CSTR)

A perfectly mixed chemical reactor, operating in steady-state, is called a CSTR [68]. A CSTR is schematically illustrated in Figure 2.1. The assumption of perfect mixing means that the temperature and concentration of different species are equal everywhere (i.e., inside and at the outlet of the reactor) [68,69].

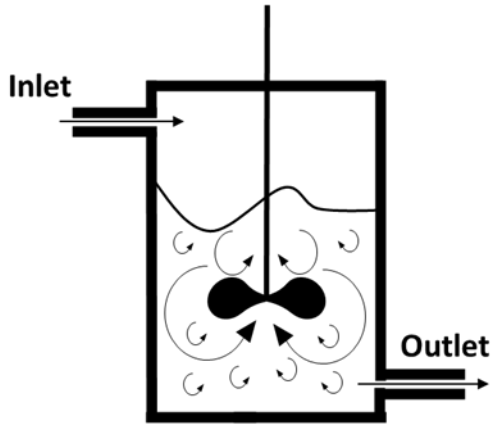

Figure 2.1. Schematic representation of a CSTR.

This implies that no concentration gradient exists in a CSTR, and therefore, the mole balance of species A, participating in the reaction $A + \frac{b}{a}B \rightarrow \frac{c}{a}C + \frac{d}{a}D$, is derived as [68]:

$$V = \frac{F_{A0} - F_A}{-r_A} \tag{2.1}$$

Where F_{A0} and F_A represent the flow rate of species A in and out of the reactor, respectively.

Considering X to be the conversion of reactant A inside the reactor, the outlet flow rate of species A can be calculated as [68,69]:

$$F_A = F_{A0} - F_{A0}X \tag{2.2}$$

By inserting equation (2.2) into equation (2.1), we can express the design equation for a CSTR reactor as follows [68,69]:

$$V = \frac{F_{A0}X}{-r_A} \tag{2.3}$$

2.2.2 Plug flow reactor (PFR)

A PFR is a tubular reactor, in which reactions, and subsequently, the production/destruction of different species, occur when the fluid flows toward the outlet of the reactor, implying the existence of a concentration and reaction rate gradient along the axial axis of the system, while no gradient exists in the radial direction, c.f., Figure 2.2 [68,69].

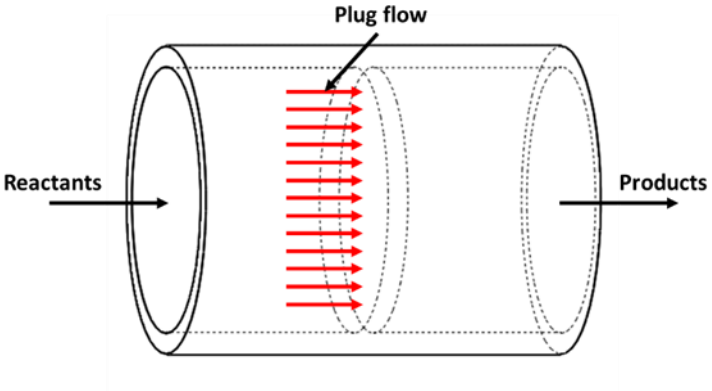

Figure 2.2. Schematic representation of a PFR.

Conducting a mole balance for species A, which participates in the reaction $A + \frac{b}{a}B \rightarrow \frac{c}{a}C + \frac{d}{a}D$ in a PFR, the following mathematical correlation can be derived [68,69]:

$$\frac{-dF_A}{dV} = -r_A \tag{2.4}$$

Writing F_A as a function of F_{A0} and X, as in equation (2.2) and differentiating the resulting correlation we have [68,69]:

$$dF_A = -F_{A0}dX \tag{2.5}$$

Finally, inserting equation (2.5) into equation (2.4), leads to the governing equation of a PFR reactor as follows [68,69]:

$$F_{A0}\frac{dX}{dV} = -r_A \tag{2.6}$$

2.3 Residence time distribution (RTD) function

The residence time in a reactor is defined as the time spent by different species inside a chemical reactor [68]. In contrast to real reactors, all the species spend an equal period of time inside an ideal reactor [69]. The distribution of the residence time in a reactor is expressed by a mathematical function, known as the "*residence time distribution (RTD)*" function [69].

2.3.1 RTD in plug flow reactors

The main assumption, in a PFR, is that the concentration of different species remain constant in the radial direction and the residence time of all species inside the reactor is the same [68,69]. Therefore, mathematically, the RTD function, $E(t)$ (Figure 2.3), of a PFR is expressed by a Dirac delta function, which occurs at a time point equal to the mean residence time of the system, τ (equation (2.7)) [69].

$$E(t) = \delta(t - \tau) \tag{2.7}$$

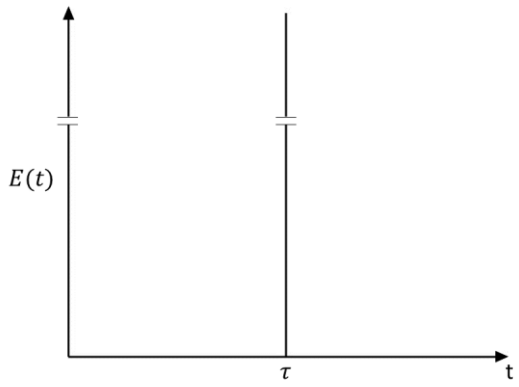

Figure 2.3. Residence time distribution function of a PFR reactor.

2.3.2 RTD in a CSTR

Perfect mixing is the main assumption in an ideal CSTR, implying that the concentration of species is the same everywhere inside and at the outlet of the reactor [68,69]. To derive the RTD of an ideal CSTR, we assume that an inert tracer is injected to the reactor at time zero, and therefore, by conducting a mass balance for this inert tracer, the following correlation can be derived [69]:

$$\begin{aligned} In\ - Out &= accumulation \\ 0\ - vC\ &=\quad V\frac{dC}{dt} \end{aligned} \tag{2.8}$$

where ν, C, and V, are volumetric flow rate of the tracer, concentration, and the reactor volume, respectively.

As the concentration is constant throughout the reactor, integrating equation (2.8) at time zero when $C = C_0$ results in [68,69]:

$$C(t) = C_0 e^{-t/\tau} \tag{2.9}$$

Considering that [69]

$$E(t) = \frac{C(t)}{\int_0^\infty C(t)dt} \tag{2.10}$$

The RTD function of an ideal CSTR can be derived, through insertion of equation (2.9) into equation (2.10) and analytical calculation of the integral in the denominator, leading to [69]:

$$E(t) = \frac{e^{-t/\tau}}{\tau} \tag{2.11}$$

2.4 Back-mixing and deviation of reactors from the ideal conditions

Back-mixing is a negative phenomenon, which affects a reactor conversion, yield, and selectivity, and indicates how much a reacted material likes to blend with unreacted species in a reactor [70]. PFR and CSTR models are derived based on idealized assumptions of no mixing in the axial direction and a perfectly mixed flow, respectively [68]. However, there is always a level of back-mixing in real reactors, as they operate far from the ideal conditions [70,71].

Dividing the convection rate of a physical quantity by its rate of diffusion, results in the derivation of the Peclet dimensionless number, Pe, which basically is the product of the Reynolds, Re, and Schmidt, Sc, dimensionless numbers (equation (2.12)) [72,73].

$$Pe = Re\,Sc = \frac{Lu}{D} \tag{2.13}$$

With L being the system's characteristic length, u the fluid velocity and D the diffusion coefficient.

According to the definition of the Pe, it can be a good measure for quantifying the degree of back-mixing in a reactor. In a perfectly mixed system (i.e., a CSTR) the diffusion coefficient approaches infinity, and thus, Pe in such a system is zero [69]. On the other hand, in a system without mixing (i.e., PFR) the diffusion coefficient (in the axial direction) approaches zero, and therefore, the Pe number of such a system approaches infinity. The degree of back-mixing in all real reactors is in between that of a PFR and CSTR [69].

2.5 1D heterogeneous catalysis model with axial dispersion for a packed bed reactor

In this section we introduce a 1D heterogeneous catalysis model, which accounts for mass transfer in the gas and solid phase, as well as the energy and momentum balances across the catalyst bed.

Due to the presence of diffusion and non-uniform velocities in a real reactor, different species experience a distribution of residence time, meaning that there is always a certain level of back-mixing in such reactors and these types of flows are known as dispersed plug flows, which are naturally statistical and can be described a similar way to molecular diffusion [69]. This implies that, using a similar approach to Fick's second law of mass transfer, the effect of back-mixing can be expressed by a unique axial dispersion coefficient [68,69]. As capturing the influence of the complex transport phenomena, occurring in a real reactor, by a mathematical model is very difficult, we make a few assumptions to simplify the problem.

2.5.1 Model assumptions

To derive the governing mathematical equations of our model, the following assumptions are made:

a) Our mathematical model assumes that the system under study is operating in a dispersed plug flow regime, as discussed above, and temperature and concentration gradients only exist in the axial direction, with the flow moving through the reactor with a velocity identical to the average fluid velocity inside the reactor.
b) Because there are no temperature and concentration gradients in the radial direction, and based on the analogies between dispersed plug flow and diffusion, it is assumed that dispersion occurs only along the axial axis of the reactor, and the effects of diffusion and non-uniform velocities can be integrated into an axial dispersion coefficient [74].
c) Heat transfer through the walls of the reactor, in non-adiabatic processes, result in substantial concentration gradients in the radial direction. Therefore, the process is assumed to be adiabatic in nature.
d) The ideal gas law is applicable.
e) The catalyst particles are small enough (< 0.1 mm) so that no temperature gradient should be considered within the catalyst particles. Additionally, in such a case, intra-porous mass and energy transport limitations can be neglected (i.e., each point on the interior of the catalyst particle surface is accessible for each species to react); therefore, the so-called catalyst effectiveness factor, η_j, is assumed to be unity for all the reactions (see section 2.6 for more information).
f) As the model will be developed for a packed bed reactor, only negligible movements of the catalyst particles (due to fluid flow) occur in the catalyst bed. Therefore, the porosity of the bed is assumed to be constant.

2.5.2 Governing equations

The governing equations can be derived from the mass, energy and momentum balances on a slice of infinitesimal thickness dz (as depicted in Figure 2.4) during an infinitesimal time dt [75,76].

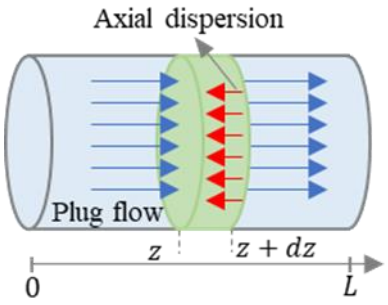

Figure 2.4. Side view of the modeled catalytic reactor.

In the following, we describe the mass and energy balance in the gas and solid phase in the catalytic bed, respectively, as well as the Ergun equation for the pressure drop across the catalyst bed, which accounts for the momentum transfer.

(a) Mass and energy balance in the gas phase (equations (2.14) **and** (2.15)**):**

$$\varepsilon_b \left(\frac{\partial C_i}{\partial t}\right) + u_s \frac{\partial C_i}{\partial z} + k_{g,i} a_v \left(C_i - C_{i,s}\right) = \varepsilon_b D_z \frac{\partial^2 C_i}{\partial z^2} + r_i^{gas} \qquad (2.14)$$

In equation (2.14), the term $\varepsilon_b \frac{\partial C_i}{\partial t}$ represents the transient behavior of the concentration, C_i, of species *i* in the gas phase, where ε_b is the catalyst bed porosity. The term $u_s \frac{\partial C_i}{\partial z}$ accounts for changes in the concentration of gas phase species *i* in the axial direction due to convection, where u_s is the superficial gas velocity. Note that, in general the gas superficial velocity should be inside the derivative. However, as we assume that the gas flows through the reactor with a velocity equal to the average fluid velocity inside the reactor, in our case this parameter can be out of the derivative. Additionally, the interactions of the catalyst bed and the gas flow are not considered in the convective term, as it represents the motion of the gas inside the catalyst bed as a whole, and therefore, the catalyst bed porosity, ε_b, does not appear in this term of the mass balance equation. The term $k_{g,i} a_v \left(C_i - C_{i,s}\right)$ represents the mass transfer of species *i* from the gas phase to the solid phase (catalyst surface), where $k_{g,i}$ is the gas-to-solid mass transfer coefficient of component *i* and a_v is the external surface area per unit volume of the catalyst bed. In general, the mass transfer between the gas and solid phase is associated to both adsorption phenomenon and the mass transfer in the boundary layer between the gas and solid phase. Later in section 2.6.4, we discuss that the effectiveness factor in our system can be assumed to be 1 for all the reactions due to the very small diameter of the catalyst particles. This implies that the mass transfer near the catalyst surface is limited by the surface reactions and the limitations due to mass transfer in the boundary layer are negligible. Additionally, the overall adsorption rate of different gas phase species on the free sites of the catalyst can be calculated using the transition state theory (i.e., the rate by which different species are transferred from the gas phase to the

surface of the catalyst). Therefore, assuming the effectiveness factor to be unity, by substituting the term $k_{g,i}a_v(C_i - C_{i,s})$ with adsorption rates, calculated based on the transition state theory, the mass transfer between the bulk of the gas and the surface of the catalyst can, with a fair accuracy, be estimated. The term $\varepsilon_b D_z \frac{\partial^2 C_i}{\partial z^2}$ stands for the changes in the concentration of species *i* in the gas phase due to axial dispersion, with D_z the axial dispersion coefficient. Finally, the term r_i^{gas} represents the production or destruction of species *i* through the gas phase reactions.

$$\varepsilon_b \rho_g C_{pg} \left(\frac{\partial T_g}{\partial t}\right) + u_s \rho_g C_{pg} \frac{\partial T_g}{\partial z} = h_f a_v (T_s - T_g) + \lambda_z^f \frac{\partial^2 T_g}{\partial z^2} \quad (2.15)$$

In equation (2.15), the term $\varepsilon_b \rho_g C_{pg} \frac{\partial T_g}{\partial t}$ accounts for the changes in the gas phase temperature, T_g, as a function of time, where ρ_g is the gas phase density and C_{pg} is the heat capacity of the gas phase. The term $u_s \rho_g C_{pg} \frac{\partial T_g}{\partial z}$ represents the gas phase temperature changes through convective heat transfer throughout the axial direction, z, due to movement of the gas phase across the catalyst bed, where u_s is the gas superficial velocity. Similar to mass transfer, the convective term, in the energy balance, does not consider the interaction between the gas flow and the catalyst bed, and it represents the heat transfer due to movement of the gas as a bulk, and therefore, the bed porosity, ε_b, does not appear in the convective term of the energy balance in the gas phase. The term $h_f a_v (T_s - T_g)$ stands for the heat transfer between the bulk of the gas and the solid phase, with h_f the heat transfer coefficient, and T_s the temperature at the catalyst surface. The term $\lambda_z^f \frac{\partial^2 T}{\partial z^2}$ denotes changes in the gas temperature through the axial direction of the catalyst bed due to conductive heat transfer, with λ_z^f the effective axial thermal conductivity. In general, wall-to-gas and wall-to-bed heat transfer can also be included in the overall energy balance equations. However, these heat transfer phenomena lead to temperature gradients in the radial direction, which is not consistent with the plug flow assumption in our model. Therefore, we assume that the process is adiabatic, and we neglect wall-to-bed and wall-to-gas heat transfer. Furthermore, in systems where the concentrations of the produced species are significantly lower than the reactants, we can assume that the density and heat capacity stay constant across the system and are almost equal to the values corresponding to the gas flow fed to the reactor. Finally, since in our system transport phenomena, dominantly, occur close to the surface of the catalyst, and knowing that the contribution of gas phase reactions to the overall heat transfer inside the system is typically smaller than surface reactions, we incorporate the effect of all reaction enthalpies in the energy balance of the solid phase to ensure accurate capturing of the heat transfer behavior at the catalyst surface where the majority of the transport phenomena is happening.

(b) Mass and energy balance in the solid phase (equations (2.16) **and** (2.17)**):**

$$\frac{\partial C_{i,s}}{\partial t} - k_{g,i} a_v \left(C_i - C_{i,s}\right) = (1 - \varepsilon_b) r_i^s \tag{2.16}$$

In equation (2.16), the term $\frac{\partial C_{i,s}}{\partial t}$ represents the time-dependent change in concentration of species *i* on the catalyst surface (i.e., in the solid phase), and the term $(1 - \varepsilon_b) r_i^s$ accounts for the production or destruction of species *i* through surface reactions in the solid phase.

$$\rho_{bed} C_{p,bed} \left(\frac{\partial T_s}{\partial t}\right) + h_f a_v \left(T_s - T_g\right) = (1 - \varepsilon_b) \sum -\Delta H_{rxn,j} \eta_j R_j \tag{2.17}$$

Finally, in equation (2.17), $\rho_{bed} C_{p,bed} \frac{\partial T_s}{\partial t}$ accounts for time-dependent temperature changes of the solid phase, with ρ_{bed} and $C_{p,bed}$ the density and heat capacity of the catalyst bed, respectively. The term $h_f a_v \left(T_s - T_g\right)$ represents the heat transfer between the gas and solid phase, and the term $(1 - \varepsilon_b) \sum -\Delta H_{rxn,j} \eta_j R_j$ stands for the amount of heat released from, or added to, the surface due to the occurring reactions, where η_j is the so-called catalyst effectiveness factor for reaction *j* (see section 2.6 for more information). As written in section 2.5.1, we assume η_j is 1 in our model, but we keep this parameter in the above equation, so that this equation is also more generally valid, for other conditions.

In general, the temperature at the catalyst surface can be different from the bulk gas temperature. In systems with a minimal temperature increase at the catalyst surface, the time dependency of the surface temperature ($\frac{\partial T_s}{\partial \tau}$) can be neglected. Therefore, the gas-solid heat transfer rate can analytically be calculated from equation (2.17) as follows:

$$h_f a_v (T_s - T) = (1 - \varepsilon_b) \sum -\Delta H_{rxn,j} \eta_j R_j \tag{2.18}$$

(c) Ergun equation for the pressure drop across the catalyst bed (equation (2.19)**)**

When investigating packed bed reactors, modelling a gas flow through porous media can be substantially simplified, due to the uniform velocity and relatively constant porosity of the system [77]. Therefore, using an analogy with flow in pipes and accounting for the contributions of frictional losses and inertia, the momentum balance of a packed bed reactor can be simplified to the Ergun equation, which correlates the pressure drop across the catalyst bed with the gas velocity inside the reactor as follows [77,78]:

$$f_p = \frac{150}{Gr_p} + 1.75 \tag{2.19}$$

Here f_p and Gr_p are the fixed bed friction factor and modified Reynolds number, respectively, and they are defined as:

$$f_p = \frac{\Delta p}{L}\frac{D_p}{\rho u_s^2}\left(\frac{\varepsilon^3}{1-\varepsilon}\right) \tag{2.20}$$

$$Gr_p = \frac{\rho u_s D_p}{(1-\varepsilon)\mu} \tag{2.21}$$

Where Δp is the pressure drop (Pa) across the catalyst bed, L is the length of the catalyst bed (m), D_p is the equivalent spherical diameter of the packing (m), ρ is the density of the gas mixture $(\mathrm{kg\ m^{-3}})$, μ is the dynamic viscosity of the gas mixture $(\mathrm{kg\ (m\ s)^{-1}})$, u_s is the gas superficial velocity $(\mathrm{m\ s^{-1}})$, and ε is the void fraction (porosity) of the catalyst bed.

Substituting equations (2.22) and (2.23) in equation (2.24), the Ergun equation can be derived as:

$$\frac{\Delta p}{L} = 150\frac{\mu u_s}{{D_p}^3}\frac{(1-\varepsilon)^2}{\varepsilon^3} + 1.75\ \frac{\rho u_s^2}{D_p}\frac{(1-\varepsilon)}{\varepsilon^3} \tag{2.25}$$

The first term in the right hand side of equation (2.26) represents the contribution of viscous effects on the pressure drop, which are more important in laminar flow conditions, and the second term represents the pressure drop contributions due to inertial effects, which are more important in turbulent flow conditions.

Note that in the literature, several correlations for calculation of the pressure drop across a catalyst bed are suggested, with the Ergun equation being the most common one, due to its simplicity and reasonable accuracy in estimating the pressure drop in packed-bed reactors [79]. Therefore, we used this equation for calculation of the pressure drop in our model. However, for systems with very small Reynolds numbers, due to the very small diameter for example, other correlations, such as Carman, Rose and Rizk, Eisfeld and Schnitzlein, and Reichelt, are also suggested in the literature [79–83].

2.6 Model parameters

There are many physical properties used in our model, like mass transfer coefficient, heat transfer coefficient, axial dispersion coefficient, and effective thermal conductivity. Normally their values are unknown or sometimes very difficult to measure experimentally. Therefore, we use empirical correlations to determine these properties. According to literature, those empirical

correlations have already been successful in modelling of packed bed reactors. The mass transfer coefficient is not used in our model, as the term accounting for mass transfer between gas and solid phase can be replaced by the adsorption rates calculated from the surface kinetics model (c.f., explanations for equation (2.14) above). Similarly, the heat transfer coefficient is not used in our model, as it can be determined analytically (c.f., explanation for equations (2.17) and (2.18) above). However, for systems with less information on the kinetics or with no control on the catalyst bed temperature, the calculation of these properties is crucial. Therefore, the conventional correlations that are normally used in modeling of fixed bed catalytic reactors for all the physical properties used in our model are presented in this section.

2.6.1 Gas-to-solid mass and heat transfer coefficient

The gas-to-solid mass transfer coefficient of species i in the gas phase, $k_{g,i}$ $(\mathrm{m}^3(\mathrm{m}^2\ \mathrm{s})^{-1})$, can be calculated using the following correlation [75,84]

$$k_{g,i} = j_{D,i} Re Sc_i^{1/3} \frac{D_i}{d_p} \tag{2.27}$$

$$j_{D,i} = \frac{Sh}{Re Sc_i^{1/3}} \tag{2.28}$$

In equations (2.27) and (2.28), $j_{D,i}$ is the Chilton-Colburn factor for mass transfer, D_i is the effective diffusion coefficient in $\mathrm{m}^2\mathrm{s}^{-1}$, and d_p is the diameter of the catalyst particle in m. Finally, Re, Sc_i, and Sh are the Reynolds, Schmidt, and Sherwood dimensionless numbers, respectively, which are given by [75,85,86]:

$$Sc_i = \frac{\mu_g}{\rho_g D_i}; \text{for } 0.6 < Sc < 7000, \text{and } 0.25 < \varepsilon_b < 0.96 \tag{2.29}$$

$$Sh = 2 + 1.1 Sc^{1/3} Re^{0.6} \tag{2.30}$$

Where μ_g is the gas dynamic viscosity $(\mathrm{kg\ m^{-1}s^{-1}})$, Sc_i is the Schmidt dimensionless number, and ε_b is the catalyst bed porosity.

Similarly, in order to determine the heat transfer coefficient, $h_f(\mathrm{W\ (m^2\ K)^{-1}})$, the following relation can be used [84,87]:

$$h_f = j_H \frac{C_{pg} G_s}{Pr^{2/3}} \tag{2.31}$$

Where G_s is the mass velocity of the gas phase $(\mathrm{kg\ (m^2\ s)^{-1}})$, and j_H is the Chilton-Colburn factor for heat transfer and is given by [84]:

$$j_H = \frac{Nu}{RePr^{1/3}} \tag{2.32}$$

Where Nu is the Nusselt dimensionless number. The following relation is recommended for determining the Nu number in packed beds [85,86]:

$$Nu = 2 + 1.1Pr^{1/3}Re^{0.6} \tag{2.33}$$

2.6.2 Axial dispersion coefficient

In chemical engineering and fluid dynamics, the axial dispersion coefficient, D_z ($\mathrm{m^2 s^{-1}}$), is used to integrate the impact of non-uniform velocities and diffusion (c.f., section 2.5) [68,69], i.e., to account for the degree of back-mixing and deviation from ideal reactor conditions (c.f., section 2.4), in a tubular reactor. For a packed bed reactor, the axial dispersion coefficient can be calculated as follows [88]:

$$D_z = 0.73D_m + \frac{0.5u_s d_p}{1 + 9.49\, D_m/u_s d_p} \tag{2.34}$$

Where D_m is the average molecular diffusivity ($\mathrm{m^2 s^{-1}}$) and u_s is the superficial gas velocity ($\mathrm{m\ s^{-1}}$).

The average molecular diffusivity, D_m, can be calculated as [88]:

$$D_m = \frac{RT}{p}\sum C_i D_i \tag{2.35}$$

Where C_i is the concentration of species i in the gas phase ($\mathrm{mol\ m^{-3}}$), R is the gas universal constant ($\mathrm{J(K\ mol)^{-1}}$), p is the total pressure of the system (Pa), and D_i is the effective diffusion coefficient ($\mathrm{m^2\ s^{-1}}$) of species i in the gas phase and is calculated as follows [89]:

$$D_i = \frac{1}{\left(\tau_{cat}/\varepsilon_b\right)\left(\frac{1}{D_{Amix}} + \frac{1}{D_{Kn,i}}\right)} \tag{2.36}$$

Where ε_b is the catalyst bed porosity, which is defined as [69]:

$$\varepsilon_b = 1 - \frac{V_p}{V_t} \tag{2.37}$$

Where V_p and V_t are the total volume of catalyst particles and of the catalyst bed (m^3), respectively. τ_{cat} is the catalyst tortuosity factor, which indicates how efficient is the diffusion in a catalyst particle [90], and can be calculated as follows [91]:

$$\tau_{cat} = \sqrt{\frac{\varepsilon_b}{(1-(1-\varepsilon_b)^{1/3})}} \tag{2.38}$$

In equation (2.36), D_{Amix} ($\mathrm{m^2\ s^{-1}}$) is the molecular diffusion coefficient of species A in the gas mixture, calculated by Blanc's law [92]:

$$\frac{1}{D_{Amix}} = \sum_i x_a \frac{1}{D_{AB}} \tag{2.39}$$

Where D_{AB} ($\mathrm{m^2\ s^{-1}}$) is the binary molecular diffusion coefficient of species A into each of the other species (B) that are present in the gas phase, and x_a is the mole fraction of species A in the gas phase. D_{AB} is given using the following equation [93]:

$$D_{AB} = \frac{1.00 \times 10^{-3} T^{1.75} (1/M_A + 1/M_B)^{1/2}}{p[(\Sigma_A \upsilon_i)^{1/3} + (\Sigma_B \upsilon_i)^{1/3}]^2} \times 10^{-4} \tag{2.40}$$

Where M_A and M_B are the molecular weights ($\mathrm{g\ mol^{-1}}$) of species A and B, respectively, p is the pressure (here in atm) and T is the temperature in K. $\Sigma_A \upsilon_i$ and $\Sigma_B \upsilon_i$ are the sum of special atomic diffusion volumes of the atoms that are forming species A and B, respectively. The special diffusion volumes for N_2, O_2, N, O, NO are 18.5, 16.3, 4.54, 6.11, and 10.65, respectively [93,94].

Finally, in equation (2.36), $D_{Kn,i}$ is the Knudsen diffusion coefficient ($\mathrm{m^2 s^{-1}}$) of species i in the gas phase, which can be calculated as follows [89]:

$$D_{Kn,i} = \frac{d_{pore}}{3} \sqrt{\frac{8RT}{\pi M_i}} \tag{2.41}$$

Where M_i is the molecular weight of species i ($\mathrm{g\ mol^{-1}}$), and d_{pore} is the diameter of the catalyst pores (m). Fang et al. [95], studied the effect of platinum on the sintering morphology of YSZ ceramics, and the reported value for the pore diameter was 10.4×10^{-9} m. As this was the same catalyst combination used in the post-plasma catalytic reactor for which we apply this model in chapter 3, we assumed this value in our model.

2.6.3 Effective thermal conductivity

The effective thermal conductivity, λ_z^f, is given by the following relation [96]:

$$\frac{\lambda_z^f}{\lambda_g} = \frac{\lambda_z^\circ}{\lambda_g} + 0.75PrRe \tag{2.42}$$

and

$$\frac{\lambda_z^\circ}{\lambda_g} = \varepsilon_b + \frac{1-\varepsilon_b}{0.139\varepsilon_b - 0.0339 + \frac{\left(\frac{2}{3}\right)\lambda_g}{\lambda_s}} \tag{2.43}$$

Where λ_g, λ_z^f, λ_z°, and λ_s are the average gas, effective, axial, and solid thermal conductivities ($\mathrm{W\ (m\ K)^{-1}}$), respectively. Pr and Re are the Prandtl and Reynolds dimensionless numbers, respectively, that are given as:

$$Re = \frac{\rho_g u_s d_p}{\mu_g};\ \ 0.1 < Re < 1500 \tag{2.44}$$

$$Pr = \frac{C_{pg}\mu_g}{\lambda_g} \tag{2.45}$$

Where ρ_g is the density of the gas phase ($\mathrm{kg\ m^{-3}}$), u_s is the gas phase superficial velocity ($\mathrm{m\ s^{-1}}$), d_p is the diameter of the catalyst particles (m), μ_g is the gas dynamic viscosity ($\mathrm{kg\ (m\ s)^{-1}}$), and C_{pg} is the heat capacity of the gas phase ($\mathrm{J\ (kg\ K)^{-1}}$).

2.6.4 Catalyst effectiveness factor

To quantify the extent of reactant diffusion into the catalyst pores, in order to react at the catalyst active sites, we use the definition of the catalyst effectiveness factor, η_j, which is the proportion of the total reaction rate (i.e., both in the gas phase and at the surface of the catalyst) to the reaction rate at the catalyst surface [69]. To calculate the effectiveness factor, in porous media with no mass transfer limitations, the Thiele modulus can be used [97]. The Thiele modulus and the effectiveness factor, for a first order reaction, are correlated as [69,98]:

$$\eta\phi_1^2 = 3(\phi_1 coth\phi_1 - 1), \qquad \phi_1 \propto r_p \tag{2.46}$$

Where ϕ_1 is the Thiele modulus for a first order reaction and r_p is the radius of the catalyst particle. According to equation (2.46), there is a direct correlation between the Thiele modulus

and the particle diameter, implying that upon increasing or decreasing the particle diameter, the Thiele modulus varies in the same manner, and as a result the reaction becomes more and more diffusion and surface limited, respectively (i.e., according to the definition, the effectiveness factor varies in the range between 0.1 and 1, respectively) [68,69]. The same explanation can also be applied to second order reactions, with the only difference being the correlation that describes the relation of the Thiele modulus and the effectiveness factor compared to equation (2.46). The size of the catalysts used in the system for which we, later in chapter 3, apply this model, is in the order of micrometers [99]. Therefore, we assume that the catalyst particles are so small (i.e., smaller than 0.1 mm in diameter) that the reaction is surface limited and the effectiveness factor in our model can be considered to be 1 for all reactions.

3 Post-plasma catalytic model for NO production: Revealing the underlying mechanisms to improve process efficiency[1]

[1] This chapter is published as: **H. Ahmadi Eshtehardi**, K. Van 't Veer, M.-P. Delplancke, F. Reniers, A. Bogaerts, Post-plasma Catalytic Model for NO Production: Revealing the Underlying Mechanisms to Improve the Process Efficiency, ACS Sustain. Chem. Eng. 11 (2023) 1720-1733 https://doi.org/10.1021/acssuschemeng.2c05665.

3.1 Introduction

In chapter 1 we discussed that plasma-based NF is gaining increasing interest for the production of fertilizers, due to its special capabilities that can help in the storage of renewable electricity in chemical compounds, making this technology a key potential for electrification of the chemical industry [41–43]. Additionally, based on a techno-economic analysis of plasma-based NO_x synthesis performed by Rouwenhorst et al., we discussed that the EC of plasma-based NO_x production is potentially a competitor of the combined HB and Ostwald process, if we can further optimize the current plasma reactors and apply efficient plasma-catalyst interactions [17].

Non-thermal plasmas, due their characteristics (i.e., operation at room temperature while electron temperature is in the order of thousands of K), can be a potential energy-efficient process for plasma-based NF, as the electrons can activate the gas molecules, by (vibrational and electronic) excitation, ionization, and dissociation, which can be more cost-efficient than just thermal dissociation. However, due to the high reactivity of non-thermal plasmas, it is difficult to selectively produce the desired product [42,45]. Hence, non-thermal plasma can be combined with catalysts in so-called plasma catalysis to improve the reaction selectivity [100]. However, studies on the interactions of plasma and catalyst are very few, and thus, further research in this field is required.

One of the earliest reports on plasma catalysis is a U.S. patent by Henis for $\mathrm{NO_x}$ removal [101]. On the other hand, Rapakoulias et al. studied the $\mathrm{NO_x}$ synthesis in an inductively coupled high frequency plasma reactor using $\mathrm{MoO_3}$ and $\mathrm{WO_3}$ as catalyst. The $\mathrm{NO_x}$ yield reported was 8% without catalyst, and increased to 19% by using the $\mathrm{WO_3}$ catalyst [102]. $\mathrm{MoO_3}$ was also coated on the reactor wall of a MW plasma by Mutel et al. [62]. An EC of 0.93 MJ/mol-N was reported for NO production, which provided 78% improvement in energy efficiency compared to the plasma process without catalyst. Sun et al. studied the $\mathrm{NO_x}$ formation in a dielectric barrier discharge (DBD) reactor with single stage configuration using $\mathrm{CuZSM-5}$ as catalyst. Temperatures above 350 °C were favorable for $\mathrm{NO_x}$ production [103]. Plasma-catalytic NO production in a glow discharge reactor was investigated by Belova and Eremin, who found the catalyst effectiveness to be in the following order: $\mathrm{Pt > CuO > Cu > Fe > Ag}$ [104,105].

Modelling of plasma-catalytic NO production can be useful to better understand the mechanisms and tune the process. Ideal reactor models, such as CSTR and PFR models (as discussed in chapter 2), are based on idealized assumptions (i.e., perfect mixing and no back-mixing, respectively) [68]. Of course, these simplified assumptions do not reflect reality, as real reactors exhibit some degree of back-mixing. Tanks-in-series models (TISM) and axial dispersion models (ADM), on the other hand, are one-parameter models, that describe reactors that are partially mixed [71]. Ma et al. employed a CSTR model, in combination with experiments, to study plasma-catalytic NO production in an RF-ICP reactor at low pressure using Pt catalyst. They investigated the

synergistic effect of plasma and post-discharge catalyst on the production of NO, and determined the major NO production mechanisms [99].

ADMs, which account for back-mixing and molecular diffusion in the axial direction, are very robust for modeling fixed bed catalytic reactors and have been widely used for investigation of various catalytic processes [75,76,106–112] . In chapter 2, we introduced a 1D heterogenous catalysis model for a packed reactor. In the present chapter, we will apply such a model for post-plasma catalytic production of NO. Compared to CSTR models, as studied by Ma et al. [99], this modelling approach is more complicated. However, it provides more information, as it allows to determine the concentration of all species as a function of both time and position across the catalyst bed (in the axial direction), both in the gas phase and on the catalyst surface. Additionally, it allows to study the reactor and catalyst bed design, as well as the effect of operation conditions, toward process optimization.

The aim of this chapter is to introduce this ADM approach for modelling of a post-plasma-catalytic process, which can provide useful insights in how, when, and where different mechanisms play a role, in favor of, or against the pathways towards the desired product, i.e., NO. In first instance, we apply our model to the experiments of Ma et al. [99]. However, as the exact concentrations of different species (except for NO) in the post-plasma gas that enters the catalyst bed were not available in their study, we first check the NO production sensitivity to these concentrations, to estimate the ranges in which our model can reproduce the experimental results and also to obtain more insight into how the post-plasma gas composition can affect the reaction performance in the catalytic bed. Additionally, we will investigate the effect of the degree of back-mixing on the outlet concentration of NO, in a wide range from close to a PFR to close to a CSTR. Finally, we will study the effect of the catalyst bed characteristic length and porosity on the system performance, and we will discuss the mechanisms behind the observed effects. Our model presented here is applied to post-plasma-catalytic NO production, but the concept is more generally valid for other plasma-catalytic systems as well.

3.2 Model description

In chapter 2 we described a 1D heterogeneous catalysis model with axial dispersion for a packed bed reactor. As mentioned earlier in this chapter we aim to apply such a model for the post-plasma catalytic stage of an RF-ICP reactor. Therefore, we first explain the experimental setup to which we will apply our model.

3.2.1 Experimental setup to be modeled

A schematic overview of the modeled experimental setup [99] is shown in Figure 3.1. Using an inductive coil connected to a matching network of an RF generator, a plasma with a length of about 14 cm is generated. The catalyst used in the experiments is a porous medium of Platinum on a Yttria-Stabilized Zirconia (YSZ) support. To prepare the catalyst, an organometallic Pt paste

was brush-painted on the support and the whole structure was heated under an air flow at a temperature of 900 °C for 2 h, aiming to decompose the organometallic compound and achieve fine Pt crystals, of the order of micron, on the surface of the YSZ support. The YSZ support has a thickness of 2 mm (t_{YSZ} in Figure 3.1), a diameter of 25 mm (d_{bed} in Figure 3.1) and a total length of 245 mm (L_{YSZ} in Figure 3.1), which is located at about 15 cm from the plasma core. A comprehensive explanation on the procedure for preparing the catalyst for the experiments is presented in the study of Ma et al [99]. According to the experimental details presented in the study of Ma et al., a plasma afterglow with an estimated temperature of 6000 K can still reach the catalytic stage. In other words, locating the catalyst at this position guarantees that the plasma does not significantly influence the surface characteristics of the catalyst, and simultaneously, active species produced by the plasma can still exist in the gas stream entering the catalytic stage [99]. The temperature at the catalytic part of the reactor is controlled by a heating mantle, which is kept at 873 K. To perform the experiments, a mixture of N_2/O_2 at 5 mbar is injected to the reactor at a flow rate of 100 sccm. The flowing gas mixture is activated by the RF plasma source with a power of about 80 W. A quadrupole mass spectrometer is used to measure the composition of the outflowing gas mixture from the reactor. A full description of the experiments is given in [99]. As illustrated in Figure 3.1, the reactor consists of 2 different stages, i.e., a plasma stage followed by a catalytic stage. In this study we only focus on modelling the catalytic stage. Finally, the deposited Pt catalyst particles on the YSZ support are assumed as a set of packed particles located in a catalyst bed with diameter identical to the diameter of the YSZ support. Therefore, the system is modelled as a packed bed reactor and radial non-uniformities are neglected.

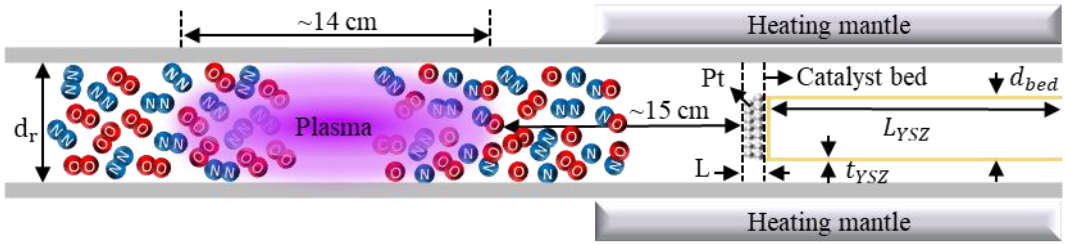

Figure 3.1. Schematic overview of the modelled experimental reactor setup, based on [99].

3.2.2 Governing equations

By considering $\tau = \frac{t}{t_{res}}$ and $\zeta = \frac{z}{L}$, where t_{res} is the residence time and L is the characteristic length of the catalyst bed, and multiplying equations (2.14) to (2.17) (explained in chapter 2) by $\frac{t_{res}L^2}{t_{res}L^2}$, their dimensionless form against time and length can be derived as follows:

Mass and energy balance in the gas phase:

$$\frac{1}{u_s}\frac{\partial C_i}{\partial \tau} + \frac{t_{res}}{L\varepsilon_b}\frac{\partial C_i}{\partial \zeta} + \frac{t_{res}}{u_s\varepsilon_b}k_{g,i}a_v\left(C_i - C_{i,s}\right) = \frac{t_{res}}{Pe\ L}\frac{\partial^2 C_i}{\partial \zeta^2} + \frac{t_{res}}{u_s\varepsilon_b}r_i^{gas} \quad (3.1)$$

Where ε_b is the catalyst bed porosity, u_s is the superficial gas velocity, $k_{g,i}$ is the gas-to-solid mass transfer coefficient of component i, a_v is the external surface area per unit volume of the catalyst bed, $Pe = \frac{u_s L}{D_z}$ is the Peclet dimensionless number, where D_z is the axial dispersion coefficient, and r_i^{gas} is the production or destruction of species i through the gas phase reactions. As mentioned earlier in chapter 2, in dispersed plug flows the presence of diffusion and non-uniform velocities (i.e., back-mixing in a real reactor) can be expressed, in analogy to Fick's second law of mass transfer, using a unique axial dispersion coefficient. In section 2.6, we calculate an overall axial dispersion coefficient for our system, which is a function of both catalytic bed characteristics (such as catalyst particle diameter and gas superficial velocity) and the diffusivities of the different species that exist in the system under study, and therefore, we can use the same value in the mass balance equation of all the species. Furthermore, C_i and $C_{i,s}$ represent the concentration of species i in the gas phase and on the surface of the catalyst, respectively.

$$\frac{1}{u_s}\frac{\partial T_g}{\partial \tau} + \frac{t_{res}}{L}\frac{\partial T_g}{\partial \zeta} = \frac{St\ a_v t_{res}}{\varepsilon_b}\left(T_g - T_s\right) + \frac{\lambda_z^f t_{res}}{u_s L^2 \varepsilon_b \rho_g C_{pg}}\frac{\partial^2 T_g}{\partial \zeta^2} \quad (3.2)$$

Where T_g is the gas temperature, ρ_g is the gas phase density, C_{pg} is the heat capacity of the gas phase, $St = \frac{h_f}{u_s \rho_g C_{pg}}$ is the Stanton dimensionless number, which describes the ratio of the heat dissipated into a fluid to the thermal capacity of the fluid, where h_f is the heat transfer coefficient, T_s is the temperature at the catalyst surface, and λ_z^f is the effective axial thermal conductivity.

Mass and energy balance in the solid phase:

$$\frac{\partial C_{i,s}}{\partial \tau} = (1 - \varepsilon_b)t_{res}r_i^s + k_{g,i}a_v t_{res}\left(C_i - C_{i,s}\right) \quad (3.3)$$

Where r_i^s is the production or destruction of species i through surface reactions in the solid phase.

$$\frac{\partial T_s}{\partial \tau} + \frac{h_f a_v (T_s - T) t_{res}}{\rho_{bed} C_{p,bed}} = \frac{(1 - \varepsilon_b)t_{res}}{\rho_{bed} C_{p,bed}} \sum \Delta H_{rxn,j} \eta_j R_j \quad (3.4)$$

Where ρ_{bed} and $C_{p,bed}$ is the catalyst bed density and heat capacity, respectively, and $\sum \Delta H_{rxn,j}\eta_j R_j$ represents the amount of heat released from, or added to, the surface due to the occurring reactions, where η_j is the effectiveness factor for reactions j (see section 2.6.4 for more information), and $\Delta H_{rxn,j}$ and R_j are the enthalpy and rate of reaction j. As explained in section 2.6.4, we assume η_j is 1 in our model, but we keep this parameter in equation (3.4), so that this equation is also more generally valid, for other conditions.

As also mentioned in section 2.5.2, the term $\frac{t_{res}}{\varepsilon_b} k_{g,i} a_v \left(C_i - C_{i,s}\right)$ in equations (3.1) and (3.3) represents the mass transfer between gas and solid phases, i.e., adsorption of the gas phase species on the catalyst surface. Therefore, it can be replaced by the adsorption rate for each species, that is calculated based on transition state theory in the surface model.

$$k_{g,i} a_v \left(C_i - C_{i,s}\right) = r_{ads} \tag{3.5}$$

More information on this is given in appendix, section 7.1.

Additionally, the term $\frac{h_f a_v t_{res}}{\varepsilon_b \rho_g C_{pg}} (T_s - T)$ in equations (3.2) and (3.4) represents the heat transfer between the bulk of the gas and the catalyst bed. In general, the temperature at the catalyst surface can be different from the bulk gas temperature. In the experiments to which our model is applied, only a small increase in the catalyst bed temperature was experimentally observed, because the catalyst bed was located 15 cm away from the active plasma region and the SEM micrographs taken, by Ma et al., before and after the plasma were very similar [99]. Hence, in our model, the time dependency of the surface temperature ($\frac{\partial T_s}{\partial \tau}$) can be neglected, due to almost constant temperature of the catalytic stage during the process. Therefore, the gas-solid heat transfer rate can analytically be calculated from equation (3.4) as follows:

$$h_f a_v (T_s - T) = (1 - \varepsilon_b) \sum \Delta H_{rxn,j} \eta_j R_j \tag{3.6}$$

As mentioned in section 2.5.2 the momentum balance for such a system is reduced to the well-known Ergun equation accounting for the pressure drop across the catalyst bed (Equations (2.19)-(3.7)). Additionally, it was discussed in chapter 2, section 2.5.2, that the Ergun equation combines the contributions of both viscous and inertial effects, which are more important in laminar and turbulent flow regimes, respectively, on the pressure drop. According to our calculations, the pressure drop in the system under study is mostly dominated by the viscous effects. Furthermore, in section 2.6 we provided solutions for evaluation of the parameters used in our model. An overview of the parameters used in our model and their values are presented in Table 3.1.

Table 3.1. General parameters used in the model, as well as the references where their values are taken from.

Parameter	Name	Value	Unit	Ref.
p	Pressure	0.005	bar	[99]
T_g	Gas temperature	873	K	[99]
S	Number of active sites	2.3×10^{-7}	mol	[99]
N_A	Avogadro's number	6.02×10^{23}	mol^{-1}	
R	Gas universal constant	8.31	$\mathrm{J\ (K\ mol)^{-1}}$	
M_{air}	Molecular weight of air	28.97	$\mathrm{g\ mol^{-1}}$	
Q_{in}	Inlet gas volumetric flow rate	1.67×10^{-6}	$\mathrm{m^3\ s^{-1}}$	[99]
$Q = Q_{in}\frac{T_g}{T^\circ}\frac{P^\circ}{P}$	Actual gas volumetric flow rate	0.001	$\mathrm{m^3\ s^{-1}}$	
V_p	Total volume of catalyst particles	6.9×10^{-9}	$\mathrm{m^3}$	[99]
d_{bed}	Catalyst bed diameter	2.5×10^{-2}	m	[99]
$A_{bed} = \pi\frac{d_{bed}^2}{4}$	Catalyst bed cross section area	4.91×10^{-4}	$\mathrm{m^2}$	
$L = \frac{V_b}{A_{bed}}$	Catalyst bed characteristic length	1.41×10^{-5}	m	
λ_s	Solid thermal conductivity	2.5	$\mathrm{W\ (m\ K)^{-1}}$	[113]
d_r	Reactor diameter	3.4×10^{-2}	m	[99]
$A_r = \pi\frac{d_r^2}{4}$	Reactor cross section area	9.08×10^{-4}	$\mathrm{m^2}$	
$u_s = \frac{Q}{A_r}$	Superficial gas velocity	1.11	$\mathrm{m\ s^{-1}}$	
$V_t = A_r L$	Total volume of catalyst bed	1.28×10^{-8}	$\mathrm{m^3}$	
$t_{res} = \frac{V_t}{Q}$	Residence time	1.27×10^{-5}	s	

ε_b	Catalyst bed porosity	0.46	-	
d_{pore}	Catalyst pores average diameter	10.4×10^{-9}	m	[95]
$\tau_{catalyst}$	Catalyst tortuosity (see section 2.6)	1.57		-
C_T	Number of sites per unit area of the catalyst	1.46×10^{19}	m^{-2}	[99]
$a_v = \frac{1}{C_T V_p}$	External surface area per unit volume of the catalyst	9.87×10^{-12}	$\mathrm{m}^2\mathrm{m}^{-3}$	
C_{pg}	Gas phase heat capacity	1.01×10^3	$\mathrm{J\ (kg\ K)}^{-1}$	

As mentioned before, our modelling approach is developed for modelling of the catalytic bed of a two-stage plasma-catalytic reactor, where a reactive flow, generated from a remote plasma, is exposed to a catalytic bed. However, this approach can also be adapted to a single-stage plasma-catalytic reactor, where the plasma is in direct contact with the catalytic bed. In such a case, a more detailed plasma kinetics model should be considered for the gas phase, in which the presence of several different species, like ions, electrons, electronic and vibrationally excited species, are considered. Of course, such a detailed plasma kinetics model will result in significant expansion of the mass transfer equations governing the plasma-catalytic system. In a single-stage plasma-catalytic system, a higher population of electronic and vibrationally excited species may enhance the dissociative adsorption reaction rates. Additionally, adsorption of other reactive species at the catalytic surface may occur, and therefore, their influence on improving or limiting the process towards the desired product should be carefully investigated. Furthermore, the effect of the presence of numerous species in the gas phase on the axial dispersion coefficient as well as on the physical and thermodynamic properties of the gas phase should also be considered. Moreover, the effect of plasma on the catalysts also needs to be investigated to make sure that the catalyst remains active. Finally, the electrical power, supplied to the gas phase to form a plasma, is an additional source of generation of temperature gradients inside the system, and therefore, its effect should also be considered in the energy balance equations. All these effects are however outside the scope of this chapter and can be considered in follow-up studies.

3.2.3 Initial and boundary conditions

The boundary conditions for this system of equations are as follows:

At the reactor inlet (inlet of the catalyst bed, $\zeta = 0$):

$$C_i = C_i^{after\ plasma}, \qquad \frac{\partial C_{i,s}}{\partial \zeta} = 0, \qquad T = T_g, \qquad T_s = T_{bed}, \qquad p = p_0 \tag{3.8}$$

At the catalyst bed outlet ($\zeta = 1$):

$$\frac{\partial C_i}{\partial \zeta} = \frac{\partial C_{i,s}}{\partial \zeta} = 0, \qquad \frac{\partial T_s}{\partial \zeta} = \frac{\partial T}{\partial \zeta} = 0 \tag{3.9}$$

The initial conditions are defined as:

$$C_{i,0} = C_i^{after\ plasma}, C_{i,s,0} = 0, \qquad T_0 = T_g, \qquad T_{s,0} = T_{bed} \tag{3.10}$$

3.2.4 Reaction kinetics

We only consider the most important reactions for NO production, describing N_2, O_2, N, O, and NO. In order to account for the simultaneous effects of plasma and catalyst on the system behavior, the plasma-catalytic N_2 oxidation kinetics model proposed by Ma et al. is also used in the present study [99]. As the catalytic N_2 oxidation is the reverse of the more widely studied catalytic NO decomposition reaction, a surface kinetics model relevant to NO decomposition on Pt is used to describe the catalytic reactions (Table 3.2).

Table 3.2. Surface reactions included in the model, along with their reaction parameters [114]. Note that $*$ stands for an empty surface site.

Reaction No.	Reaction on Pt (211) surface	ΔH° (eV)	E_a (eV)
R_1	$N_2 + 2^* \rightleftharpoons 2N^*$	1.35	2.55
R_2	$O_2 + 2^* \rightleftharpoons 2O^*$	−2.09	0.17
R_3	$N + * \rightleftharpoons N^*$	−4.26	0.00
R_4	$O + * \rightleftharpoons O^*$	−3.66	0.00
R_5	$N^* + O^* \rightleftharpoons NO^* + *$	−0.61	1.39
R_6	$NO^* \rightleftharpoons NO + *$	1.89	1.89
	ΔH: Reaction enthalpy	E_a: Activation energy	

The activation energy for dissociation of N_2 and O_2 in the gas phase is quite high (i.e., 9.74 and 5.12 eV, respectively), so dissociation in the gas phase is unlikely to occur at the conditions under study. Therefore, the dissociation reactions of N_2 and O_2 were excluded from the reactions describing the gas phase reaction kinetics. Additionally, due to the very low concentration of N

and O radicals in the gas phase and the zero activation energy for their adsorption on the catalyst surface (c.f., Table 3.2), we assume that they will immediately adsorb on the surface upon entrance in the catalyst bed, and thus their recombination back to N_2 and O_2 in the gas phase can be neglected in the catalytic stage of the reactor under study. Therefore, in the gas phase, we only consider the so-called Zeldovich mechanism to occur, which describes the non-catalytic N_2 oxidation (Table 3.3). The question may arise on the reasoning for including the adsorption and desorption mechanisms of N and O radicals and why we should account for these mechanisms. According to the experimental details presented in the study of Ma et al. [99], a plasma afterglow reaches the catalytic stage, indicating that some N and O radicals exist in the gas flow passing through the catalyst. Additionally, N and O radicals can also be produced through dissociative adsorption of N_2 and O_2 molecules that are present in the gas phase. Therefore, the N and O radicals can also interact with the catalyst surface; hence, we also account for the adsorption and desorption mechanisms associated with these species in our surface chemistry. To add the effect of vibrationally excited N_2 and O_2 molecules, formed in the plasma, on the proposed reaction kinetics, the normalized density of each vibrationally excited state is determined considering a Treanor vibrational distribution function [45,115]. We assume that N_2 and O_2 have the same vibrational temperature. Ma et al. estimated vibrational temperatures to be 10000 K in the plasma, based on [116], and they selected $T_v = 6000$ K as a representative vibrational temperature, after the temperature drop expected during the flow of the post-plasma gas to the catalyst bed [99]. Therefore, we also use $T_v = 6000$ K in our model. Furthermore, according to the experiments, the gas temperature in the catalytic stage is controlled using a heating mantle and it is kept at 873 K. Therefore, in our calculations, we use $T_g = 873\ K$ at the inlet of the catalyst bed. Details on the calculation of the plasma-catalytic reaction rate coefficients are presented in appendix (section 7.1) following the methods described by Mehta et al. [117].

Table 3.3. Gas-phase reactions included in the model, along with their reaction parameters [118]. These two reactions form the so-called Zeldovich mechanism of NO formation [119].

Reaction No.	Reaction	A (cm^3s^{-1})	E_a (eV)	ΔH° (eV)	ΔS° (eV K^{-1})
R_7	$N_2 + O \rightleftharpoons NO + N$	3.0×10^{-10}	3.31	3.26	0.123
R_8	$O_2 + N \rightleftharpoons NO + O$	$3.2 \times 10^{-12}\left(\frac{T}{300}\right)$	0.27	−1.38	0.139
	A: Pre-exponential factor		ΔH: Reaction enthalpy		
	E_a: Activation energy		ΔS: Reaction entropy		

Note that NO_2 formation can also be one of the possible pathways in this system. However, in the present work we do not consider (catalytic) NO_2 formation since to our knowledge the kinetic parameters (i.e., reaction barriers and enthalpies on Pt) needed for our model were not available

in literature. Additionally, no experimental measurements of NO_2 were reported by Ma et al. [99], which is used to benchmark our model.

3.2.5 Typical calculation results

The model calculates the concentrations of the various species in the model (both in gas phase and at the catalyst surface) and the reaction rates of all reactions listed in Table 3.2 and Table 3.3, both as a function of time and position across the catalyst bed, for a wide range of conditions. This allows us to determine the most important reactions responsible for production of NO in the chemistry set used in our model. Of special interest is the NO concentration at the reactor outlet, as this is the final product, which we try to optimize.

Finally, based on the total power introduced in the system, and the total NO concentration at the reactor outlet, we can in principle also calculate the EC of NO formation as:

$$EC = \frac{P_{total}}{C_{NO} \times Q} \times 10^{-6} \tag{3.11}$$

Where EC is the energy cost of NO formation ($MJ\ mol^{-1}$), P_{total} is the total power (W), C_{NO} is the NO concentration ($mol\ m^{-3}$) at the reactor outlet, Q is the gas volumetric flow rate ($m^3\ s^{-1}$), and 10^{-6} is the conversion factor from J to MJ.

Note, however, that we cannot calculate the absolute value of the EC, as we do not know the exact power going into the system. Indeed, it consists of the power of the power supply, heating mantle of the catalyst bed and vacuum pump, and the values of the latter two were not reported in the study of Ma. Et al. [99]. Therefore, we will plot the EC in arbitrary numbers, so that we can study the relative trends of the energy efficiency of the system for various conditions, and because the total power going into the system will be (more or less) constant for all conditions, keeping in mind that the power of the power supply is constant, as well as the temperature of the catalyst bed and the pressure (i.e., flow rate of the vacuum pump).

3.3 Results and discussion

3.3.1 Effect of post-plasma species fluxes entering the catalyst bed

To evaluate the NO production sensitivity to the post-plasma fluxes of species entering the catalytic stage, we solved our model for a wide range of post-plasma concentrations of the species involved in the NO production process. It allows us to estimate for which conditions our model can reproduce the experimental NO concentrations, reported by Ma et al. [99]. In addition, this parameter study gives us insights in how the reaction performance in the catalyst bed is affected by the post-plasma composition.

We used the partial differential equation (PDE) solvers in MATLAB & Simulink 2022 for solving equations (3.1)-(3.4). In our model, linear and non-linear PDEs, algebraic equations, as well as initial and boundary conditions are involved. We first checked the sensitivity of the model for discretization, ranging from 10 to 1000 intervals, and the model results were found independent of discretization for discretization intervals above 100. Hence, the catalyst bed of the experimental reactor was axially discretized by 100 uniform space intervals. Since we use the dimensionless form of the governing equations in our calculation and considering that $\zeta = \frac{z}{L}$, 100 uniform space intervals result in a $d\zeta$ = 0.01. Multiplying this value by the system's characteristic length (i.e., $\mathrm{L} = 1.41 \times 10^{-5}\ \mathrm{m}$) leads to $\mathrm{dz} = 1.41 \times 10^{-7}\mathrm{m}$. Given that the axial dispersion coefficient at the conditions under study is in the order of 10^{-5} ($\mathrm{m^2 s^{-1}}$), the Pe number in each calculation cell, $\mathrm{Pe_{cell}} = \frac{\mathrm{u_s dz}}{\mathrm{D_z}}$, gives a value in the order of 10^{-2}. Such a low value for the cell Pe number indicates that the back-mixing plays an important role in each calculation cell. Finally, the output results are reported after 1260 s (or 21 min), when steady state was definitely reached. For time discretization, a time step of around 10^{-7} s was considered from time zero to $\mathrm{t} = 0.01$ s, and after that a time step of 0.01 s was used in our calculations.

According to literature, at similar plasma conditions to the reactor under study, when $log_{10} x_{O_2}$ varies from -4 to -1 (i.e., the $\mathrm{O_2}$ fraction in the feed gas varies from 10^{-4} to 10^{-1}), the $log_{10} \frac{P_N}{2P_{N_2}}$ (i.e., the logarithm of the $\mathrm{N_2}$ dissociation fraction) can vary non-monotonically or decrease monotonically, in a range from -4 to -2.5 [99,120–122]. We solved our model for a wide range of $\mathrm{N_2}$ dissociation fractions between 10^{-5} and 10^{-1}, to completely cover the reported range in the literature at different $\mathrm{O_2}$ fractions in the feed gas, corresponding to the experiments of Ma et al., [99]. Knowing the post-plasma concentration of NO as a function of $\mathrm{O_2}$ fraction in the feed gas, as reported by Ma et al., [99], and assuming that the $\mathrm{O_2}$ dissociation fraction in the plasma is normally one order of magnitude greater than for $\mathrm{N_2}$ [116,123–126], the post-plasma concentration of each species can be calculated as a function of $\mathrm{N_2}$ dissociation fraction, at different $\mathrm{O_2}$ fractions in the feed gas, as described in appendix, section 7.2. Note that the results presented below are strongly influenced by the assumption of a constant ratio between $\mathrm{O_2}$ and $\mathrm{N_2}$ dissociation fraction. Of course, this factor 10 is just an approximation, based on literature, and we do not know the exact value. Therefore, we keep this parameter constant in our calculations.

Figure 3.2 a illustrates the experimental and calculated NO concentration at the reactor outlet, as a function of $\mathrm{O_2}$ fraction in the feed gas. According to the experiments reported by Ma et al. [99], for an $\mathrm{O_2}$ fraction below 0.001, increasing the $\mathrm{O_2}$ fraction in the feed gas results in a slight increase in the NO concentration until it reaches a maximum at an $\mathrm{O_2}$ fraction around 0.001 (see Figure 3.2 a). By further increasing the $\mathrm{O_2}$ fraction in the range from 0.001 to 0.01, the NO concentration starts to drop until it reaches a minimum at an $\mathrm{O_2}$ fraction of about 0.01. Finally, when the $\mathrm{O_2}$ fraction rises to 0.2, the NO concentration also rises drastically. Capturing these trends by our model requires a precise measurement of all different species concentrations in the

post-plasma gas flow that enters the catalyst bed, as these values are used as the initial conditions of our model. However, these data were not available for our case study. Hence, for a certain O_2 fraction in the feed gas (which automatically determines the N_2 fraction), we had to assume a certain N_2 dissociation fraction (which determines the O_2 dissociation fraction, as explained above). Together, they determine the N_2, O_2, N and O concentrations (or fluxes) in the post-plasma mixture (c.f., appendix, section 7.2). When assuming an N_2 dissociation fraction profile as a function of O_2 fraction in the feed gas as illustrated in Figure 3.2 b, which qualitatively captures the behavior described in literature (see above), our model can reproduce with reasonable accuracy the observed experimental trend for the measured NO concentrations at the reactor outlet as a function of O_2 fraction (see Figure 3.2 a).

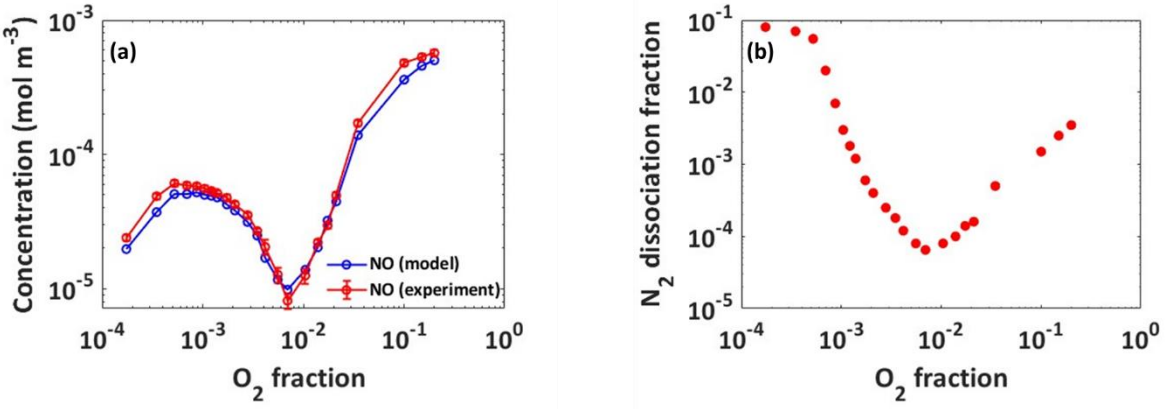

Figure 3.2. (a) Comparison of experimental and calculated NO concentration at the reactor outlet, as a function of O_2 fraction in the feed gas. In (b) the assumed N_2 dissociation fraction is plotted as a function of O_2 fraction in the feed gas, for which our model can reproduce the experimental trends of NO concentration as illustrated in (a). Such a non-monotonic variation in N_2 dissociation fraction as a function of O_2 fraction is indeed also described in literature (see text), indicating that our model can reproduce the experimental NO concentration within a realistic input parameter space.

To further investigate how the post-plasma gas composition affects the reaction performance in the catalyst bed, we plot in Figure 3.3 the NO concentration (a) and its corresponding EC of formation (b) calculated by our model at different N_2 dissociation fractions, as a function of O_2 fraction in the feed gas. Note that the EC is plotted in arbitrary numbers, as explained above, so we can also compare the relative trends for various conditions.

As observed in Figure 3.3 a, the NO production is not really sensitive to the N_2 dissociation fraction at low O_2 fractions in the feed gas (i.e., $x_{O_2} < 1\%$). The reason is that the number of O radicals in the gas flow entering the catalyst bed, and subsequently their concentration at the catalyst surface, is so low that not much NO can be produced through the catalytic process. However, at higher O_2 fractions in the feed gas (i.e., $x_{O_2} > 1\%$), high N_2 dissociation fractions yield a high NO concentration at the reactor outlet, as observed in Figure 3.3 a. On the other hand, the NO concentration is still low at low N_2 dissociation fraction. Indeed, at these higher O_2

fractions, the concentration of O_2 and O radicals in the post-plasma gas flow is higher, and therefore more O radicals can be adsorbed on the catalyst surface, which can then react with the surface-adsorbed N radicals to form NO through the associative recombination reaction (R_5). However, even when enough surface-adsorbed O radicals exist at the catalyst surface, only a low amount of NO can be produced at low N_2 dissociation fractions, due to the low concentration of N radicals in the gas phase and subsequently, at the catalyst surface. This explains why the NO production at the catalytic stage is very sensitive to the N_2 dissociation fraction. As a result, the EC of NO production is higher at lower N_2 dissociation fractions; Figure 3.3 b), while upon increasing the N_2 dissociation fraction, the EC of NO production decreases for N_2 dissociation fractions close to 0.1, at an O_2 fraction of 20% in the feed gas (Figure 3.3 b).

In summary, a high N_2 dissociation fraction (and thus also a high O_2 dissociation fraction, as they are connected: the latter is typically one order of magnitude higher), in combination with a relative high O_2 fraction (~ 20%) in the feed gas, yield a high NO concentration at the reactor outlet and a lower EC of formation (while the opposite conditions give rise to a low NO concentration and high EC). This is logical, because these conditions produce more O and N radicals, which are the main drivers of NO production at the catalyst surface. Indeed, we performed a detailed reaction analysis to determine the dominant mechanisms toward NO production, and the results are presented in the appendix (sections 7.3 to 7.7).

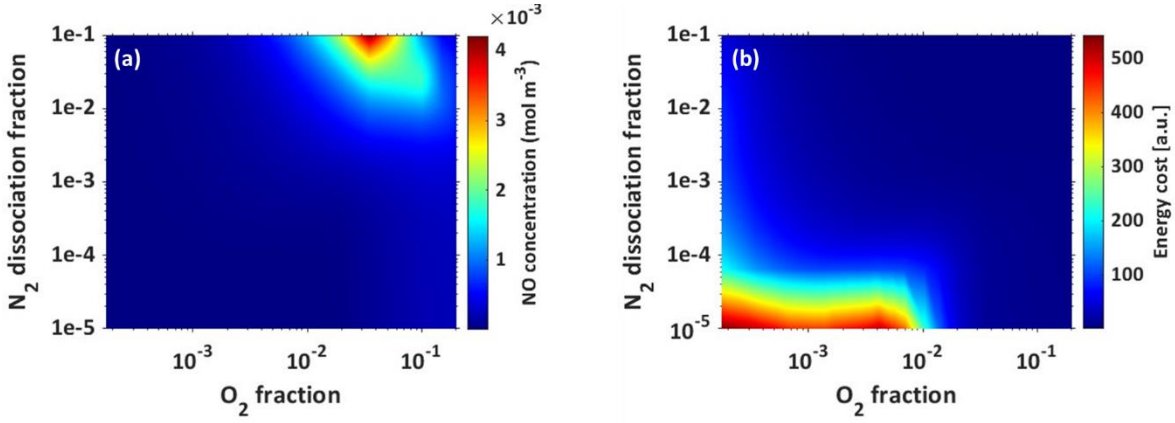

Figure 3.3. Effect of N_2 dissociation fraction and O_2 fraction in the feed gas, on the NO concentration (a), and its corresponding EC of formation (b) calculated by the model.

We also varied the post-plasma concentration of NO in a range from 0 to 6.8×10^{-4} mol m^{-3} (i.e., 10000 ppm) to investigate the effect of NO concentration entering the catalyst bed on the NO concentration at the reactor outlet (Figure 3.4). This study was performed for an N_2:O_2 mixture of 80:20 at an N_2 dissociation fraction of 3.5×10^{-3}, for which our model can reproduce the experimental NO concentration at the reactor outlet. An O_2 fraction of 20% was chosen, as the catalytic effect is still pronounced enough at this condition (comparing 2.2×10^{-4} mol m^{-3} (3200 ppm) and 5.7×10^{-4} mol m^{-3} (8250 ppm) for plasma only and plasma-catalytic processes

in the experiments of Ma et al. [99], respectively). Additionally, this feed gas mixture mimics dry air composition, and is therefore of special interest for industrial purposes. As illustrated in Figure 3.4, even without NO present in the post-plasma gas, about 3×10^{-4} $mol\,m^{-3}$ of NO is produced at the catalyst bed, due to reactions of N, O, N_2 and O_2 at the catalyst surface. Furthermore, a linear dependence is observed for the NO concentration at the reactor outlet as a function of post-plasma concentration of NO. Hence, the total NO concentration at the reactor outlet is the sum of the NO formed in the plasma and a constant amount of 3×10^{-4} $mol\,m^{-3}$ formed at the catalyst bed.

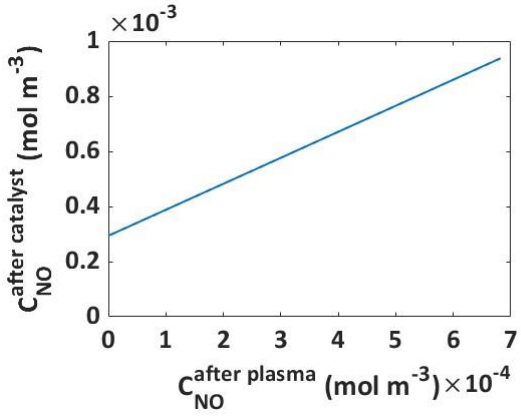

Figure 3.4. Effect of NO concentration entering the catalyst bed on the NO concentration at the reactor outlet ($T_g = 873$ K, $x_{O_2} = 20\%$, $P_{plasma} = 80$ W, $T_v = 6000$ K, $P = 5$ mbar, N_2 dissociation fraction $= 3.5 \times 10^{-3}$).

3.3.2 Effect of back-mixing degree

Increasing the desired product yield (NO in our case) is always the main purpose in design and optimization of any reactor. Figure 3.5 shows how the NO concentration at the reactor outlet and its EC of formation vary with the degree of back-mixing inside the reactor. To this end we solved the model for different Pe numbers (i.e., different axial dispersion coefficients) ranging from 10^{-3} (corresponding to $D_z = 1.6 \times 10^{-2}\ m^2 s^{-1}$, close to CSTR) to 550 (corresponding to $D_z = 2.8 \times 10^{-8}\ m^2 s^{-1}$, close to PFR). Note that for other calculations, the value of the Pe number is calculated based on the operating conditions of the experiment, and was found to be equal to 502, indicating that our system can be described as a PFR, with negligible back-mixing. That also explains why in Figure 3.4, the plasma-produced NO is additive to the NO produced in the catalytic bed, and no NO from the plasma phase is lost by reactions in the catalytic bed. Additionally, approaching CSTR and PFR regimes is also possible at low and high characteristic length and gas superficial velocities, respectively. However, in this study we were mostly interested to investigate the effect of back-mixing on the system performance, and therefore, we varied the Pe number only by varying the axial dispersion coefficient.

As illustrated in Figure 3.5, less back-mixing (i.e., high Pe, close to PFR) yields a rise in the NO production (Figure 3.5 a) and a drop in its EC of formation (Figure 3.5 b). We observe an S shape pattern with increasing Pe number from CSTR to PFR conditions (Figure 3.5 a). The reason is that at lower back-mixing degrees the catalytically produced NO has less tendency to intermix with unreacted species, and therefore, its loss due to axial dispersion decreases. This clearly confirms the adverse effect of back-mixing on the NO concentration at the reactor outlet. Hence, to reduce this adverse effect, the reactor and the catalyst bed size and configuration should be optimized to minimize the degree of back-mixing (i.e., flow pattern as close as possible to a PFR).

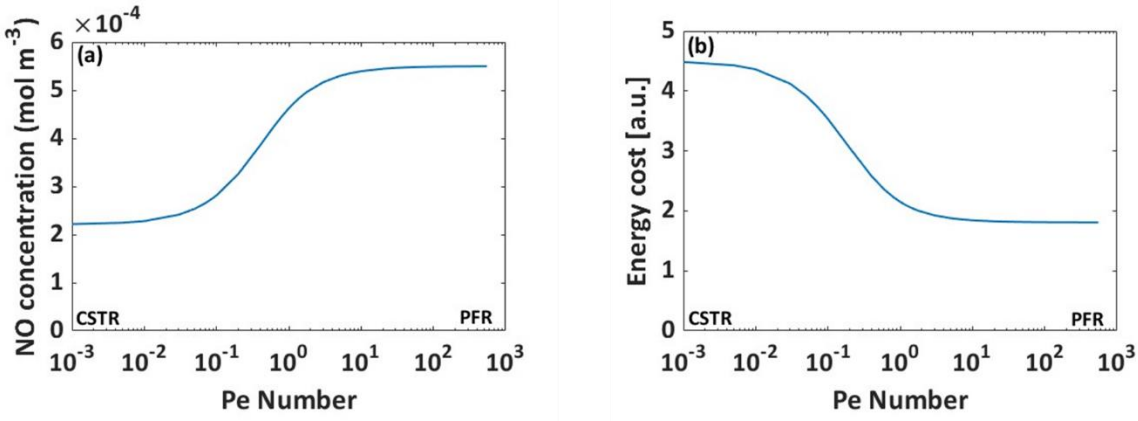

Figure 3.5. Effect of Pe number on the outlet concentration of NO (a), and its EC of formation (b). ($T_g = 873$ K, $x_{O_2} = 20\%, T_v = 6000$ K, $P = 5$ mbar, N_2 dissociation fraction $= 3.5 \times 10^{-3}$).

3.3.3 Effect of the catalyst bed characteristic length

We varied the total volume of catalyst particles from 6.9×10^{-9} m^3 (i.e., total volume of catalyst in the experimental setup) to 10^{-3} m^3. As the diameter of the catalyst bed is considered to be constant, this results in an increase in the characteristic length of the catalyst bed from 14 μm to 2 m. It should be noted that a characteristic length of 2 m is not realistic in practice, but we performed the simulations in this wide range to show trends. The contact time of the gas with the catalyst (see appendix, section 7.8: Figure 7.7 a) rises from 10^{-5} s (for the smallest catalyst volume of 6.9×10^{-9} m^3, corresponding to the experiments, i.e., characteristic length of 14 μm) to 1.8 s (for the largest catalyst volume investigated of 10^{-3} m^3, corresponding to a characteristic length of 2 m). Normally, increasing the contact time of the gas with the catalyst should result in a higher NO concentration. However, as illustrated in Figure 3.6 a, increasing the characteristic length (i.e., a longer contact time of the gas with the catalyst) results in a lower NO concentration till a minimum is reached at around 1 mm. This is because the increase in characteristic length of the catalyst bed promotes the adsorption of NO and its subsequent dissociation into N and O radicals on the surface (i.e., the net rates of associative recombination (R_5) and NO desorption (R_6) on and from the surface, respectively, dramatically drop, Figure 7.7b). Therefore, in this range when the characteristic length increases from 14 μm to around 1 mm, the NO production rate at the reactor outlet (expressed in $mol\ m^{-3}\ s^{-1}$) sharply decreases from values around 17 to 0.02

$\mathrm{mol\ m^{-3}\ s^{-1}}$ (Figure 3.6 b). As a result, a longer contact time (Figure 7.7 a) is not enough to compensate for the effect of the sharp drop in NO production rate, and to help the process toward more production of NO. Therefore, less NO is produced and its concentration, at the outlet of the reactor, is lower at longer characteristic lengths (Figure 3.6 a). By further increasing the characteristic length of the catalyst bed to values above 1 mm, the NO production rate continues to drop, but this drop is significantly less steep than for shorter characteristic lengths. Simultaneously, the contact time continues to rise with increasing characteristic length (Figure 7.7 a). At these long characteristic lengths (longer than 1 mm), the improvements in contact time of the gas with the catalyst are significant enough to promote the process toward more NO production. In other words, although the NO is produced at lower rates, for longer characteristic lengths the contact time of the gas with the catalyst is long enough to enhance the NO concentration at the reactor outlet (Figure 3.6a).

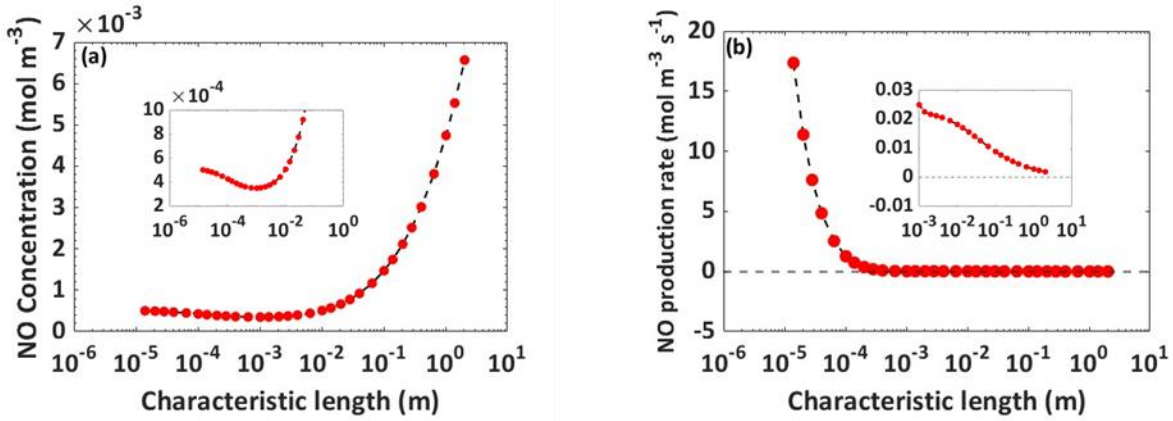

Figure 3.6. Effect of the catalyst bed characteristic length on the NO concentration (a), and the net NO reaction rate (b), at $\mathrm{T_g = 873\ K,\ x_{O_2} = 20\%, T_v = 6000\ K, P = 5\ mbar, N_2 dissociation\ fraction = 3.5 \times 10^{-3}}$.

The effect of the catalyst bed characteristic length on the EC of NO formation and on the NO production rate (in $\mathrm{mol\ s^{-1}}$) is illustrated in Figure 3.7 a and b, respectively. Increasing the catalyst bed characteristic length has no effect on the gas volumetric flow rate. Therefore, the NO concentration is the only variable that determines the NO production rate (the product of NO concentration and the gas volumetric flow rate, i.e., denominator of equation (3.11), thus it follows exactly the same trend as the NO concentration (Figure 3.7 b). Similar to the NO concentration, the NO production rate decreases with increasing characteristic length until it reaches a minimum at around 1 mm (Figure 3.7 b). As a result, the EC of NO formation increases upon increasing characteristic length of the catalyst bed from 14 μm (corresponding to the experimental conditions) to 1 mm (Figure 3.7 a). After this minimum in production rate (or maximum in EC), further increasing the characteristic length results in a higher NO concentration, hence, the NO production rate also increases. As a result, the EC of NO formation decreases towards a characteristic length of 2 m (i.e., around 92% improvement).

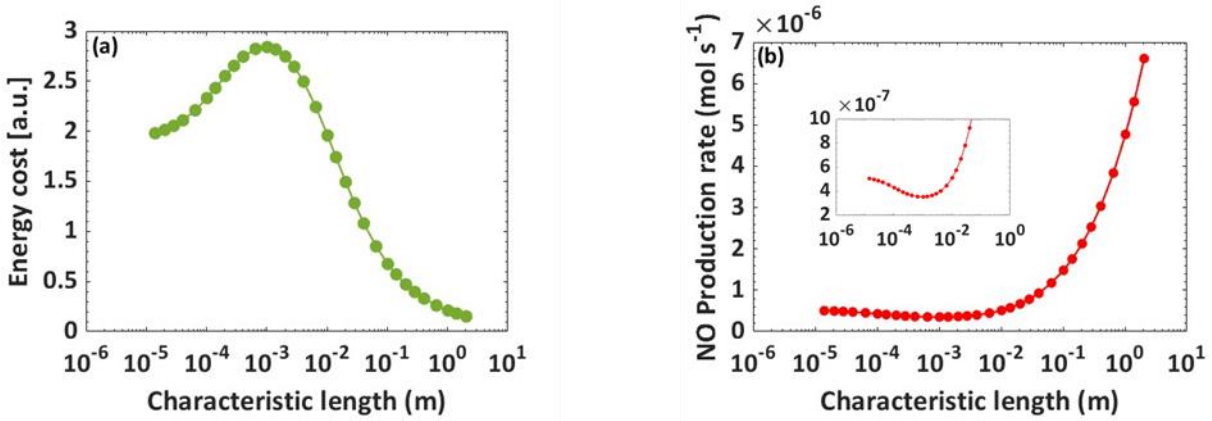

Figure 3.7. Effect of the catalyst bed characteristic length on the EC of NO formation (a), and the NO production rate (b), at $T_g = 873$ K, $x_{O_2} = 20\%$, $T_v = 6000$ K, $P = 5$ mbar, N_2 dissociation fraction $= 3.5 \times 10^{-3}$.

Such an improvement in EC of NO formation might lead to the conclusion that longer catalyst beds significantly improve the process performance. However, such long characteristic lengths (2 m, using 10^{-3} m^3 of the porous Pt catalyst) are not feasible due to the limitations in configuration of the reactor under study and laboratory conditions. This can explain the reasoning behind selection of 14 μm as the characteristic length of the catalyst bed in the experiments, in addition to the fact that it also requires only a limited amount of catalyst. Nevertheless, these results illustrate that our 1D heterogeneous catalysis model allows to investigate the optimum length of the catalyst bed, which is not possible by a CSTR model.

It should be mentioned that the Y-axis in both Figure 3.6 b and Figure 3.7 b is labeled as NO production rate, but the values presented in these figures are different in both unit and actual values. The values in Figure 3.6 b are calculated based on the sum of the reaction rates involving NO, and since overall in these reactions NO is produced, we label the sum as the NO production rate expressed in $mol\ m^{-3}\ s^{-1}$. On the other hand, the values in Figure 3.7 b are calculated as the product of NO and the total volumetric flow rate, which yields the total molar flow rate of NO produced in the system and we label it as NO production rate expressed in $mol\ s^{-1}$.

3.3.4 Effect of catalyst bed porosity

In the reactor configuration under study, the catalyst bed porosity can easily be adjusted by varying the diameter of the catalyst bed (i.e., the diameter of the YSZ support), which can affect the performance. In our model, we varied the catalyst bed porosity from 0.06 (corresponding to a catalyst bed diameter of 33 mm) to 0.99 (corresponding to a catalyst bed diameter of 3 mm). The experiments were performed with a porosity of 0.46, c.f. Table 3.1. Note that by increasing the catalyst bed diameter from 3 to 33 mm, the characteristic length of the catalyst bed decreases

from 1 mm to 8.1 μm. The effect of catalyst bed diameter on the characteristic length and on the porosity of the catalyst bed is explained in appendix, section 7.9.

Figure 3.8 a shows the effect of the bed porosity on the NO concentration at the outlet of the catalyst bed at steady state. A higher bed porosity means that there is more free volume in the catalyst bed for the gas to pass through. Also, the higher the porosity, the longer the characteristic length of the catalyst bed. Therefore, more volume of the gas passes through a longer catalyst bed, which significantly improves the contact time of the gas with the catalyst particles inside the bed (Figure 3.8 b). On the other hand, as the porosity increases (i.e., at longer catalyst bed characteristic lengths), the NO production rate decreases (Figure 3.8 c) due to more NO adsorption and subsequent dissociation on the catalyst surface (c.f., the results presented for the effect of catalyst bed characteristic length). It is clear from Figure 3.8 a that a higher bed porosity results in a higher NO concentration at the outlet of the catalyst bed, until it reaches its maximum at porosity values around 0.9. The reason is that, although at higher porosity values the NO reaction rate decreases a lot (Figure 3.8 c), the higher contact time between gas and catalyst compensates for this drop in NO production rate. Therefore, the overall produced NO at steady state increases with increasing catalyst bed porosity. However, further increasing the bed porosity to values close to 1 means there is almost no catalyst inside the bed anymore (i.e., the effect of surface reactions become negligible), and as a result, the NO concentration at the outlet significantly drops.

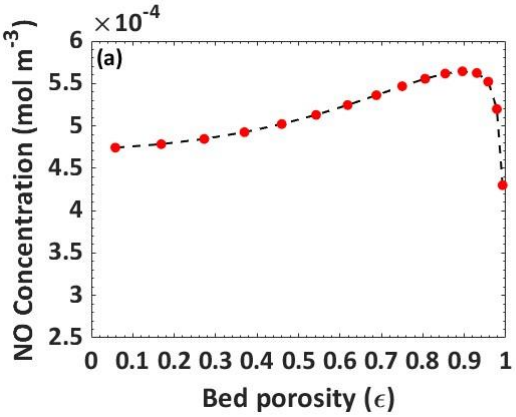

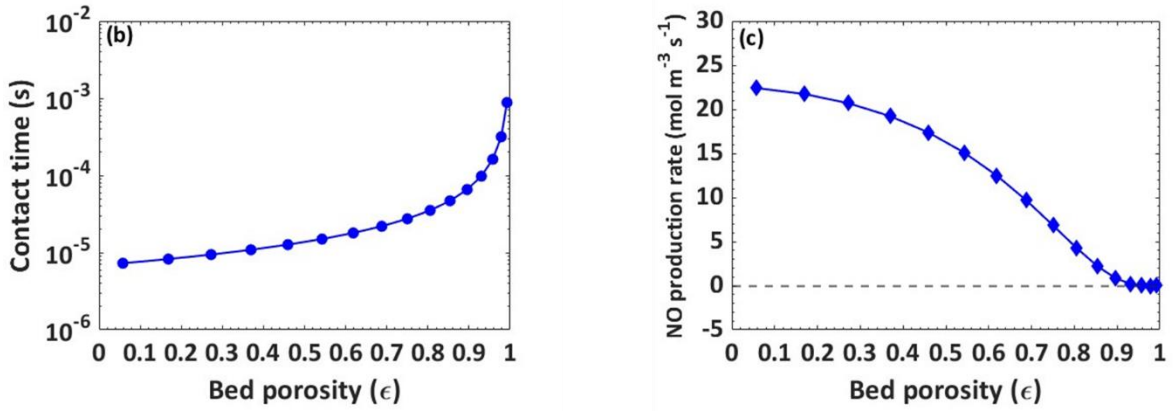

Figure 3.8. Effect of the catalyst bed porosity on the NO concentration (a), the contact time between gas and catalyst (b), and net NO production rate (c), at $T_g = 873\ K,\ x_{O_2} = 20\%,\ T_v = 6000\ K, P = 5\ mbar$, N_2 dissociation fraction $= 3.5 \times 10^{-3}$.

To further investigate the effect of the catalyst bed porosity on the performance of the system, we plot in Figure 3.9 a the EC of NO formation as a function of bed porosity. Increasing the catalyst bed porosity has no effect on the gas volumetric flow rate. Therefore, similar to the case of varying the catalyst bed characteristic length, the steady state NO concentration at the reactor outlet is the only parameter that controls the NO production rate in $\mathrm{mol\,s^{-1}}$ (i.e., product of the NO concentration and the gas volumetric flow rate), and subsequently, the EC of NO formation. As the porosity of the bed increases, the steady state NO concentration at the reactor outlet increases until it reaches its maximum at porosity values around 0.9 (Figure 3.8 a). As a result, the EC (Figure 3.9 a) drops from $\varepsilon = 0.06$ (corresponding to $\mathrm{d_{bed}} = 33$ mm) to $\varepsilon = 0.9$ (corresponding to $\mathrm{d_{bed}} = 11$ mm). After this optimum porosity of 0.9, further increasing the catalyst bed porosity to values close to 1 lead to a significant drop in the NO concentration at the reactor outlet, and subsequently the NO production rate sharply drops (Figure 3.9 b). Therefore, the EC of NO formation increases from $\varepsilon = 0.9$ to $\varepsilon = 0.99$.

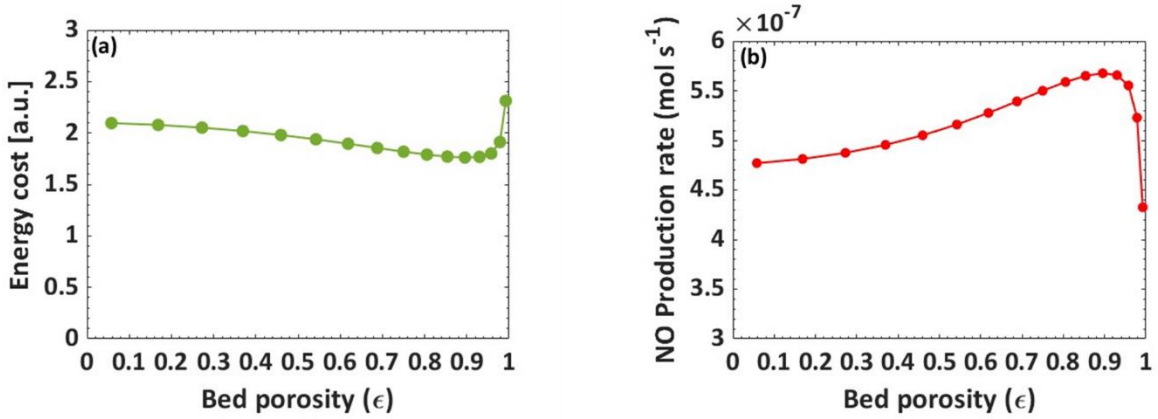

Figure 3.9. Effect of catalyst bed porosity on the EC of NO formation (a), and the NO production rate (b), at $T_g = 873$ K, $x_{O_2} = 20\%$, $T_v = 6000$ K, $P = 5$ mbar, N_2 dissociation fraction $= 3.5 \times 10^{-3}$.

According to our model predictions for the effect of catalyst bed porosity on the NO concentration and its EC of formation, further improvement in the performance may be possible by increasing the porosity of the catalyst bed from 0.46 (corresponding to the experiments) to 0.9. However, achieving such a high catalyst bed porosity might be difficult in practice. Noted that increasing the porosity to these high values in our model was only possible because of the specific configuration of the catalyst bed in the reactor under study. In conventional (commercial) fixed bed reactors, where the catalyst bed is made of roughly uniform catalyst beads, the porosity range is typically quite narrow ($0.35 < \varepsilon < 0.55$) [77]. Therefore, from practical perspective, the selected porosity value in the experiments seemed to be among the best values possible in practice. Although very high or very low porosity values studied in this section are generally not physically possible in real world systems, the porosity values can mathematically vary in a range from zero to one, and these calculations are performed only with the aim of providing insight in how the catalyst bed porosity can affect the system's performance. Additionally, the term catalyst beads, as used here, is a general term which refers to a support on which the catalyst material is immobilized. These beads are not necessarily spherical, and depending on the manufacturing process and the specific requirements of the catalytic application, they can come in various shapes, such as pellets, irregular particles, bi-trilobes, etc. Nevertheless, our calculations provide useful insights in the effect of this parameter, in so far that it can be tuned, and maybe our work can inspire experimental groups to design a catalytic bed with higher porosity.

3.4 Conclusions

Plasma-based NO production has recently gained increased interest as a potential sustainable alternative N_2 fixation process. Plasma catalysis can potentially enhance the performance by coupling a plasma with a (post-plasma) catalytic surface. Mathematical modeling can play a key role in the optimization of the process, but modeling of plasma-catalytic N_2 fixation into NO is poorly studied.

In this chapter, we applied a 1D heterogeneous catalysis model with axial dispersion (i.e., so-called axial dispersion model; ADM, as explained in details in chapter 2, section 2.5) for plasma-catalytic NO production in an RF-ICP reactor. By considering the major transport phenomena in the catalytic bed (i.e., mass, energy, and momentum transfer), the model allows to gain valuable insight in the underlying mechanisms due to coupling of plasma and catalyst, and how to improve the performance. We studied the chemical reactions leading to the production of NO, and the resulting NO concentrations, both at the catalyst surface and in the gas phase, as a function of time and axial position in the reactor.

We investigated the effect of the post-plasma composition (i.e., species concentrations/fluxes) on the NO concentration at the reactor outlet and its EC of formation. For this purpose, we varied (i) the N_2dissociation fraction (which also determines the O_2dissociation fraction, as the latter is typically an order of magnitude higher) and (ii) the O_2 fraction in the feed gas. Together, they determine the post-plasma concentrations (or fluxes) of N, O, N_2 and O_2. In addition, we also studied the effect of varying the NO post-plasma concentration on the NO concentration at the reactor outlet. In general, our model predicts that a higher N_2 dissociation fraction in the post-plasma gas flow leads to a higher NO concentration at the reactor outlet. However, the NO production is not very sensitive to the N_2 dissociation fraction at O_2 fractions less than 1% in the feed gas. A higher O_2 fraction in the feed gas and N_2 dissociation fraction in the post-plasma gas flow result not only in a higher NO concentration, but also in a significant improvement in EC calculated by our model. Finally, a linear increase in the outlet concentration of NO was observed with a rise in the post-plasma concentration of NO for a constant O_2 fraction in the feed gas, but also without NO in the post-plasma mixture, a considerable amount of NO is formed at the catalyst bed, as the N and O radicals are the main drivers of catalytic NO production.

We also studied the effect of back-mixing on the NO production. Our model predicts that higher Pe numbers (i.e., flow patterns close to a PFR and therefore, lower back-mixing) lead to a higher concentration of NO at the reactor outlet and a drop in the process EC. Hence, for process improvement, it will be important to design a catalytic bed reactor resembling as much as possible a PFR.

Increasing the catalyst bed characteristic length in general leads to a high NO concentration and low EC, at least for very long characteristic lengths (around 2 m). Although such value might be unrealistic and would require much more catalyst than the characteristic length used in the experiments, our simulations can provide information on the effect of this parameter on the system performance. Finally, increasing the catalyst bed porosity also results in a higher NO concentration and lower EC, until reaching a maximum at porosity values around 0.9. At still higher catalyst porosity, there would be almost no catalyst inside the bed and therefore the effect of surface reactions would become negligible.

This kind of model has been used before in the field of thermal catalysis, and its robustness in simulation and optimization of various catalytic processes was already demonstrated [75,76,127–

129]. However, in this chapter, we applied such a model for the simulation of a plasma-catalytic process for NO production. Our modeling approach can provide useful insights in the underlying mechanisms responsible for NO production, as a function of time and at different positions across the catalyst bed. Additionally, it can predict the effect of different operating parameters on the NO concentration at the reactor outlet and its EC of formation. Although these model predictions will need to be verified experimentally, and we don't claim the model predictions are quantitatively accurate, at least the results give insights in qualitative trends, when varying certain parameters.

Finally, this type of model is not only useful for explanation and improvement of the system under study, but also can be used for other plasma types coupled with a catalyst. Therefore, this modeling approach can open new windows of opportunity for the simulation, improvement and optimization of plasma-catalytic processes operating in fixed bed reactors, not limited to N_2 fixation, but for various plasma-catalytic gas conversion processes.

4 Effusion nozzle for energy-efficient NO_x production in a rotating gliding arc plasma reactor[1]

[1] This chapter is published as: **H. Ahmadi Eshtehardi***, S. Van Alphen*, C. O'Modhrain, J. Bogaerts, H. Van Poyer, J. Creel, M.-P. Delplancke, R. Snyders, A. Bogaerts, Effusion nozzle for energy-efficient NO_x production in a rotating gliding arc plasma reactor, Chem. Eng. J. 443 (2022) 136529. https://doi.org/10.1016/j.cej.2022.136529. (* shared first authors)

4.1 Introduction

In chapter 1, section 1.7, the high energy consumption of plasma-based NO_x synthesis was mentioned as one of the biggest obstacles of industrialization of this process [6]. Based on a techno-economic analysis performed by Rouwenhorst et al. [17], it was shown that the energy consumption of plasma-based NO_x synthesis can potentially compete with the current industrial processes, such as HB process combined with the Ostwald process, through further plasma reactor optimizations.

Krop and Pollo reported an NO production of 4.7% at an EC of 3.5 MJ/mol, in an electric arc plasma reactor with water injection [130]. Bian et al. studied NO_x production from air in a water jet discharge and reported a NO_x concentration of 1% with an EC of 47 MJ/mol [131]. For RF plasmas, NO_x concentrations around 2-900 ppm (hence, below 0.01%), with EC ranging from 363 to 2133 MJ/mol, were reported [132,133]. Likewise, NO_x concentrations between 0.01 and 0.6% have been reported in dielectric barrier discharge (DBD) plasmas, with EC between 21-540 MJ/mol [103,134–136]. ICPs have been reported to produce NO_x concentrations between 5.5 and 19%, but with EC ranging from 1921 to 26451 MJ/mol [137]. MW plasmas at reduced pressure (50 torr) showed NO productions between 6 and 20% with an EC of 0.2-0.9 MJ/mol; however, these record values were not reproduced since then [62–65]. Direct current (DC) spark discharges yielded NO_x concentrations ranging from 7 to 6000 ppm (i.e., up to 0.6%) with EC between 0.4 and 20 MJ/mol [138–140]. Vervloessem et al. showed that in a pulsed spark discharge, the EC of NO_x production from air can drop to a mere 0.4 MJ/mol, close to the theoretical minimum, but indeed, at the expense of a very low NO_x concentration (300 ppm) [138]. In recent years, there are various papers in literature on GA plasmas, producing NO_x concentrations in the range of 0.001 to 6.5%, with EC between 1.8 and 15 MJ/mol [54,59,61,134,141–146]. For instance, Jardali et. al. performed studies with a rotating gliding arc (RGA) plasma, achieving an EC of 2.5 MJ/mol with an appreciable NO_x concentration of 5.2% in oxygen-enriched air [59]. Very recently, Tsonev et al. showed that increasing the pressure leads to a further improvement of the performance in an RGA reactor, with EC as low as 1.8 MJ/mol, NO_x concentration of 4.8%, and PR of 69 g/h, in oxygen-enriched air, at a pressure of 3 barg [143]. MW plasmas at atmospheric pressure also produce NO_x concentrations in the range of 0.32 to 3.81% with EC between 2 to 4.5 MJ/mol [63,147]. For example, impressive results were achieved by Kelly and Bogaerts, where a MW plasma at atmospheric pressure with oxygen-enriched air gave an EC of 2.0 MJ/mol with NO_x concentration of 3.8% and high production rate (PR) of ca. 86 g/h [147]. Notably, the performance was better at higher power and flow rate, showing the promise for upscaling. Pei et al. performed studies on NF with a DC glow discharge plasma in air and reported a NO_x concentration of 0.7% with an EC of 2.8 MJ/mol [148]. It is clear from above that thermal reactions which dominate in (near-)thermodynamic equilibrium plasmas, give rise to efficient dissociation of N_2 and O_2 molecules. On the other hand, electron impact reactions are important in non-equilibrium plasmas. Direct electron impact dissociation (which often proceeds through electronic excitation) and ionization typically require more energy than strictly needed for bond breaking, and this

explains why non-equilibrium plasmas, such as DBD, exhibit a high energy cost. However, at lower electron energy, electron impact reactions lead to vibrational excitation of N_2 and O_2 molecules, and the stored energy in the vibrationally excited levels can be used to overcome the energy barrier of dissociation and of NO formation. In warm plasmas, both vibrational-induced dissociation and thermal reactions can occur simultaneously, depending on the conditions [6].

Taken together, this literature overview shows that within different plasma systems, warm plasmas, such as GA, MW and DC glow discharge plasmas, have the best performances for plasma-based NO_x production at atmospheric pressure. This is indeed attributed to highly efficient thermal reactions occurring due to high temperatures (> 3000 K) achieved in these plasmas [17,42]. A summary of NO_x concentration and EC for different plasma types as a function SEI is presented in chapter 5, section 5.1.

While the above results look promising, an important limitation is that part of the produced NO_x in the plasma is destroyed after leaving the plasma reactor. Indeed, the temperature in the above plasma reactors (GA or MW) reach a typical value of 3000 K or even higher [59,61], but the gas cools down slowly after leaving the reactor. As a result, the produced NO will react with N or O atoms, back into N_2 and O_2 molecules, which reduces the overall NO_x production, as revealed by modeling [21].

Therefore, in this chapter, we present a design modification to the above-mentioned RGA plasma reactor [59], by coupling it with a specific nozzle, which we call “effusion nozzle”. This causes a fast drop in the gas temperature when the gas leaves the reactor, thereby quenching the unwanted recombination reactions, and thus improving the overall reactor performance. We investigate the performance of this novel plasma reactor/nozzle design in a wide range of operating conditions, i.e., flow rate, input power and N_2 fraction in the feed gas. Although the achieved results are still far from the requirements for industrialization of plasma-based NO_x synthesis, they clearly show that improving the energy efficiency of plasma reactors is feasible through optimization of the reactor designs.

4.2 Reactor setup and effusion nozzle

Figure 4.1 schematically illustrates the RGA plasma reactor, with details of the internal configuration, also showing the rotational gas flow behavior (black arrow line) and the arc plasma (purple) in the center (artist view), in case of steady arc mode (see section 4.3.1). The plasma reactor consists of a nickel cathode, supplied with high voltage, and a grounded stainless-steel anode, coupled to the newly designed effusion nozzle (see below), which acts as the reactor body. A spark plug (NGK BP6ES) without its ground pin is used as the powered electrode (the ground pin is replaced by the stainless-steel body of the reactor). The ceramic piece in the center of the reactor (100 mm in length, 6 mm in diameter) encloses the cathode pin so that only a cylindrical knob (1.4 mm in length, 2.5 mm in diameter) is exposed (red part in Figure 4.1). The reactor body comprises of a cylinder with diameter of 13 mm and length of 11.2 mm, which is followed by a

cone-shape section with diameter decreasing from 13 to 4 mm. The cone-shape section extends to the outlet of the reactor, which is a cylinder of 4 mm diameter and length of 20 mm.

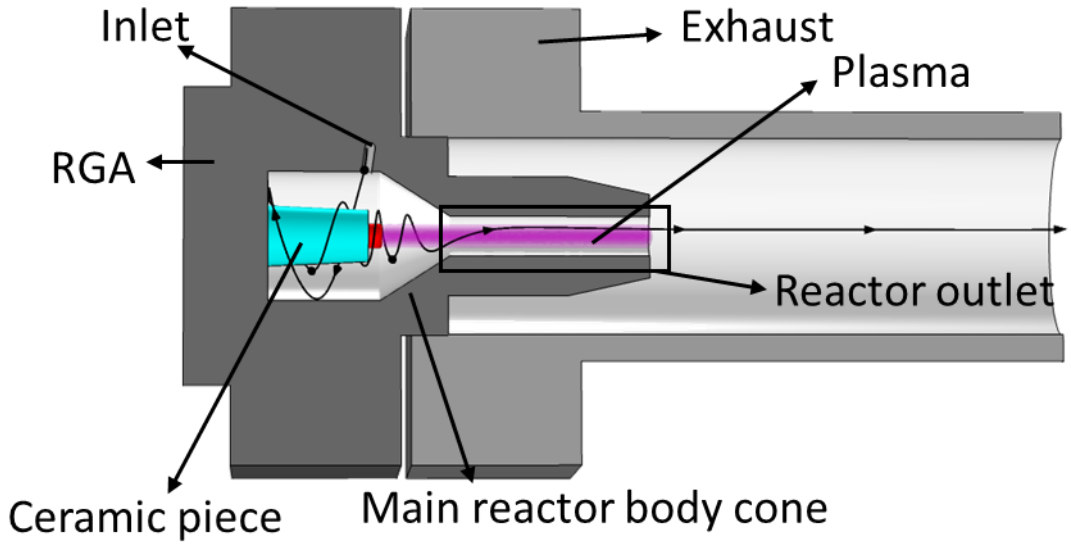

Figure 4.1. Schematic picture of the RGA plasma reactor, illustrating the gas flow behavior (black line) and the plasma in steady arc mode (purple zone). The cathode knob is indicated in red at the left, while the entire reactor body is at anode potential.

The (stainless-steel) effusion nozzle is coupled to the reactor outlet to enhance the reactor performance by cooling the gas temperature and quenching unwanted recombination reactions. The effusion nozzle consists of a gas-receiving cavity with inner diameter of 15 mm and length of 29.5 mm. At the end, it contains six radially distributed tiny “effusion holes” of 0.8 mm diameter, and a cuboid protruding element, called “gas divider”, with 1 mm thickness, perpendicular to the axis of the gas receiving cavity; see Figure 4.2. The effusion nozzle screws over the plasma reactor outlet, abruptly stopping and dividing the air flow, first by the cuboid and then further by these six small radial holes. The gas divider, indicated in red color in Figure 4.2, serves as anchor for the arc. A stainless-steel cylinder with diameter and length of 25 mm and 295 mm, respectively, is coupled to the whole system to collect the exhaust gas stream and to provide connection to the gas diagnostic device.

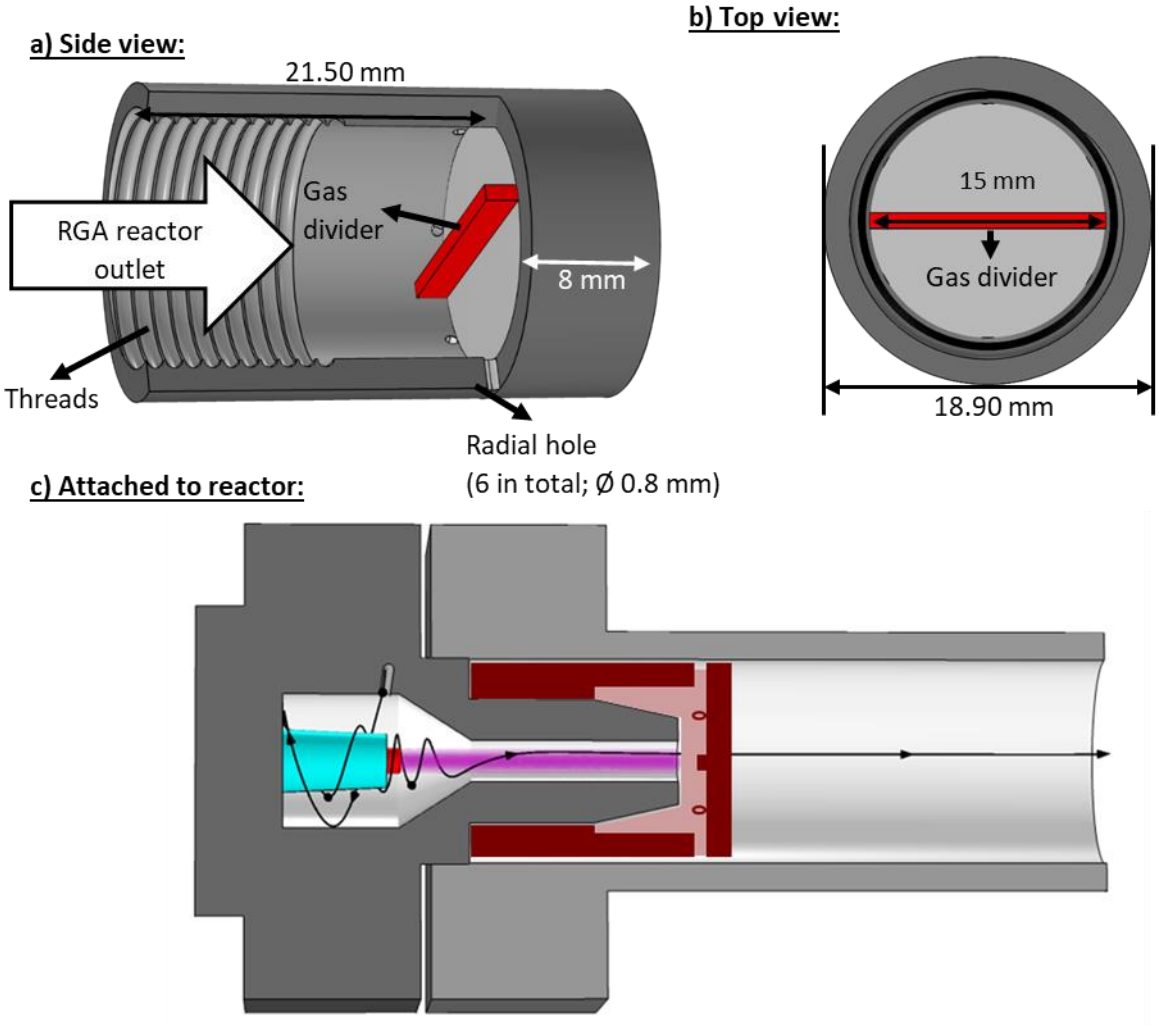

Figure 4.2. Schematic picture of the effusion nozzle with dimensions, in side-view (a), top view (b) and attached to the reactor (c). In the latter case, the nozzle is colored in red. The gas divider (red bar in (a) and (b)) serves as anchor when the effusion nozzle is mounted on the RGA, and it has a width of 1 mm, height of 2 mm, and length of 15 mm. It sits on top of the 8 mm steel back wall, across the whole nozzle.

The arc plasma is ignited using a 10 kV DC power supply (Topower TN-XXZ02). A ballast resistor with a resistance of 25 kΩ was integrated into the circuit. This relatively high resistance counteracts the current variation and inhibits extensive heating of the power supply. Additionally, by integrating this resistance into the circuit, the highest supplied current is 280 mA. A high voltage probe (TESTEC 1000:1) measures the discharge voltage, while the current is measured from the voltage drop across a 25 Ω resistor. An oscilloscope (Keysight DSOX1102A, 70 MHz bandwidth, 2 GSa s-1 sample rate) is utilized to record the time evolution waveform of the discharge voltage and current.

Feed gas (i.e., a mixture of N_2 and O_2 with a purity of 99.999%) was introduced into the reactor via a tangential inlet of 1 mm in diameter (see Figure 4.1). The gas volumetric flow rates are adjusted using mass flow controllers (Bronkhorst F-201CV). In the main RGA reactor body, a reverse vortex flow is created due to the tangential gas inlet and the shape of the reactor. As illustrated by the black line in Figure 4.1, the gas first swirls upwards along the reactor wall, before collapsing into a smaller inner vortex that flows around the ceramic piece and towards the reactor outlet.

We measured the total produced NO_x as the sum of the NO and NO_2 concentrations (%) in the exhaust stream, by a non-dispersive infrared sensor along with an ultraviolet sensor, for quantitative analysis of the species concentrations (EMERSON-Rosemount X-STREAM enhanced XEGP continuous Gas analyzer). N_2O and N_2O_5 are only formed in the ppm range, and therefore do not contribute to the NO_x concentration in a significant way. This is in agreement with our previous studies [59].

The average plasma power (P) is calculated by:

$$P[W] = \sum_{j=1}^{N} \frac{V_j I_j}{N} \tag{4.1}$$

Where I_j and V_j are the recorded discharge current and voltage, respectively, and N is the number of records.

Knowing the plasma power and the total measured NO_x concentration, we define the EC of the process as:

$$EC\ [MJ/mol] = \frac{P[J/s] \times 24[L/mol] \times 60[s/min] \times 100[\%]}{C_{NO_x}[\%] \times Q[ln/min]} \times 10^{-6} \tag{4.2}$$

Where 24 L/mol is the molar volume at the reactor inlet (1 atm and 293.15 K), Q is the total gas volumetric flow rate, and 10^{-6} is the conversion factor from J to MJ.

We performed measurements in a wide range of operating conditions, i.e., volumetric flow rates ranging from 1 to 10 ln/min, electrical currents from 60 to 200 mA, and N_2 fractions ranging from 20 to 80%. All experiments were performed three times for each of the conditions, and the average values are taken over a 5-minute measurement period. We checked whether a 5-minute time period was sufficient, by also measuring the NO_x concentration over a long time (above 1 hour), and indeed, the NO_x concentration in the RGA's effluent quickly reaches a stable value, as demonstrated by the time evolution of the measured NO_x concentration, shown in Figure 7.9 in the appendix (Section 7.10.1). The reported values are the weighted averages, and the error bars are calculated based on the standard deviation of the results of each experiment from its

corresponding average value. More information about the experimental procedure, diagnostic device specification and calibration is given in the appendix (Section 7.10.2).

4.3 Results and discussion

4.3.1 Distinct operation modes of the reactor

The new configuration of our RGA reactor can operate in three different modes depending on the electrical current: (i) a rotating arc of variable length (rotating arc regime), (ii) a steady arc with stable length (steady arc regime), and (iii) a transition regime in which the plasma arc always switches between the two aforementioned arc regimes.

In GA plasma reactors, a plasma arc is created in the shortest gap between cathode and anode. In typical RGA plasma reactors, the arc immediately starts gliding along the reactor body due to the swirling gas flow. The elongation and rotation of the arc occur because it glides between the upper part of the cathode and interior surface of the reactor body (anode), and due to the presence of a swirling flow inside the reactor, respectively.

When powered by a current source, which is the case in our setup, the arc elongation is indicated by the almost linear rise in the discharge voltage (Figure 4.3 a). Upon increasing the arc resistance, due to elongation of the arc, the discharge current drops. During arc elongation, energy is dissipated into heat and radiation. Therefore, when the applied power is insufficient to maintain additional arc elongation, the arc extinguishes. This is presented by a sudden drop of the discharge current (Figure 4.3 a), and a reciprocal jump in the electrode voltage. Consequently, reignition occurs where the distance between the cathode and the anode is minimal, representing the typical operational mode of an RGA reactor. However, if certain conditions are met, the arc can stabilize due to the intense heat transfer to the reactor walls (so-called wall stabilization). In this steady arc regime, the provided power, by the power supply, is sufficiently high, enabling the extension of the arc until reaching the furthest possible contact point at the reactor outlet. In such a condition, the arc persists without extinguishing and maintains a relatively stable position at the reactor's center with a constant length. This stability can also be observed in the relatively constant values of both discharge voltage and current (Figure 4.3 b).

However, this change in arc regime does not occur abruptly. In our RGA plasma reactor, when coupled with the effusion nozzle, we observed that at low power (90 to 130 W) the reactor is always in the rotating arc regime. At intermediate power (135 to 185 W), the reactor is in a transition regime: although this power is enough for elongation of the plasma arc to the furthest contact point in the reactor outlet, it is not high enough for long term stabilization of the arc, like in the steady arc regime. Therefore, the plasma arc is always switching between steady and rotating regime (Figure 4.3 c). Eventually, at even higher power (> 190 W) the steady arc regime is achieved.

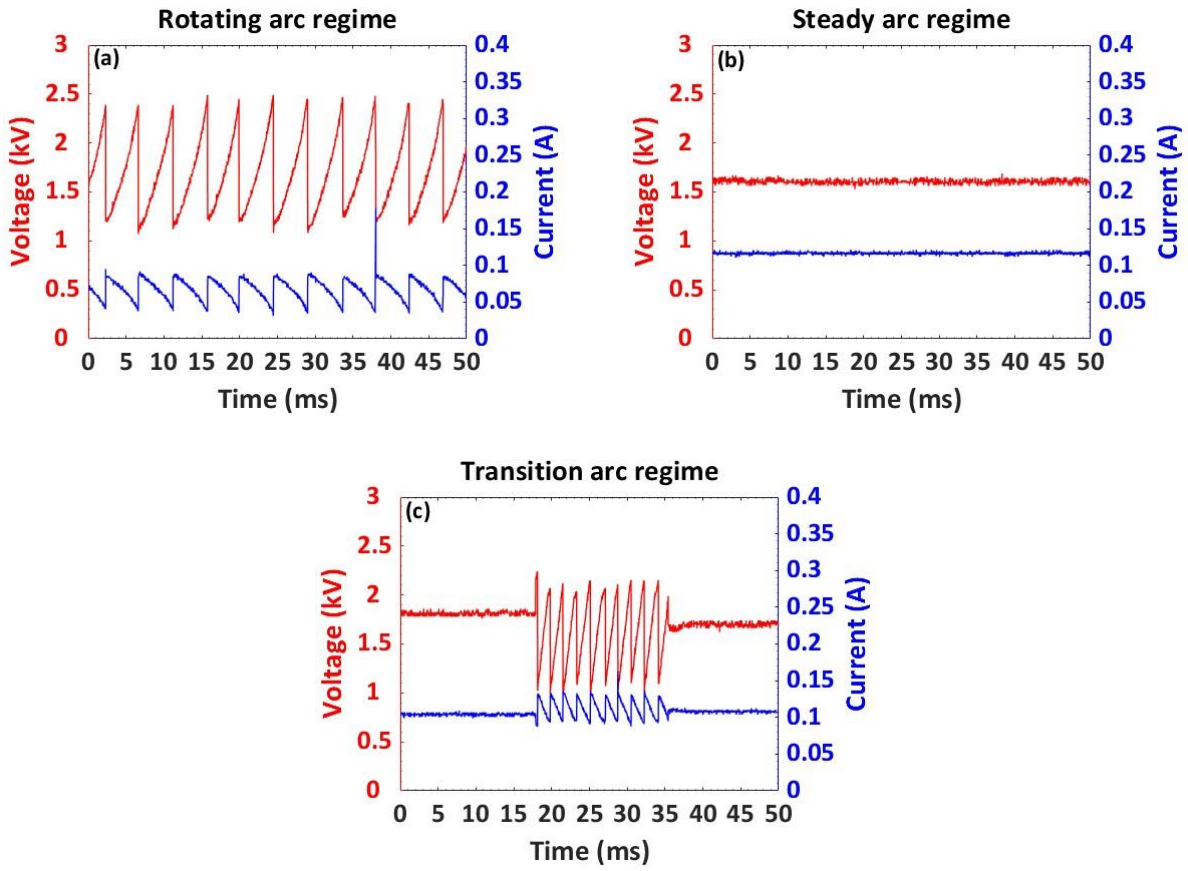

Figure 4.3. Current and voltage time evolution of the plasma arc operating in a) rotating, b) steady, and c) transition arc regime, for an N_2/O_2 ratio of 50/50 and gas flow rate of 2 ln/min.

These distinct operating regimes of our RGA reactor are also clear when we plot voltage as a function of applied current, in so-called V-I characteristics, recorded from the oscilloscope (Figure 4.4). When the reactor is supplied with around 60 mA, a voltage of about 1.7 kV dissipates into the plasma ($\mathrm{P} \approx 100$ W), the gas breaks down and a plasma is ignited, and the reactor starts to operate in the rotating arc regime. By increasing the current up to 80 mA, the reactor still operates in the rotating arc regime, and a higher current results in a lower voltage, characteristic for an arc plasma. Upon further increasing the current, the reactor operation mode enters the transition arc regime, which is reflected by a jump in the plasma voltage. The reactor stays in this regime up to a current of about 110 mA. As mentioned above, the plasma arc constantly switches between rotating and steady arc regime. Consequently, measuring the plasma V-I characteristics is quite difficult, which is reflected by the larger error bars determined for the measured plasma voltage. When the plasma current is above 120 mA, the plasma power is high enough ($\mathrm{P} \geq 190$ W) to sustain the elongated plasma arc and the reactor keeps operating in the steady arc regime.

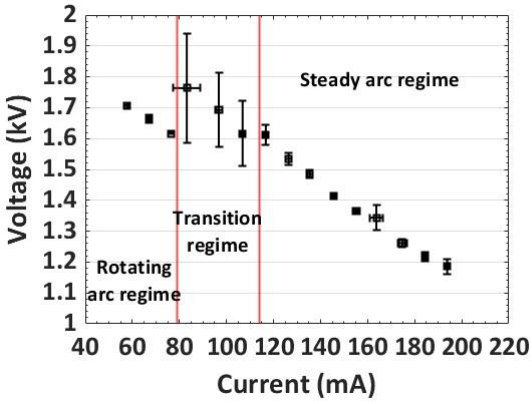

Figure 4.4. V-I characteristics of the RGA reactor, operating at different currents (yielding different plasma powers) for an N_2/O_2 ratio of 50/50 and gas flow rate of 2 ln/min.

4.3.2 Improvement in NO_x yield and EC due to the effusion nozzle: Effect of power and N_2 fraction

Figure 4.5 compares the performance of our reactor with and without the effusion nozzle, in terms of NO_x concentration (i.e., NO + NO_2), EC and supplied plasma power. As explained in section 4.3.1, our RGA reactor operates in three distinct regimes: (i) rotating arc mode at low power (90-130 W) where the arc rotates/glides along the reactor body, (ii) transition regime at intermediate power (135-185 W), and (iii) steady arc mode at power above 185 W, where the arc is stabilized due to the intense heat transfer to the reactor walls (so-called wall stabilization), and elongates until it reaches the furthest point of contact on the reactor outlet (schematically illustrated in Figure 4.1 above). In the last case, it remains there in a stable regime in the center of the reactor with constant length, and fills most of the reactor outlet, such that all of the incoming gas effectively passes through the plasma. Figure 4.5 shows the results for both rotating and steady arc regime, in a wide range of N_2 fractions in the feed gas.

In the rotating arc regime, for N_2 fractions below 50%, the effusion nozzle allows ignition and sustainment of the plasma arc at lower power values than without nozzle (Figure 4.5 e), reaching about the same NO_x concentration (Figure 4.5 a). For N_2 fractions above 50%, slightly higher power should be supplied as without nozzle, but higher NO_x concentrations are achieved. The effect of either lower power (for the same NO_x concentration) or higher NO_x concentration yields a slightly lower EC for each N_2 fraction, with on average 4.5% improvement, and the largest improvement of 7.3% for an N_2 fraction of 80, mimicking dry air composition (Figure 4.5 c).

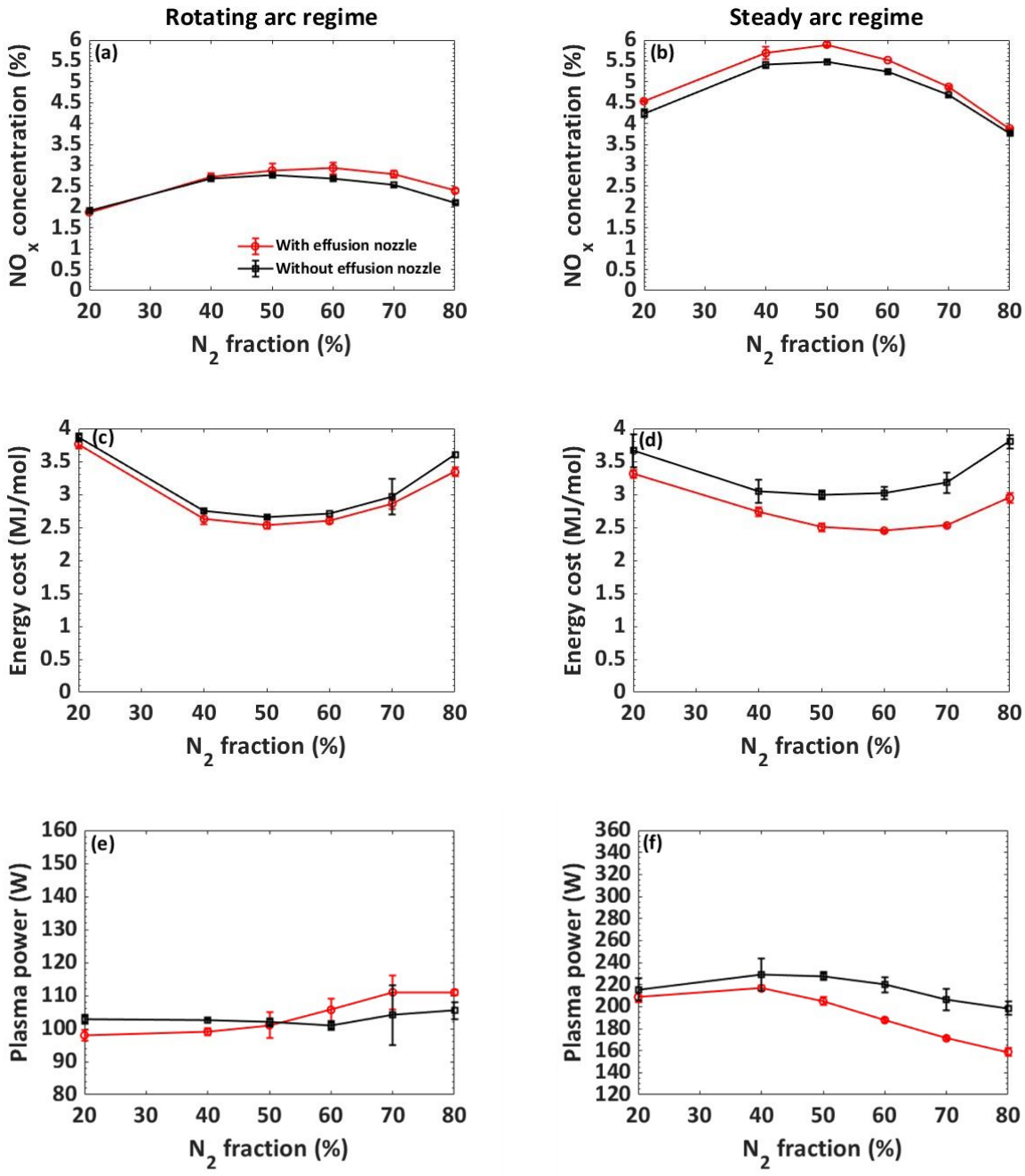

Figure 4.5. Measured NO_x concentration (a, b), EC (c, d) and plasma power (e, f) in the RGA plasma reactor operating with and without the effusion nozzle, as function of N_2 fraction in the mixture, in rotating (left) and steady (right) arc regimes. The applied current in the rotating arc regime was between 60 and 120 mA, while it was between 120 and 200 mA in the steady arc regime. The total flow rate was fixed at 2 ln/min.

In the steady arc regime, a lower power can sustain the arc across the entire range of N_2 fractions when it is operating with the effusion nozzle (Figure 4.5 f). Moreover, the effusion nozzle also results in slightly higher NO_x concentrations (improvements up to 8%) (Figure 4.5 b). Because of

both, the EC with the effusion nozzle drops on average by 16.3% over the entire range of N_2 fractions compared to without nozzle, with the largest improvement of about 22.5% at N_2 fraction of 80% (i.e., dry air composition). Overall, our best results are obtained in the steady arc regime, at an N_2 fraction of 50%, yielding a NO_x concentration of 5.9%, at an EC of 2.5 MJ/mol, but an N_2 fraction of 60% yields an even slightly lower EC of 2.4 MJ/mol.

4.3.3 Effect of gas volumetric flow rate on the NO_x yield and process EC

Figure 4.6 compares the performance of the RGA plasma reactor with effusion nozzle at different flow rates for both rotating and steady arc regime, in terms of NO_x concentration and EC, as a function of N_2 fraction. It should be noted that flow rates of 1 and 1.5 ln/min always resulted in the steady arc regime, even at low power, which normally results in the rotating arc regime. Indeed, at these low flow rates, the plasma arc could already elongate and reach the furthest point of contact at the reactor outlet. Nevertheless, the data of 1 and 1.5 ln/min at these lower power values are also plotted in the figures of the rotating arc regime, to compare them with the other data at this lower power.

In both rotating and steady arc regime, the NO_x concentration decreases with increasing flow rate, due to the shorter gas residence time inside the plasma (Figure 4.6 a and b). In the rotating arc regime, the highest NO_x concentration of 4.7% was measured at a flow rate of 1 ln/min, but the results are very similar at 1.5 ln/min. In the steady arc regime, the highest NO_x concentration is about 6%, measured at a flow rate of 1 ln/min, but again the results are very similar at 1.5 and even 2 ln/min.

The lowest flow rates also require the lowest power to sustain the plasma, in both rotating and steady arc regime (Figure 4.6 e and f), but because the SEI is the ratio of power over flow rate, the EC is not the lowest at these low flow rates; even more, in the steady arc regime, the lowest flow rate gives rise to the highest EC (Figure 4.6 c and d). In the rotating arc regime, the lowest EC is 2.1 MJ/mol, at a flow rate of 1.5 ln/min (Figure 4.6 c), while in the steady arc regime, the lowest EC is 2.3 MJ/mol, at a flow rate of 4 ln/min. Note however that the EC in the steady arc regime does not change considerably upon changing flow rate, certainly not at more O_2-rich mixtures.

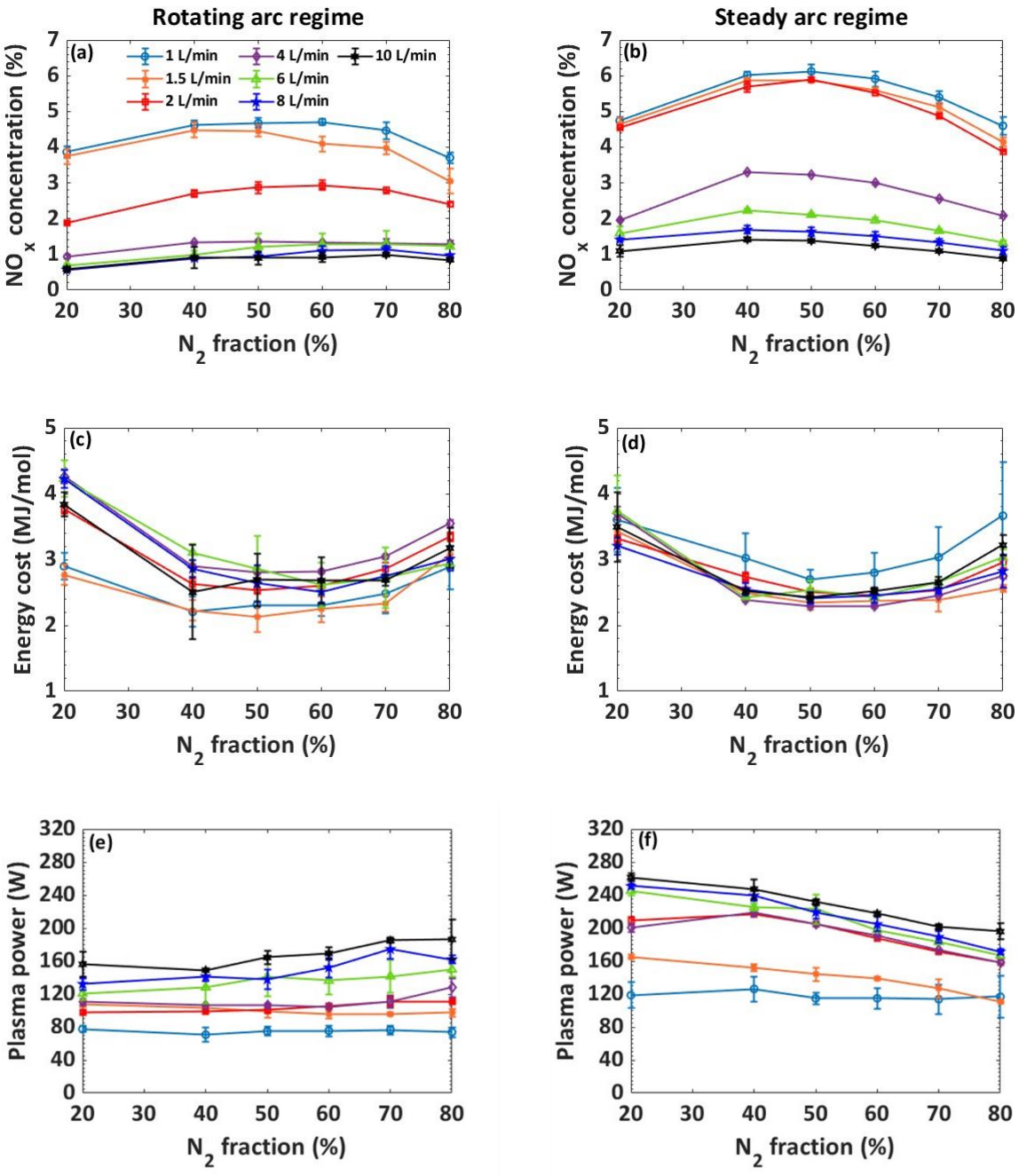

Figure 4.6. Effect of total gas flow rate on the performance of the RGA reactor with effusion nozzle, in terms of NO_x yield (a, b), EC (b, c), and plasma power (e, f), for the rotating (left) and steady (right) arc regimes. Note: a steady arc was formed at flow rates of 1 and 1.5 ln/min for the entire range of N_2 fractions, even at low power, but these data are still plotted in the left panels, as they were obtained at similar power as the other data in the rotating arc regime.

4.4 Conclusion

The high energy consumption of plasma-based NO_x synthesis was mentioned as one of the biggest obstacles of industrialization of this process. In this chapter, to tackle this problem, we presented a novel design, called “effusion nozzle”, to improve the performance of an RGA plasma reactor for NO_x production. We performed experiments in a wide range of applied power, gas flow rates and N_2 fractions, and our results indicate an enhancement in NO_x concentration by 8%, as well as a reduction in EC by 22.5%. In absolute terms, we obtained NO_x concentrations up to 5.9%, at an EC down to 2.1 MJ/mol. These results were the best values obtained up to the time that this study was published in Chemical Engineering Journal (CEJ) [151].

As mentioned before in section 4.1 our obtained ECs are not yet competitive with the combined HB and Ostwald process. Indeed, according to the techno-economic study performed by Rouwenhorst et al. [17], the EC of plasma-based NO_x production must be reduced to 1.1-1.5 MJ/mol in order to compete with the industrial HB and Ostwald process. Hence, further efforts will be needed to improve the performance. Although our results do not yet reach the requirements for industrialization of plasma-based NO_x synthesis, they clearly show that improving energy efficiency of this process is feasible through modifications in plasma reactor design.

To understand why the effusion nozzle yields improved performance, my colleague Senne Van Alphen, used a modelling strategy consisting of four complementary models. Although this modelling approach did not reach complete agreement with the measured NO_x concentrations, it could reasonably explain the improved performance obtained by the effusion nozzle. Indeed, his model shows that fast cooling occurs as soon as the gas molecules collide with the effusion nozzle, which acts as a very efficient heat sink. This fast drop in temperature limits the recombination of NO with N and O atoms into N_2 and O_2, i.e., the backward reactions of the so-called Zeldovich mechanism, and thus it limits the decrease in NO_x concentration after the plasma. Indeed, this decrease is more pronounced without the effusion nozzle, due to the slow drop in temperature after the plasma. Hence, he could explain the higher NO_x concentration observed experimentally in case of the effusion nozzle. Furthermore, because the effusion nozzle allows ignition and sustainment of the plasma at somewhat lower power, still producing the same (or even slightly higher) NO_x concentrations, this also explains the lower energy cost observed experimentally.

5 Scaling up energy-efficient plasma-based nitrogen fixation[1]

[1] This chapter is submitted for publication at Sustainable Energy & Fuels.

5.1 Introduction

In addition to challenges related to plasma catalysis and achieving high energy efficiency, as explained in chapter 1, section 1.7, we also need to address reactor engineering challenges to build a scaled up reactor that is efficient enough for the industrial application of plasma-based NF [6]. Furthermore, over the past century, the HB process has been significantly optimized to very low EC of about 0.5 MJ/mol [17]. This also presents the biggest challenge for the plasma-based process: the EC depends on both the SEI and NO_x concentration: a higher SEI typically yields a higher NO_x concentration, but when the NO_x concentration does not rise more than the SEI, the corresponding EC will rise as well. In other words, upon rising SEI, the NO_x concentration should rise faster to keep a good EC. Several plasma discharges have been explored already for NO_x production.

Several studies on plasma-based NO_x production were summarized in chapter 4, section 4.1. Here we summarize the reported NO_x concentration and EC for plasma-based NO_x production at various SEI values for different plasma types; see Figure 5.1. Except for the Birkeland-Eyde process, all other reported plasma processes have been operated in lab scale reactors. Indeed, scaling up of plasma-based NF with a low EC and high NO_x concentration remains a big challenge for the industrialization of this process.

In the present chapter, we try to tackle this challenge by developing a low current, high flow rate plasma reactor and comparing the results to a smaller counterpart. In this way, we are able to scan a large SEI range and investigate the potential of scaling up the NF process. The high flow rates of the feed gas, up to 300 ln/min, allow to increase the PR, even at low NO_x concentrations. This effect, in combination with elevated pressure, can potentially enhance the industrial applicability of plasma-based NF. Finally, we apply a simple approach, based on thermodynamic equilibrium calculations, to estimate the flow rate passing through the region with elevated temperature, as well as the gas temperature, in order to better explain our experimental results.

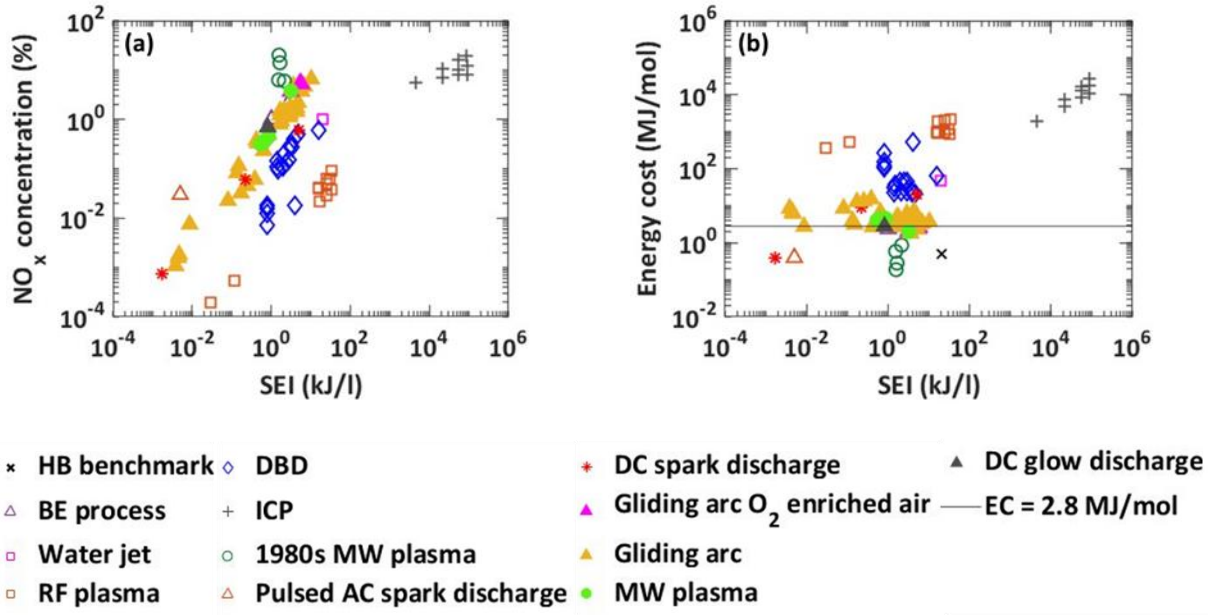

Figure 5.1. Reported NO_x concentration (a) and EC (b) of plasma-based NO_x production, as a function of SEI in different plasma systems, including 1980s low pressure MW plasma, MW plasma at atmospheric pressure, GA, RF plasma, DBD, ICP, spark discharge, and DC glow discharge. The horizontal line in (b) corresponds to the EC of 2.74 MJ/mol, which is the minimum thermodynamic equilibrium EC for atmospheric pressure NF (as discussed further in this paper). Only some low-pressure plasmas produce a lower EC, demonstrating they are characterized by thermodynamic non-equilibrium. Among the atmospheric pressure plasmas (more suitable for upscaling and industrial implementation), warm plasmas, such as GA, MW and DC glow discharge plasmas (all indicated with solid symbols), show the best performance in terms of both NO_x concentration and EC (close to the thermodynamic equilibrium limit), as explained in the text.

5.2 Experimental setup

In order to test the effects of upscaling, we used two different plasma reactors in this work, i.e., a large one and its smaller counterpart, but based on the same operating principle, i.e., pin-to-pin configuration, powered by the same DC current-controlled power supply and operating in the low-current arc regime. Arc discharges are characterized by electron emission at the cathode being either field or thermionic emission or a combination of both [152]. Although at very low currents (< 50 mA) they can exhibit non-equilibrium effects, in the current range of 200 – 1000 mA (as in our study), arc discharges in air are typically in local thermodynamic equilibrium [153]. This current range, in combination with a wide range of flow rates, being applicable to either the small or large reactor, allows us to cover a wide SEI range of 0.1 – 7.6 kJ/l. The small reactor operates from 0.9 – 7.6 kJ/l, i.e., a high SEI region. The large reactor only operates at lower SEI, i.e., 0.1 – 1 kJ/l, because of the high flow rates, but not very high power (limited by the power supply unit (PSU); see section 5.2.2). Besides the pin-to-pin configuration (like its smaller counterpart), it can also operate in another, so-called torch configuration (see below).

5.2.1 Small reactor

A schematic representation of the small reactor is presented in Figure 5.2.

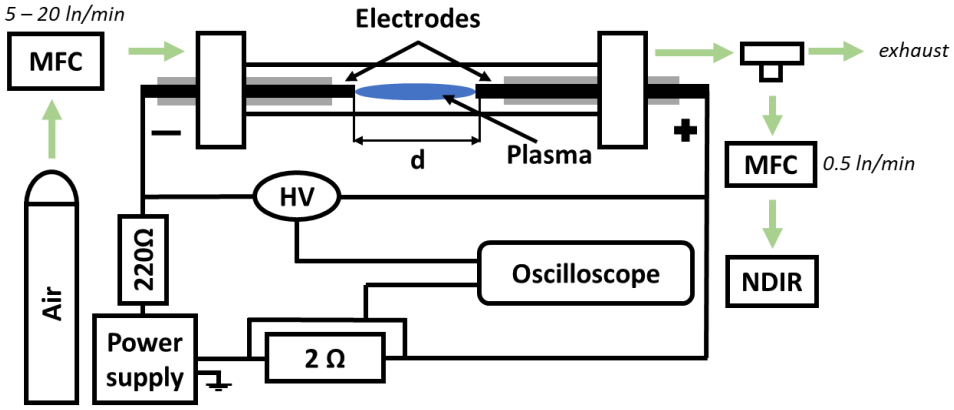

Figure 5.2. Schematic representation of the small reactor, with plasma (indicated in blue) ignited between the two opposing electrodes (indicated in black).

A compressed air cylinder was connected to a mass flow controller (MFC, Bronkhorst F-210CV), which supplied the gas flow to the reactor (5, 10, 15, 20 ln/min at STP conditions). The mass flow rate is indicated in ln/min (normal liters per minute), which refers to reference conditions of 0 °C and 1 bar, consistent with the definition of the MFC manufacturer, who defines normal liters at 0 °C.

The plasma was generated between two cylindrical stainless-steel electrodes (8 mm in diameter, indicated in black in Figure 5.2) placed inside a quartz tube with 16 mm inner and 20 mm outer diameter. The electrodes were insulated from the body of the reactor by an Al_2O_3 tube placed around them (indicated in grey in Figure 5.2). The distance between both electrodes (d in Figure 5.2) was varied between 7 and 14 cm. The reactor volume is 14.1 and 28.2 cm^3 for d = 7 and 14 cm, respectively.

The concentration of NO and NO_2 was measured using a non-dispersive infrared (NDIR) detector (Emerson, Rosemount X-stream enhanced XEGP continuous gas analyzer). The NDIR was calibrated using calibration gases (16.02 vol% NO in He, 7.80 vol% NO_2 in He) purchased from Praxair. Although the calibration gases are diluted in He, this calibration is still valid for NO_x production in air, because they are mimicking the target gases absorption characteristics due to the inert nature of helium, and the fact that it does not interfere with the absorption features of NO and NO_2. Note that the measurement device could only detect NO and NO_2 (which we denote here collectively as NO_x). Each experiment was conducted three times to obtain the standard deviation. The current applied to the reactor was varied between 200 and 500 mA. Details of the power supply unit (PSU) are mentioned in section 5.2.4.

5.2.2 Large reactor

As mentioned above, the large reactor can operate both in a pin-to-pin and torch configuration, with the plasma being stabilized by a swirling flow. Experiments without swirling flow were also conducted, but the plasma stability was significantly reduced. A schematic of the experimental setup of the large reactor in pin-to-pin configuration is presented in Figure 5.3.

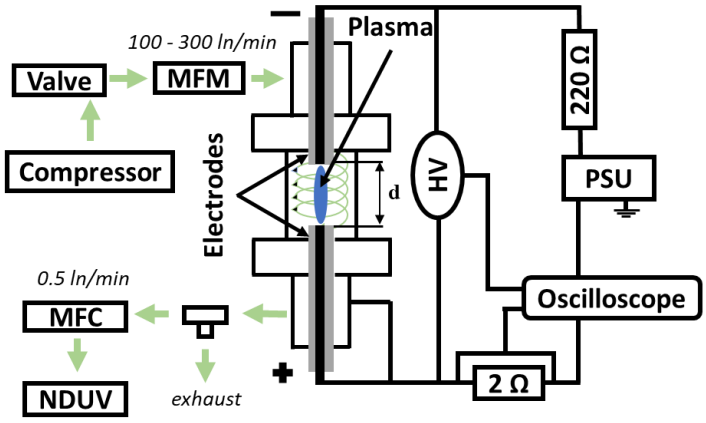

Figure 5.3. Schematic representation of the large reactor, with plasma (indicated in blue) ignited between the two opposing electrodes (indicated in black) and the swirling flow around the plasma (indicated in green).

The reactor consists of two Wla electrodes with diameter of 30 mm, encased in 40 mm Si_3N_4 insulation (indicated in black and grey in Figure 5.3, respectively). The electrodes are placed within a stainless-steel tube with inner diameter of 63 mm and outer diameter of 73 mm. The distance between both electrodes (d in Figure 5.3) was also varied between 7 and 14 cm. The reactor volume is 218.2 and 436.4 cm^3 for d = 7 and 14 cm, respectively, hence more than 10 times larger than its smaller counterpart. When investigating the reactor in torch configuration (see schematic diagram in section 5.2.3, Figure 5.4), the bottom electrode was removed, and the reactor body acted as grounded electrode. Note that we evaluate this torch configuration to overcome the limitations of the pin-to-pin configuration, as explained in the Results and Discussion section.

An air compressor is connected to a control valve, which in turn is connected to the reactor through a mass flow meter (MFM) (IFM SD6500), which supplies the flow rate to a helical swirl generator. The current was varied between 300 and 1000 mA, and the flow rate of air between 100 ln/min and 300 ln/min. The PSU (at lab scale) did not allow to apply power above 2500 W, or current above 1000 mA. This, in combination with the high flow rates, is the reason why this reactor only operates in the low SEI region of 0.1 – 1 kJ/l, as mentioned above. The NO and NO_2 concentrations were measured by non-dispersive ultraviolet spectroscopy (NDUV) using a WiTec ULTRA-Sens NO_x AK100 TBH gas analyzer, calibrated similarly to NDIR as described above. Note

that the gas analyzer could only detect NO and NO_2 (collectively denoted as NO_x). The reason for using a different gas analyzer for the large reactor is that the NDIR detector, used for the small reactor, is not accurate for measuring NO_x concentrations lower than 1% (i.e., in the ppm range), while the produced NO_x concentrations in the large reactor are always below 0.5% (see below).

5.2.3 Large reactor in torch configuration

A schematic of the large reactor in torch configuration is presented in Figure 5.4. The reactor setup was the same as in pin-to-pin configuration, except that the bottom electrode was removed, and the reactor body acted as the grounded electrode. Therefore, when the gas breaks down due to the applied voltage of 10 kV by the power supply, a plasma forms between the electrode and the reactor body.

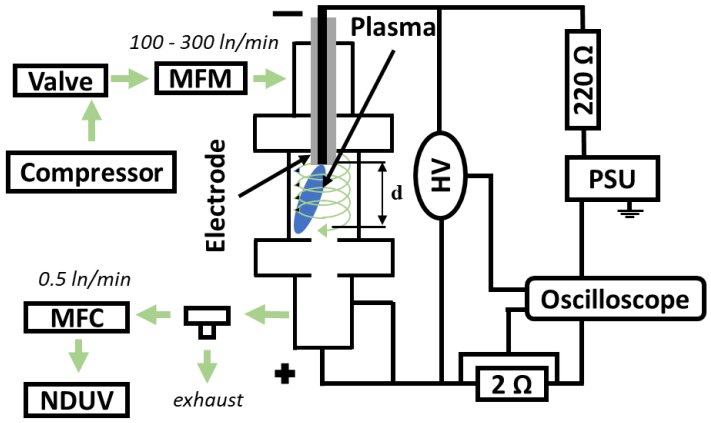

Figure 5.4. Schematic representation of the large reactor in torch configuration, with plasma (indicated in blue) ignited between the electrode (indicated in black) and the reactor body, and the swirling flow around the plasma (indicated in green).

5.2.4 Definition of the performance metrics

For both reactors, the voltage was measured with a high voltage probe (HV) (Tektronix P6015A) and the current was obtained by measuring the voltage drop across a shunt resistor with 2 Ω resistance. Both signals were recorded with a two-channel oscilloscope (Keysight InfiniiVision DSOX1102A). The current was supplied with a current-controlled PSU (Technix SR12KV-10KW) with negative output polarity, for both reactors.

The plasma power was calculated by averaging the instantaneous power measurements as:

$$P\ [W] = \frac{1}{n}\sum_{i=1}^{n} V_i \times I_i = \frac{1}{n}\sum_{i=1}^{n} V_{plasma_i} \times \frac{V_{shunt_i}}{R_{shunt}} \tag{5.1}$$

Where n is the number of recorded points (in the order of thousands, depending on the oscilloscope settings), V_{plasma_i} is the voltage drop across the plasma discharge, V_{shunt_i} is the voltage drop across the shunt resistor and R_{shunt} is the resistance of the shunt resistor. In order to calculate the power, three scopes are taken and then averaged for each of the experimental conditions. Examples of the voltage and current scopes are presented in section 5.2.5, Figure 5.5. For the small reactor, we observed a periodic signal, oscillating around the current value set on the power supply and the burning voltage. For the large reactor, we observed a rather random behaviour, with longer periods of stability but stronger voltage and current peaks, indicating restriking (see, section 5.2.5).

The SEI is calculated from the plasma power and the total gas flow rate as:

$$SEI\ \left[\frac{kJ}{l}\right] = \frac{P\ [W]\ \times\ 60\ \left(\frac{s}{min}\right)}{flow\ rate\ [ln/min]} \times 10^{-3}\left[\frac{kJ}{J}\right] \tag{5.2}$$

The EC is calculated from the total measured NO_x (NO + NO_2) concentration, the power and flow rate (which both define the SEI), as:

$$EC\ \left[\frac{MJ}{mol}\right] = \frac{P\ [W]\ \times\ 22.4\ \left(\frac{ln}{mol}\right)\ \times\ 60\ \left(\frac{s}{min}\right) \times 100[\%]}{total\ NO_x\ concentration\ [\%]\ \times flow\ rate\ [ln/min]} \times 10^{-6}\left[\frac{MJ}{J}\right] \tag{5.3}$$

Where 22.4 ln/mol is the molar volume at normal conditions as explained above.

The production rate (PR) is calculated as follows:

$$PR_{NO_x}\left[\frac{g}{h}\right] = \frac{\left(\ x_{NO} \times\ 30\ \left[\frac{g}{mol}\right] + x_{NO_2}\ \times\ 46\ \left[\frac{g}{mol}\right]\right)\ \times\ flow\ rate\ [ln/min]}{22.4\ \left[\frac{ln}{mol}\right]} \times 60\left[\frac{min}{h}\right] \tag{5.4}$$

Where x_{NO} and x_{NO_2} are the fraction of NO and NO_2 in the gas flow after the plasma. In equation (5.3) and (5.4), the change of the volume due to the stoichiometry of NO_2 formation is neglected, because the main product is NO, while NO_2 is formed at very low amounts (less than 2 % for all conditions). The NO_x concentration was measured after the reactor performance has achieved steady state, and there are no changes in concentration as a function of time. In addition, each of the experiments was also conducted three times, in order to reduce the uncertainty. The error bars are present in all figures, but in some cases, they are too small to be visible.

5.2.5 Voltage-Current characteristics for the small and large reactor

The temporal behaviour of plasma voltage and current for the small reactor and its larger counterpart in the pin-to-pin and torch configuration are shown in Figure 5.5 a-d. Applying a potential difference of about 10 kV in between the electrodes, results in the gas breakdown and formation of an arc discharge in the space between the electrodes (or between the electrode and the reactor body, for the torch configuration) which starts to glide along the exposed part of the electrode. While the arc is gliding, energy is dissipated into heat and radiation in the small reactor, despite that a rather stable plasma was observed, the voltage and current are periodically oscillating around the current value set on the power supply (Figure 5.5 a and b). For the large reactor in pin-to-pin configuration, we observed a rather random behaviour with longer periods of stability. Again, the voltage and current are oscillating around the mean voltage value and the set current value on the power supply (Figure 5.5 c), however, these oscillations are stronger than for its smaller counterpart. For the large reactor in torch configuration, the fluctuation of voltage and current is less pronounced than in pin-to-pin configuration, but still a random behaviour of stability periods was observed (Figure 5.5 d). These relatively strong oscillations of the voltage and current as a function of time, together with the random behaviour of stability periods, indicate that the large reactor, in both pin-to-pin and torch configuration, is operating in a restriking regime [154,155].

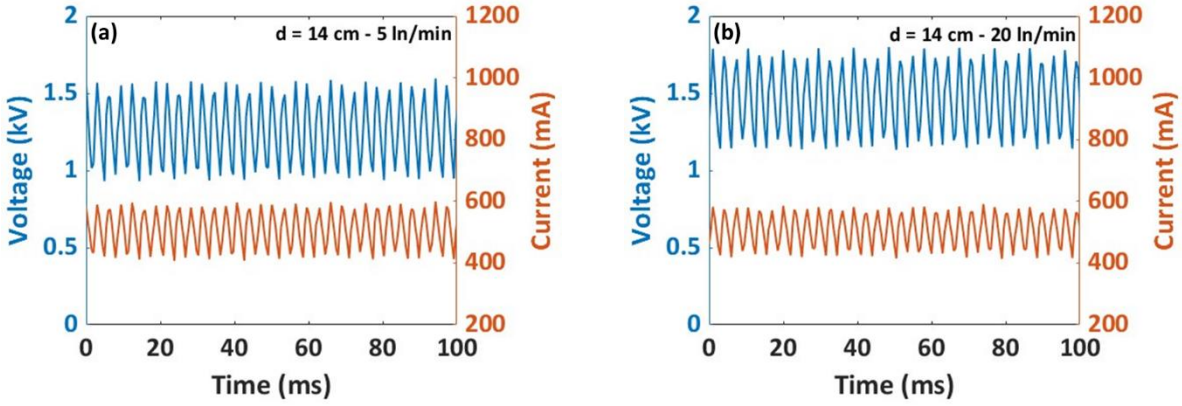

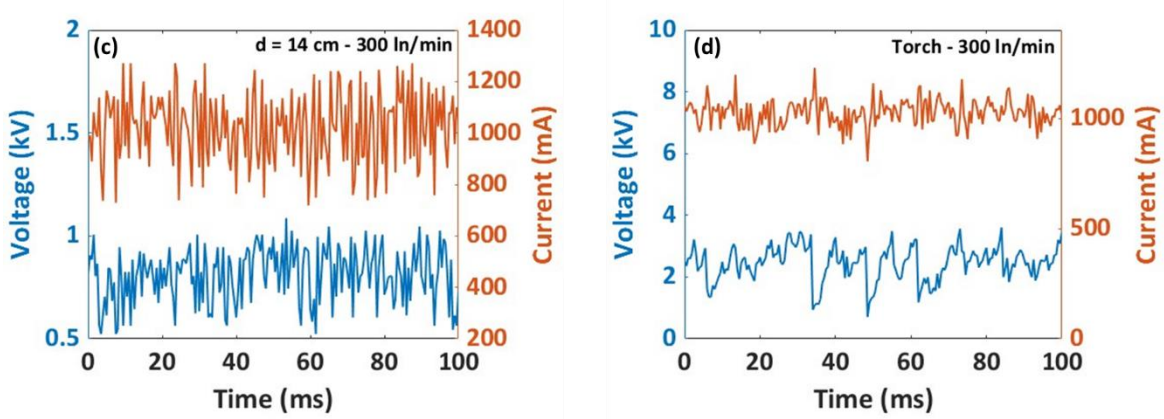

Figure 5.5. Temporal behavior of plasma voltage and current for a distance between the electrodes of 14 cm, in the small reactor operating at 5 and 20 ln/min and applied current of 500 mA (a and b, respectively), the large reactor in pin-to-pin configuration (c), and in torch configuration (d), both at 300 ln/min and applied current of 1000 mA.

5.3 Model description

In order to explain our experimental results, we developed a simple model based on thermodynamic equilibrium considerations. The EC associated with thermodynamic equilibrium was calculated by estimating the energy needed to heat the gas in the temperature range of 300 – 6000 K, which is a sufficiently wide range for plasmas at atmospheric pressure. We used the following relation:

$$q = \int_{300}^{T_2} C_p(T)dT \tag{5.5}$$

Where q is the energy needed to heat one kg of gas, $Cp(T)$ is the heat capacity as a function of temperature (here in J kg^{-1} K^{-1}), and T_2 is the temperature to which we are heating the gas. We can then multiply this energy by the thermodynamic equilibrium NO concentration for temperature T_2 to determine the EC for NO formation as a function of temperature. Following the same idea, we can calculate the power needed to heat a given mass flow of gas to a given temperature T_2:

$$P = \dot{m} \int_{300}^{T_2} C_p(T)dT \tag{5.6}$$

Where P is the power needed to heat the gas, and $\dot{m}$ is the mass flow rate (in kg/s, but later converted to ln/min). The heat capacity of the gas as a function of temperature was obtained

from a zero-dimensional model for calculating the equilibrium composition as a function of temperature using COMSOL Multiphysics 6.0 [156]. The model includes five species: N_2, O_2, N, O, NO. NO_2 is not included in the model because oxidation from NO to NO_2 happens in the post-plasma region [141], and our experiments reveal anyway that NO_2 is formed at less than 2% of the NO concentration for all conditions, see previous section. The chemical reactions considered are presented in Table 5.1, with their respective rate coefficients, for the forward reaction. The detailed balance principle was used for calculation of the reverse rate coefficients.

The temperature-dependent enthalpy of the considered species, used to calculate the heat capacity, is taken from the NASA Glenn polynomials [157]. The model was used to calculate the equilibrium NO concentration as a function of temperature, as well as the heat capacity of the mixture as a function of temperature, used to calculate the energy needed to heat the gas to a certain temperature, from which the EC is obtained to reach the equilibrium NO concentration at a certain temperature:

$$\mathrm{EC}\left[\frac{MJ}{mol}\right] = \frac{q\left[\frac{J}{Kg}\right]\times 29\times 10^{-3}\left[\frac{kg}{mol}\right]}{x_{NO}} \times 10^{-6}\left[\frac{MJ}{J}\right] \tag{5.7}$$

Where x_{NO} is the mole fraction of NO calculated by the model.

Table 5.1. Chemical reactions considered in the model.

	Reaction*	Rate coefficient forward reaction [m^3/s]	Ref.
(1)	$N_2 + M \rightleftharpoons N + N + M$	$5\times 10^{-8}\left(\frac{-133200}{T}\right)\times\left(1-\exp\left(\frac{-3354}{T}\right)\right)$	[158]
(2)	$O_2 + M \rightleftharpoons O + O + M$	$3.7\times 10^{-8}\exp\left(\frac{-59380}{T}\right)\times\left(1-\exp\left(\frac{-2240}{T}\right)\right)$	[158]
(3)	$N_2 + O \rightleftharpoons NO + N$	$9.7\times 10^{-21}\times \mathrm{T}^{1.01}\times\exp\left(\frac{-3120}{T}\right)$	[159]
(4)	$O_2 + N \rightleftharpoons NO + O$	$3\times 10^{-16}\times\exp\left(\frac{-38000}{T}\right)$	[159]

* M is any molecule in the gas.

5.4 Results and discussion

As mentioned in section 5.2, we investigated the performance of the two different plasma reactors, to obtain more insights in the effects of upscaling. Due to the clearly different range in

flow rates of the small and large reactor, while using the same PSU (see above), both reactors operate in a different SEI range. The small reactor operates in a pin-to-pin configuration with axial flow going through the plasma region. By using a current-controlled PSU, we varied the current between 200 – 500 mA, for flow rates of 5, 10, 15 and 20 ln/min. In addition, we investigated the effect of the interelectrode spacing, by varying the distance between the electrodes between 7 and 14 cm. This configuration covers the high SEI range, with maximum value of 7.6 kJ/l.

To investigate the potential of scaling up plasma-based NF, we developed a larger version of this reactor, which can operate both in pin-to-pin and torch configuration. The latter configuration is put forward as a solution to overcome the limitations of the pin-to-pin configuration, as explained below. The large reactor is operated by the same PSU, but the current range could be extended from 300 to 1000 mA, with flow rates of 100, 200 and 300 ln/min. As explained above, this yields a lower SEI range, because the PSU could not supply higher current. In addition, the distance between the electrodes was also varied between 7 and 14 cm in the pin-to-pin configuration.

Last but not least, in order to aid the analysis of our experimental results and obtain more insight in the effects of upscaling, we performed calculations based on thermodynamic equilibrium considerations. For all of the conditions, we are reporting the total NO_x concentration (being $NO+NO_2$).

5.4.1 Small reactor

The plasma in the small reactor could not be sustained in the full current range between 200 and 500 mA for all gas flow rates; see Figure 5.6, which depicts the plasma power as a function of current. More specifically, we observed two regimes of plasma operation as a function of flow rate, as presented by the photographs in Figure 5.7. With increasing gas flow rate, the discharge transitions from a stable and rather diffuse column (Figure 5.7, at 5 ln/min) to a more contracted and oscillating column (Figure 5.7, at 20 ln/min), which reduces the stability at low currents. The blue region in Figure 5.7 is the current-conducting region of the discharge, while the orange glow observed around the core is the NO_2 emission, as also observed by Machala et al. [160]. Furthermore, upon increasing current, the plasma starts gliding along the exposed part of the electrode, leading to a longer discharge, not corresponding to the exact distance between the electrodes. We note that despite the plasma was stable for 5 ln/min, the voltage and current as a function of time were oscillating around the mean voltage and current values (c.f., section 5.2.5, Figure 5.5 a). Furthermore, there is a bright contracted spot on the cathode, indicating the plasma operates in the arc regime.

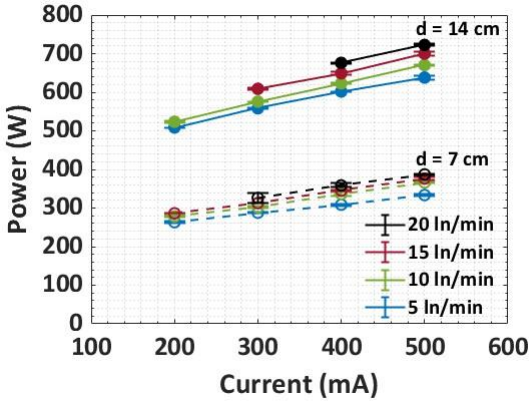

Figure 5.6. Plasma power as function of applied current, for the four different flow rates and two different distances between the electrodes (dashed lines/open symbols, and solid lines/closed symbols, for d = 7 and 14 cm, respectively). Error bars are indicated by the horizontal lines; the actual values are too small to be visible.

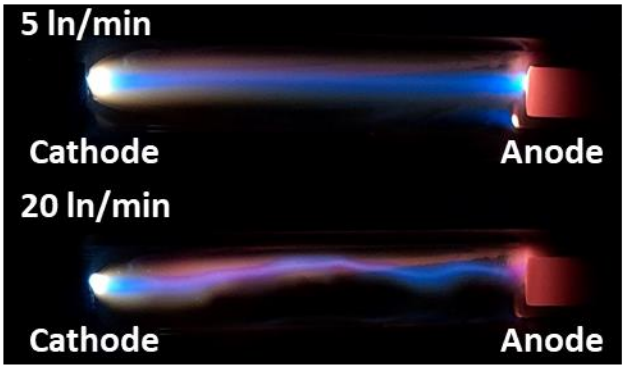

Figure 5.7. Transition of plasma regime upon increasing feed gas flow rate, from a stable and diffuse column at 5 ln/min, to a contracted and oscillating column at 20 ln/min. Both images are taken at the same current of 500 mA.

As mentioned, Figure 5.6 illustrates the plasma power as a function of applied current, for the four different flow rates and two different distances between the electrodes. The plasma power linearly rises with current for both 14 and 7 cm, and for all flow rates. This trend is natural for plasma sustained between two opposing electrodes [160]. As the gas flow rate increases, we observe an increase in plasma power, due to the enhanced convective losses. Indeed, the plasma becomes more resistive, and a higher voltage is required to sustain the discharge at the same current. For example, we can see a 53 W increase in power between 5 and 20 ln/min for 500 mA and 7 cm distance between the electrodes. This behavior is consistent with the modelling of a similar type of discharge in N_2 in a study by Tsonev et al. [161].

When the distance between the electrodes increases from 7 to 14 cm, the gas flow rate has a stronger effect on the voltage required to sustain the discharge, because of the enhanced interaction between plasma and gas flow. As a result, there is a larger increase in power for 14 cm distance between 5 and 20 ln/min flow rates, e.g., for 500 mA, the difference is 85 W. As the distance between the electrodes increases, we expect the power to rise with the same factor. In Figure 5.6, we indeed observe a rise in power by nearly a factor of two for all investigated conditions. For 5 ln/min, the rise in power between 7 and 14 cm is roughly 1.91 for all currents, while for 20 ln/min it is 1.87.

The measured NO_x concentration as function of current, for the different flow rates and distances between the electrodes is presented in Figure 5.8. For all conditions we observe a rise in NO_x concentration as a function of current and distance between the electrodes and a drop as a function of flow rate. The highest NO_x concentration is 3.51%, for a current of 500 mA, a flow rate of 5 ln/min and distance between the electrodes of 14 cm. For 7 cm distance between the electrodes, despite the linear behavior in power as a function of current (Figure 5.6), we see a nonlinear behavior in the NO_x concentration for 10 and 15 ln/min (Figure 5.8a), while for 5 and 20 ln/min we do observe a nearly linear relationship. For 14 cm distance (Figure 5.8 b) a nonlinear rise in NO_x concentration is observed only for 10 ln/min, while the other flow rates yield a nearly linear trend.

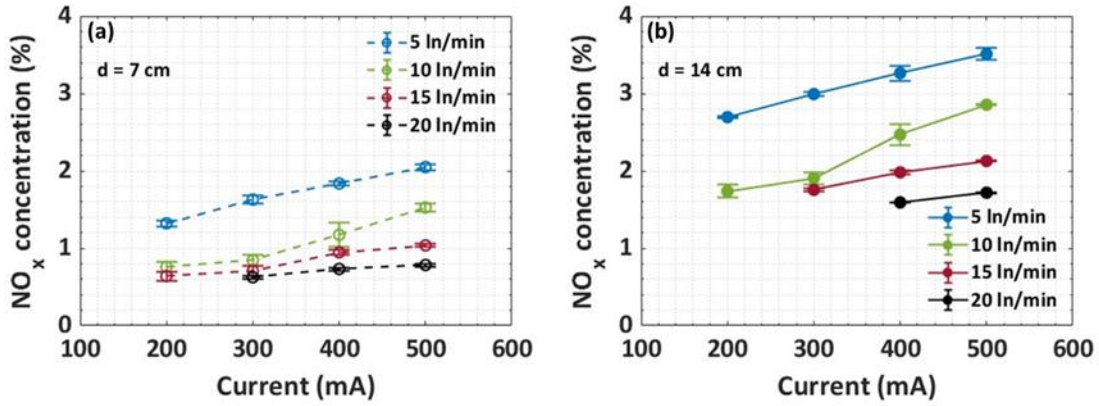

Figure 5.8. Total NOx concentration as function of current, at different flow rates, for (a) 7 cm and (b) 14 cm, in the small reactor. Error bars are indicated but are often too small to be visible.

Doubling the distance between electrodes does not result in the same rise in NO_x concentration, despite the nearly linear relationship for power (Figure 5.6). For example, at 500 mA, the ratio of the NO_x concentration between 7 and 14 cm is 1.71 for 5 ln/min and 2.19 for 20 ln/min. This shows that increasing the distance between electrodes, and thus the length of the plasma, is a crucial parameter. The result is most striking at 20 ln/min, where the rise in power was only 1.87. For the larger electrode distance, the relative increase in NO_x concentration is thus higher than

the relative increase in power, and as a result, the process is overall improved in terms of EC (see Figure 5.9).

Indeed, in order to more clearly present the relationship between power and produced NO_x concentration, we plot in Figure 5.9 the results for both EC and NO_x concentration as a function of SEI, for the different flow rates and distances between the electrodes. As mentioned before, the SEI is the ratio of power over flow rate (equation (5.2)), and it is an important parameter to determine the reactor performance. We clearly see a drop in the EC and a rise in the NO_x concentration as function of SEI in the entire SEI range. This indicates that the performance, both in terms of NO_x concentration and EC, would further improve upon higher SEI. We will investigate this in future work, when we have a PSU that can produce higher power.

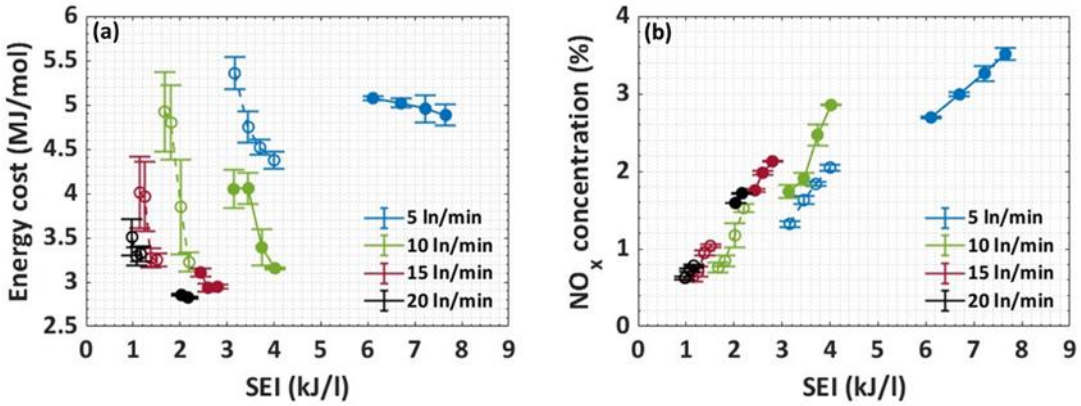

Figure 5.9. EC (a) and NO_x concentration (b) as a function of SEI, for the four different flow rates and a distance between the electrodes of 7 and 14 cm (dashed lines/open symbols, and solid lines/closed symbols, respectively). Error bars are indicated but are sometimes too small to be visible.

Interestingly, the EC as a function of SEI strongly depends on the gas flow rate, showing an additional decreasing relationship at higher flow rates. Indeed, the SEI is defined by power and flow rate. The power rises a bit with flow rate, but not proportionally. Hence, the SEI clearly drops with rising flow rate. The NO_x concentration also drops with rising flow rate (Figure 5.8), but less strongly than the drop in SEI. As the EC is determined by both NO_x concentration and SEI, we obtained the lowest EC at the highest flow rate, i.e., 2.8 MJ/mol, for an SEI of 2.1 kJ/l (Figure 5.9 a). However, this condition corresponds to a NO_x concentration of only 1.72% (Figure 5.9 b). On the other hand, the highest NO_x concentration of 3.51% (obtained at 5 ln/min, 14 cm and highest SEI of 7.6 kJ/l; Figure 5.9 b) yields an EC of 4.8 MJ/mol (Figure 5.9 a).

Because of the relationship between power, flow rate and NO_x concentration, we achieved multiple points with similar SEI but clearly different EC (c.f., Figure 5.9a). This effect was also observed by Pei et al., who also investigated the EC and NO_x concentration as a function of distance between the electrodes for a DC glow discharge [148]. This relationship shows that the distance between electrodes provides an additional degree of freedom.

It should be realized that all these values are obtained for NO_x production simply from air (N_2:O_2 = 80:20). Care should be taken when comparing the results with literature (c.f., Figure 5.1 in section 5.1), where the best results are typically reported for oxygen-enriched air (usually N_2:O_2 = 50:50) (e.g., [59,143,151]). However, we want to design an industrial process, where starting from air is more convenient, and otherwise the cost of producing oxygen-enriched air should also be accounted for, which is never done in literature.

5.4.2 Large reactor in pin-to-pin configuration

For the large reactor in the pin-to-pin configuration, the plasma could be sustained in the current range of 400 - 1000 mA when the swirling flow was applied. Without swirling flow, the plasma was highly unstable, and we could only operate at higher currents. Hence, we discuss here only the results with swirling flow, and we refer to section 5.4.3, Figure 5.13) for the results without swirling flow.

The power as a function of current for different flow rates and distances between the electrodes in the large reactor in pin-to-pin configuration are presented in Figure 5.10.

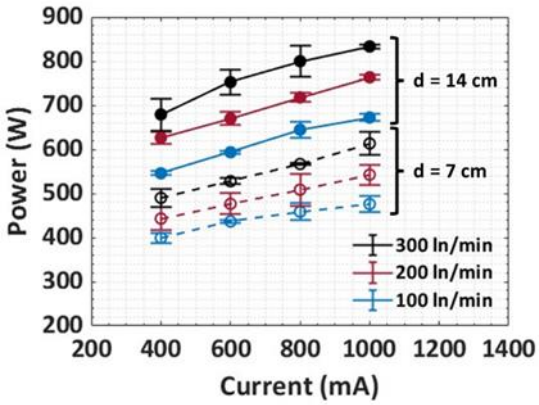

Figure 5.10. Plasma power as a function of current, for three different flow rates and two distances between the electrodes (dashed lines/open symbols and solid lines/closed symbols, for d = 7 and 14 cm, respectively), in the large reactor in pin-to-pin configuration. Error bars are indicated but are sometimes too small to be visible.

Similar to the observations in the small reactor, we can see a linear increase in power as function of current for all investigated conditions. Again, the deposited power increases with flow rate and with interelectrode distance. Increasing the distance between electrodes by a factor two yields a rise in power by much less than a factor two for the same current and flow rate. For example, for 1000 mA and 300 ln/min, the ratio in power between 14 and 7 cm is 1.35. This is far less than what we observed in the smaller reactor, where the power almost doubled.

The NO_x concentration as a function of current, for different flow rates and for a distance between the electrodes of 7 and 14 cm, is presented in Figure 5.11. We again see that the NO_x concentration decreases with flow rate and increases with current and distance between electrodes. There is a nearly linear increase as a function of current, although with a relatively shallow slope. As the rise in NO_x concentration as a function of current is very similar for all flow rates, the drop in NO_x concentration as a function of flow rate is nearly constant across the entire current range.

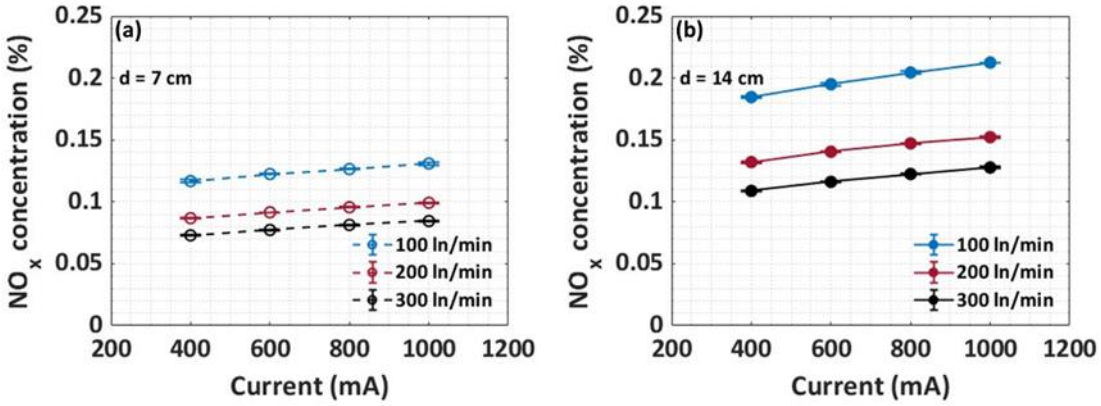

Figure 5.11. NO_x concentration as a function of current, for three different flow rates and a distance between the electrodes of (a) 7 cm, and (b) 14 cm, in the large reactor in pin-to-pin configuration. Error bars are indicated but are too small to be visible.

The highest NO_x concentration obtained is 0.21%, for a distance between the electrodes of 14 cm, a current of 1000 mA and a flow rate of 100 ln/min. Because of the significant reduction in SEI range, as compared to the small reactor, the NO_x concentration is significantly lower for all investigated conditions compared to the small reactor, where values up to 3.51% were obtained (Figure 5.8 b). We can see that the relative NO_x increase, upon rising distance between the electrodes, is again higher than the increase in power, e.g., it is 1.51 for 1000 mA and 300 ln/min, while the relative rise in power was only 1.35 (Figure 5.10). Still, the relative increase is smaller than twice. However, as the rise in NO_x concentration is larger than the rise in power, the EC will drop upon increasing distance between the electrodes. The EC and NO_x concentration as a function of SEI for different flow rates and distances between the electrodes are presented in Figure 5.12.

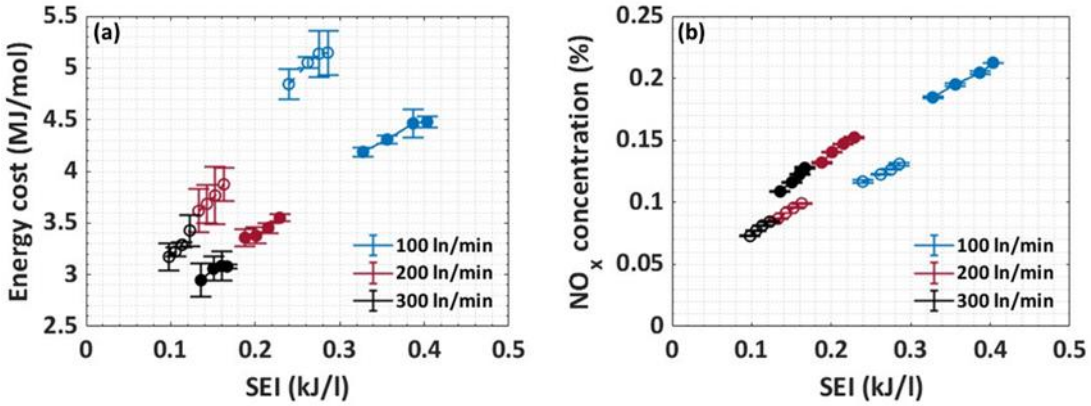

Figure 5.12. EC (a) and NO_x concentration (b) as a function of SEI, for three different flow rates and two distances between the electrodes (dashed lines/open symbols, and solid lines/closed symbols, for d = 7 and 14 cm, respectively), in the large reactor in pin-to-pin configuration. Error bars are indicated but are sometimes too small to be visible.

In contrast to the small reactor, here the EC increases, instead of decreases with SEI. The reason will be explained by our modeling insights in section 5.4.6 below. Again, for the same SEI, we observe a lower EC at 14 cm distance between the electrodes, because the NO_x concentration rises faster with interelectrode distance than the power (c.f., same behavior for the small reactor in Figure 5.9 a). The EC reaches its lowest value at an SEI of 0.13 kJ/l, for 300 ln/min and 400 mA, and is equal to 2.9 MJ/mol. It corresponds however to a low NO_x concentration of only 0.11%. The NO_x concentration increases nearly linearly as a function of SEI, and again, for the same SEI condition we reach a much higher NO_x concentration at larger distance between the electrodes. As mentioned above, the highest NO_x concentration obtained is 0.21%, at 14 cm distance, 100 ln/min and SEI of 0.4 kJ/l, but it corresponds to a fairly high EC of 4.5 MJ/mol. Based on these results, it is clear that even if we reduce the SEI significantly, the EC will not improve, because the NO_x concentration will also drop (c.f., Figure 5.12 b).

We believe that the relationship between NO_x concentration and SEI inside the plasma is the driving force for reducing the EC, rather than the overall SEI. However, in the formulas, the overall SEI is always used. The SEI in the plasma is (considerably) higher than the overall SEI, which is attributed to the limited flow going through the plasma, due to the plasma confinement, i.e., the plasma does not fill the entire reactor. This is most obvious in the large reactor. Note that the SEI inside the plasma is not a macroscopic parameter, although it is the intrinsic parameter affecting the performance. A clarification of this process is given in the next section.

5.4.3 EC and NO_x concentration in the large reactor without swirling flow

The EC and NO_x concentration in the large reactor in pin-to-pin configuration without swirling flow are plotted as a function of SEI in Figure 5.13, for three different flow rates and two distances between the electrodes. The highest NO_x concentration is 0.25%, obtained at the highest SEI, and

corresponds to an EC of 4.8 MJ/mol. A lower EC of 3.3 MJ/mol was obtained at a lower SEI of 0.26 kJ/l, but the corresponding NO_x concentration here is only 0.19%. While the NO_x concentrations are slightly higher than in the same reactor with swirling flow (where a maximum value of 0.21% is obtained, see Figure 5.11 b and Figure 5.12 b in chapter 5, section 5.4.2), the EC is somewhat worse (i.e., the lowest EC obtained in the reactor with swirling flow was 2.9 MJ/mol; Figure 5.12 a in section 5.4.2). This indicates that the swirling flow helps to not only improve the plasma stability, but also the reactor performance in terms of EC.

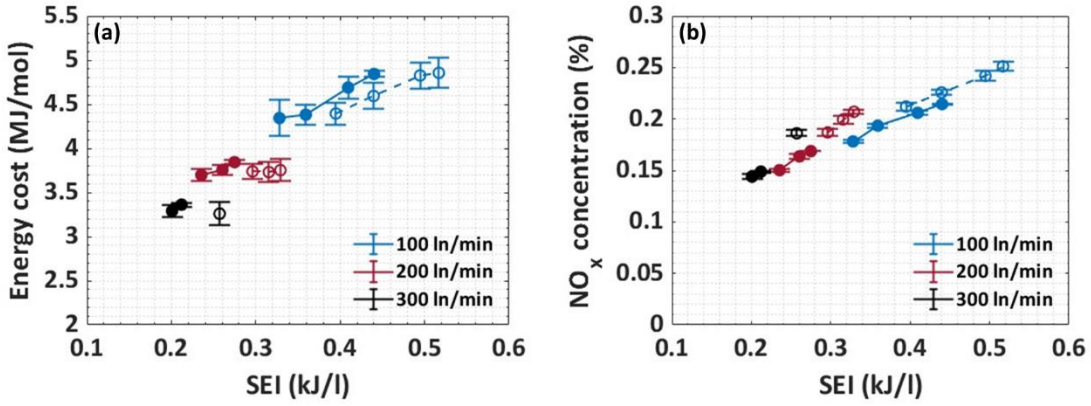

Figure 5.13. EC (a) and NO_x concentration (b) in the large reactor in pin-to-pin configuration without swirling flow, as a function of SEI, for three different flow rates and two distances between the electrodes (dashed lines/open symbols, and solid lines/closed symbols, for d = 7 and 14 cm, respectively). Error bars are indicated, but are often too small to be visible.

5.4.4 Large reactor in torch configuration

From previous section it is clear that the large reactor in pin-to-pin configuration is not very successful, due to the contracted nature of the plasma arc, limiting the amount of gas flowing through the plasma. This will be discussed in more detail below. To solve this limitation, we also tested the large reactor in torch configuration with the same swirling flow pattern. In the torch configuration, the bottom electrode of the reactor was removed, and the plasma was free to glide and rotate within the reactor, thus occupying a somewhat larger volume in the reactor (longer plasma column). For the torch configuration, the plasma was also stable in the current range of 400 to 1000 mA. The power and NO_x concentration as a function of current for three different flow rates are presented in Figure 5.14.

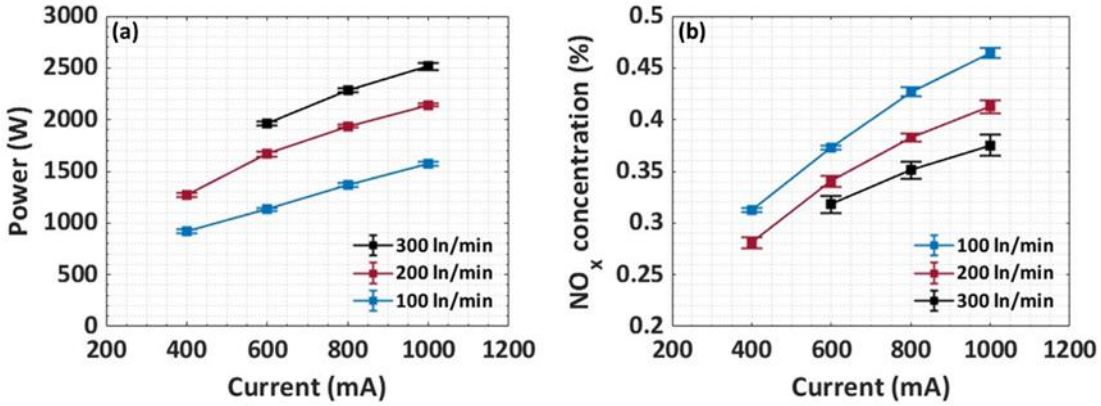

Figure 5.14. Power (a) and NOx concentration (b) as a function of current, for three different flow rates in the large reactor in torch configuration. Error bars are indicated but are mostly too small to be visible.

We can again see a nearly linear relationship between the current and power (Figure 5.14 a). The power again increases with flow rate, reaching the highest value achieved in this study, i.e., 2500 W for 300 ln/min and 1000 mA. Indeed, because the plasma can freely glide and rotate within the reactor body, the plasma column is longer and a higher voltage drop can be achieved, which results in a higher power deposited in the reactor. As a result, there is also a significant increase in the NO_x concentration compared to the pin-to-pin configuration (Figure 5.14 b). The NO_x concentration also shows a nearly linear dependence as a function of current. The highest NO_x concentration measured in this configuration was for 100 ln/min and 1000 mA and is equal to 0.46%. The NO_x concentration again decreases with rising flow rate but does not drop below 0.28%. Because higher power is deposited in this configuration, the SEI is also higher.

The EC and NO_x concentration as a function of SEI are presented in Figure 5.15. Similar to the pin-to-pin configuration, the EC increases with SEI. The lowest EC is achieved at 0.4 kJ/l, reaching 2.9 MJ/mol, corresponding to a NO_x concentration of 0.32%. The EC that corresponds with the highest NO_x concentration (of 0.46%) is 4.8 MJ/mol. Compared to the large reactor in pin-to-pin configuration, the EC is the same, but the NO_x concentration is more than double (e.g., highest NO_x concentration of 0.46% vs. 0.21% in torch vs. pin-to-pin configuration). Hence, overall, the torch configuration yields a better performance, due to the longer plasma column. Compared with the small reactor, the EC is slightly higher (2.9 vs. 2.8 MJ/mol), but the NO_x concentration is still dramatically lower (maximum 0.45% vs. 3.5%). This shows how reactor upscaling is quite challenging, and that reactor design is crucial for achieving a scaled-up process with high NO_x concentrations and low EC.

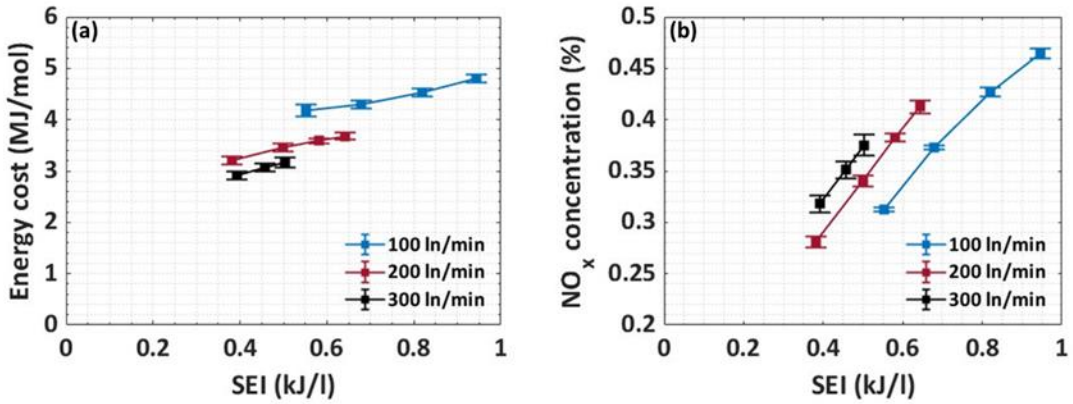

Figure 5.15. EC (a) and NOx concentration (b) as function of SEI, for the large reactor in torch configuration. Error bars are indicated but are mostly too small to be visible.

5.4.5 Comparison of production rate in the three reactors

In reactor upscaling, the production rate (PR) becomes a very important parameter, indicating whether reducing the SEI by increasing the gas flow rate through the reactor has a substantial effect, or only dilutes the products produced by the plasma. To determine whether the scaling up is successful, we evaluated how the PR changes as a function of SEI, for the conditions of lowest EC, for the three reactors, i.e., the small pin-to-pin, large pin-to-pin and large reactor in torch configuration; see Figure 5.16.

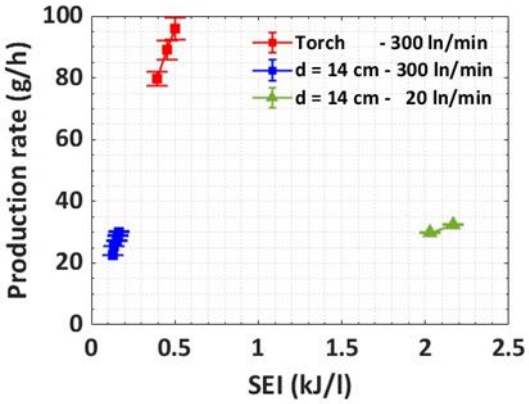

Figure 5.16. Total NO_x production rate as a function of SEI, for the three different reactors, i.e., small pin-to-pin, large pin-to-pin, and the large reactor in torch configuration. The conditions with the lowest EC are presented here.

It is logical that the PR increases with increasing SEI. The PR trends closely follow the trends in NO_x concentration. When comparing both reactors in pin-to-pin configuration, we see that they yield more or less the same PR (in the range of 20 – 35 g/h). Indeed, the large reactor operates at 15 times higher flow rate, but the obtained NO_x concentration is about 15 times lower

(maximum 3.51% vs. 0.21% in the small vs. large reactor). Both effects compensate each other when determining the PR. The corresponding EC in the large reactor is however slightly lower (4.5 vs. 4.9 MJ/mol in the large vs. small reactor), due to the much lower SEI (linked to the much higher flow rates).

These results are very important, as they indicate that the mass flow heated to the temperature leading to NF (or in other words, the amount of gas flowing through the plasma arc) is nearly the same for the large and small reactor, despite the substantially higher flow rate passing through the large reactor. This suggests that the plasma arc in the large reactor is very contracted and is probably not wider than the plasma arc in the small reactor, despite the much larger reactor dimensions. Hence, this limits the amount of gas flowing through the plasma.

In general, we can conclude that the large reactor in pin-to-pin configuration is not very successful for upscaling, at least in this configuration, because the PR is not enhanced. The reason is the low NO_x concentration obtained, due to the higher flow rates, which dilute the NO_x produced in the plasma, while the amount of NO_x produced in the plasma, determined by the flow passing through the plasma arc, is the same for the small and large reactor, due to the similar plasma arc diameter, as explained above.

The question arises whether this limitation could be mitigated if the PSU of the large reactor could deliver much higher power, leading to much lower SEI. The answer is no, because, even if the PSU would deliver much higher power, the arc diameter would not rise with the same extent, so there would still be gas not flowing through the arc, causing dilution of the produced NO_x.

In summary, our results indicate that the NO_x production inside the plasma is very similar for the small and the large reactor, but due to the additional (much higher) flow rate in the large reactor, which is not passing through the plasma (and thus not giving rise to NO_x production), the overall NO_x production in the large reactor is lower. This effect will be discussed in more detail in section 5.4.6, by means of thermodynamic equilibrium calculations. Nevertheless, despite the lower NO_x concentration in the large reactor, the EC is very similar as in the small reactor, due to the lower SEI.

From comparing the NO_x concentrations in the small and large reactor in pin-to-pin configuration, it is clear that we need other modifications to the reactor design, in order to increase the performance, and to overcome the fundamental limitation of the limited amount of gas passing through the arc in case of upscaling, causing dilution.

Figure 5.16 illustrates that this limitation can be overcome by operating the large reactor in torch configuration. Indeed, our results show more than three times higher PR, while sustaining the EC below 3 MJ/mol. The highest PR that we achieved is 96 g/h, for an SEI of 0.5 kJ/l, while at 0.4 kJ/l (corresponding to the lowest EC of 2.9 MJ/mol), the PR is 80 g/h. The reason for these good results is that in the torch configuration, the NO_x concentration is much higher than in the pin-to-

pin configuration, for nearly the same EC. Hence, this shows again that if we pay sufficient attention to the reactor design, scaling up can be successful.

An important aspect in terms of upscaling is the question of long-term operation of plasma reactors. In general, erosion of the electrodes, and of the reactor, is one of the limitations for long-term operation. This is one of the reasons why so-called 3D GA plasma reactors were introduced as an alternative to classical 2D GA reactors [54]. In the design of our large reactor, the main components, including the electrodes and the main reactor body, are made from temperature- and corrosion-resistant materials. This greatly increases the reactor lifetime, thereby enabling long-term process operation.

As mentioned in the Introduction, except for the Birkeland-Eyde (BE) process, to our knowledge, all other reported NF plasma processes were operated in lab scale reactors. Hence, the question arises how our upscaled reactor differs from the BE process. In the BE process, magnetic fields had to be used to stabilize the plasma, while we are using a swirling flow to achieve the same effect. In this way, we avoid the costly operation of large electromagnets, and at the same time we are able to reach the very low EC necessary for the industrial implementation of this technology. The BE process further utilized high current alternating current (AC) arcs, which created an asymmetric heating profile within the gas flow. In our reactors the gas is heated more uniformly through DC current, which allows for better control of the gas flow dynamics [162,163].

5.4.6 LTE calculations

Previous research conducted by Naidis et al. has shown that arcs sustained by currents larger than 200 mA are in LTE [153]. This would indicate that we can use LTE calculations to gain insights into the process. The calculated NO concentration and corresponding EC for producing this NO, from air, as a function of temperature, assuming LTE, are presented in Figure 5.17.

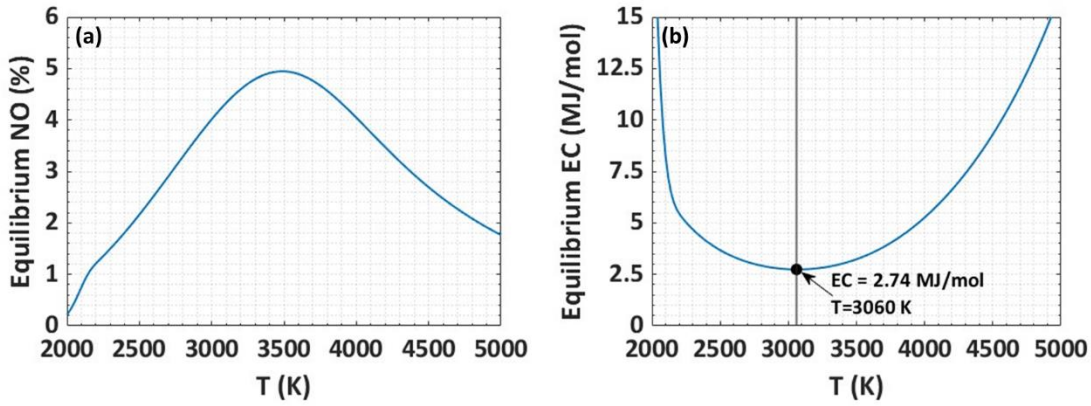

Figure 5.17. Calculated NO concentration (a) and EC (b) as a function of temperature, assuming LTE.

We can see that in the lower temperature region (< 3500 K), there is a steep increase in NO concentration as a function of temperature, which reaches a maximum of 5 % at 3500 K. The maximum is followed by a clear drop at higher temperatures, reaching below 1 % above 6000 K (see Figure 5.17 a). This indicates that for relatively small changes in temperature, a large increase in NO concentration will be observed in the temperature range of 1900 – 3200 K. The lowest EC calculated is 2.74 MJ/mol, for a temperature of 3060 K. Note that this value is very close to the lowest EC of 2.8 MJ/mol that we obtained experimentally in the small reactor for 20 ln/min and an SEI of 2.1 kJ/l (Figure 5.9 a). Also in the large reactor, we achieved similar values (i.e., 2.9 MJ/mol, again close to the thermodynamic limit) in the pin-to-pin and torch configuration for 300 ln/min and SEI values of 0.13 (Figure 5.12 a) and 0.4 kJ/l (Figure 5.15), respectively. The EC decreases gradually in the temperature range of 2000 – 3000 K, leading to this minimum value, after which it starts rising (Figure 5.17 b). These calculations present the thermodynamic limit of the EC, together with the maximum concentration of NO that can be obtained for this EC, being 4.2 % (see Figure 5.17 a). We will now use this information to obtain more insights in our experimental results. Indeed, following equation (5.6) and using the experimental plasma power and mass flow rate, we can now calculate the average gas temperature in the reactor.

5.4.7 Calculated gas temperature in the reactors

The average gas temperature, calculated as explained in previous section, is plotted in Figure 5.18 as a function of current for different flow rates, for the high SEI region and low SEI region, corresponding to the small (a) and large (b) reactor, respectively.

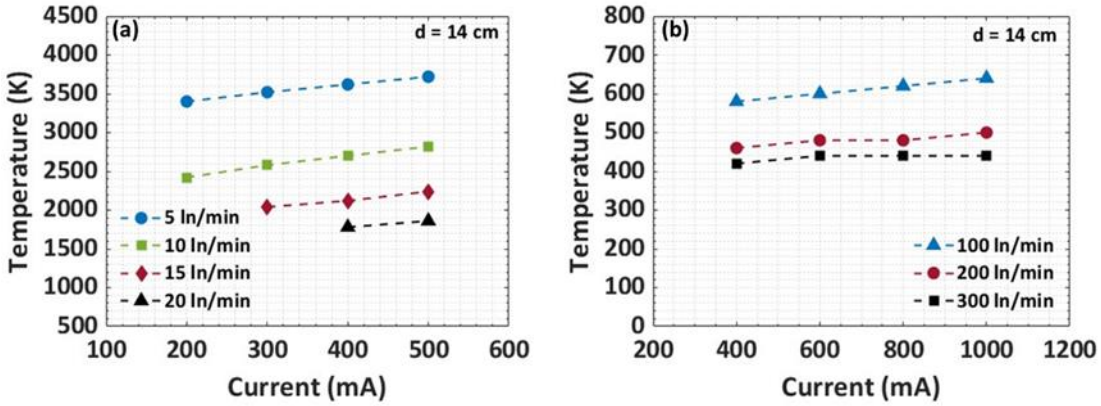

Figure 5.18. Average gas temperature, calculated from the measured power and flow rate, using eq. 6, in the small reactor (a) and large reactor (b).

In the small reactor (Figure 5.18 a), the average temperature increases linearly with current, although the slope is shallow, reaching its highest value of 3720 K for 500 mA and 5 ln/min. The gas temperature drops as a function of the gas flow rate, reaching values below 2000 K for 20 ln/min. Based on these calculations for the small reactor, we should be able to achieve very efficient NO_x production at 200 mA and 5 ln/min, or at 500 mA and 10 ln/min. In reality, we observe much lower NO_x concentration compared to the equilibrium calculations, i.e., maximum 3.5%. We attribute this observed discrepancy due to back-reactions taking place in the afterglow of the plasma, i.e., the recombination of NO with O or N atoms, back into O_2 or N_2 molecules (see reverse reactions 3 and 4 from Table 5.1) [151]. As a result, we measure lower NO_x values than theoretically predicted based on thermodynamic equilibrium. Furthermore, we can see that for the higher flow rate, the average gas temperature presented in Figure 5.18 a will yield far less NO, according to the thermodynamic equilibrium calculations (c.f., Figure 5.17 a), than what we measure in our small reactor, indicating that we are producing more than the equilibrium, especially for the case with the lowest EC of 2.8 MJ/mol where the NO_x concentration was 1.8%.

Even more interesting is that in the large reactor (Figure 5.18 b), the temperatures are consistently below 700 K, which creates conditions impossible for NO_x production, simply based on thermodynamic equilibrium. Hence, the temperatures plotted in Figure 5.18 b are unrealistically low for this reactor, at least for the plasma core. More realistic temperatures will be presented below. The reason for the observed discrepancies in the large reactor, and also for the high flow rates of the small reactor, lies in the contracted nature of the plasma, for which the above method of calculating the average gas temperature (based on experimental plasma power and gas flow rate) breaks down. Atmospheric pressure plasmas indeed experience a contracted power density profile, due to the non-linear relation between gas heating and the electric field [152]. In order to calculate the SEI and the average temperature, we assumed that the power is deposited uniformly in the reactor volume and the entire flow passes through the chemically active plasma region. Obviously, this gives rise to such unrealistically low plasma temperatures. Indeed,

experimentally, the measured plasma power is deposited in a very small volume and only a fraction of the gas flow is heated to the (much higher) temperatures responsible for NO_x production.

As a result, we usually observe an inverse relationship between EC and NO_x concentration, meaning that they both rise as a function of SEI (see Figure 5.12 and Figure 5.15 above). This is sign that at high SEI (and thus higher NO_x concentrations), the back-reactions become dominant, and the EC increases considerably. When the (macroscopic) SEI is lower, and because the plasma arc is not filling the entire reactor width, the cold gas surrounding the plasma quickly mixes with the exhaust, stopping the back-reactions and diluting the products, resulting in a more efficient process, but at the price of lower NO_x concentrations. In this situation, the SEI inside the plasma is high, given that a very small amount of the mass flow is in a plasma state and all the power is deposited in this very small volume, while on the other hand, the macroscopic SEI (of the total reactor) is low, because of the large averaging.

5.4.8 Improved thermodynamic equilibrium calculations

In order to account for the above effect, we modified the equilibrium calculation of the gas temperature by making two strong assumptions: (i) The plasma is thermally insulated, and non-equilibrium effects are negligible, and (ii) the cold gas surrounding the plasma stops the back-reactions through mixing, and all the products generated in the hot region are recovered. Following these assumptions, we can correlate the experimentally measured EC with the theoretically calculated EC, and this allows us to correctly determine the temperature inside the plasma. Using equation (5.6) and the experimental plasma power, we can then determine the gas flow passing through the hot region, for the temperature determined by the EC.

Based on Figure 5.17 b, we can see that for the same EC we can have two different temperatures inside the plasma. In order to determine which solution is physical, we employ two boundary conditions: (i) The flow rate passing through the hot region should not exceed the total flow rate of the experiment, and (ii) the plasma temperature and NO_x concentration as a function of current and flow rate must agree with the experimental observations. The plasma temperature and the flow rate passing through the region with elevated temperature, obtained according to these calculations, are plotted in Figure 5.19 as a function of current, for different flow rates, for 14 cm distance between both electrodes.

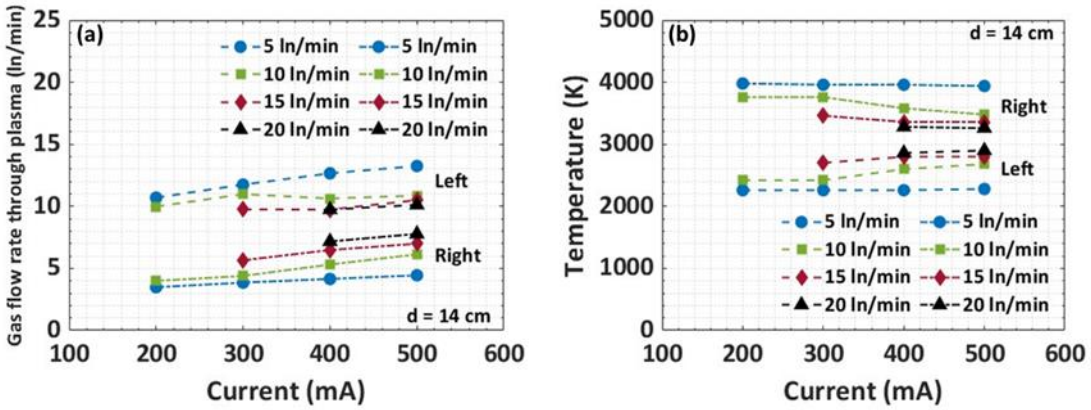

Figure 5.19. Calculated flow rate passing through the region with elevated temperature (a), and corresponding plasma temperatures (b), in the small reactor, as a function of current for four different flow rates, for 14 cm distance between both electrodes. "Left" and "right" in the figure denote whether the values of temperature are taken from the left-hand side or right-hand side of the EC graph (Figure 5.17 b); see text.

Our calculations show that if we take the values of the temperature from the right-hand side of the EC graph (Figure 5.17 b), as presented by the dash-dotted curves in Figure 5.19, all flow rates calculated in this way are below the total flow rate. If we take the values from the left-hand side of the graph, the calculations for 5 and 10 ln/min provide unphysical results, being higher than the total flow rate, while the calculations for 15 and 20 ln/min predict flow rates below the total flow rate, hence they are physical (Figure 5.19 a). Only looking at the flow rate, we cannot determine which conditions are physical, and we need to look at the temperatures and NO_x concentration as well.

We can see from Figure 5.19 b that if we take the values of the EC from the right-hand side of the plot in Figure 5.17 b, the temperature slightly decreases as a function of current (mainly at 10 ln/min), while for the values at the left-hand side, the temperature slightly increases as a function of current (again mainly at 10 ln/min; see Figure 5.19 b). From our experiments we know that the EC in the small reactor decreases with increasing SEI (Figure 5.9 a), which means that the temperature and the NO_x concentration have to increase with current. The latter also corresponds to our expectations and the general understanding of arc plasmas. This means that we are on the left-hand side of the EC graph.

Taking these effects into account, we can see that only the flow rates of 15 and 20 ln/min satisfy these conditions. As seen from Figure 5.7, the plasma is less contracted at low gas flow rate, where we can consider that the power is deposited within the whole reactor and the back-reactions are limiting the conversion, while at the higher gas flow rates, when the plasma is contracted, our approximations become more valid, i.e., (i) the plasma is thermally insulated, and (ii) the cold gas surrounding the plasma stops the back-reactions through mixing, and all products generated in the hot region are recovered (see discussion above). Our model shows that,

provided the above assumptions are valid, a value of the EC near the thermodynamic limit can be reached, but at the expense of dilution of the produced NO_x; in other words, at a lower NO_x concentration than predicted by the model.

5.4.9 Application of the same method to the large reactor

Based on the above assumptions, we can now also roughly describe the behavior of the large pin-to-pin reactor. Indeed, in this situation the plasma is always contracted, and the NO_x concentration is also increasing with current.

Following our previous considerations, the plasma temperature must be taken from the left-hand side of the EC graph (Figure 5.17 b). Figure 5.20 presents the calculated plasma temperature and flow rate passing through the region with elevated temperature for the large pin-to-pin reactor with 14 cm distance between both electrodes, as a function of current for three different flow rates.

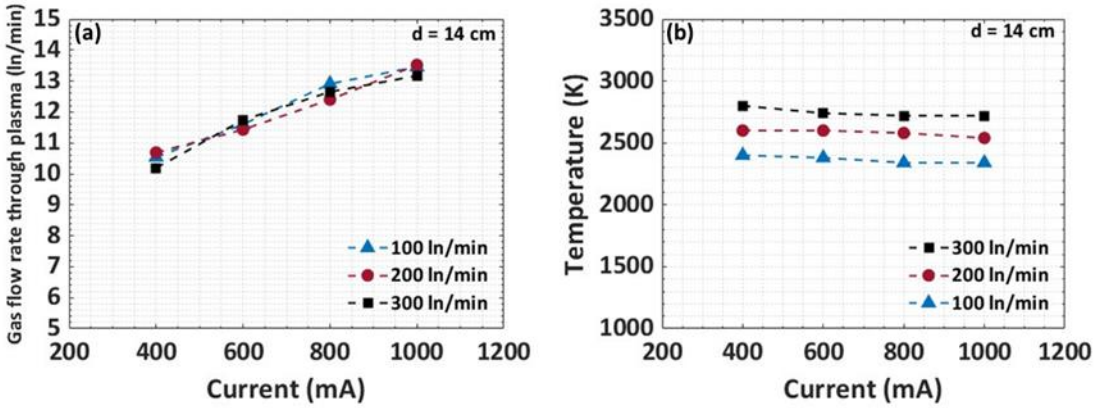

Figure 5.20. Calculated flow rate passing through the region with elevated temperature (a) and corresponding plasma temperature (b), in the large pin-to-pin reactor with 14 cm distance between both electrodes, as a function of current, for different flow rates.

We can see that the flow rate through the region with elevated temperature increases with current and is nearly the same as what we calculated for the smaller reactor (c.f., Figure 5.19 a and Figure 5.20 a) for 400 mA, despite the much larger reactor dimension, hence indicating indeed that the plasma is significantly contracted in the large reactor. Upon rising current, the radius of the plasma rises, which leads to a 4 ln/min increase in flow rate passing through the plasma for 1000 mA. Nevertheless, this flow rate of 14 ln/min is still dramatically lower than the experimental flow rates, due to the contract nature of the plasma. Note that the flow rate passing through the plasma is roughly the same for a total flow rate of 100, 200 and 300 ln/min.

The calculated temperature in the plasma is also very similar to the values determined in the small reactor (c.f., Figure 5.19 b (left) and Figure 5.20 b), increasing as a function of flow rate, but

in this case slightly decreasing as a function of current. This behavior highlights the limitation of our approach. In the large reactor (low SEI region), the measured EC increases as a function of SEI, together with the NO_x concentration (c.f., Figure 5.12). There are only two ways for the EC to increase as a function of SEI: (i) if we follow the left-hand side of the EC graph (Figure 5.17 b), the temperature has to drop with increasing NO_x concentration, or (ii) if we follow the right-hand side of that graph, the temperature has to increase, and the NO_x concentration should drop. In our experiments, we observe an increase in both EC and NO_x concentration as a function of SEI. Following Figure 5.17 a, this would mean that the back-reactions are dominating and are limiting the conversion. Hence, one of our main assumptions breaks down and we observe a decreasing temperature as a function of current. This indicates that the design of the large pin-to-pin reactor must be improved in order to reach higher NO_x concentrations for low EC, due to the limitations of the back-reactions. Indeed, if the model breaks down, it means that the reactor does not operate efficiently.

Increasing the SEI in the large reactor (by applying a higher power) will only yield better performance if the plasma column would also become broader; otherwise, there is still a lot of gas not passing through the plasma and diluting the produced NO_x. However, a higher plasma power will not necessarily lead to a wider plasma column, due to the natural phenomenon of contraction at high power plasmas. We plan to test this in our future work. Despite this, we can see from Figure 5.20 b that the drop in temperature as a function of current is not very large, so we believe that the information extracted is still valuable for comparing the results between the different reactors, especially for the low EC conditions, where our approximations should be more valid.

The same evaluation is also made for the large reactor in torch configuration. The flow rate passing through the region with elevated temperature and the plasma temperature as a function of current for three different flow rates in the torch configurations are presented in Figure 5.21.

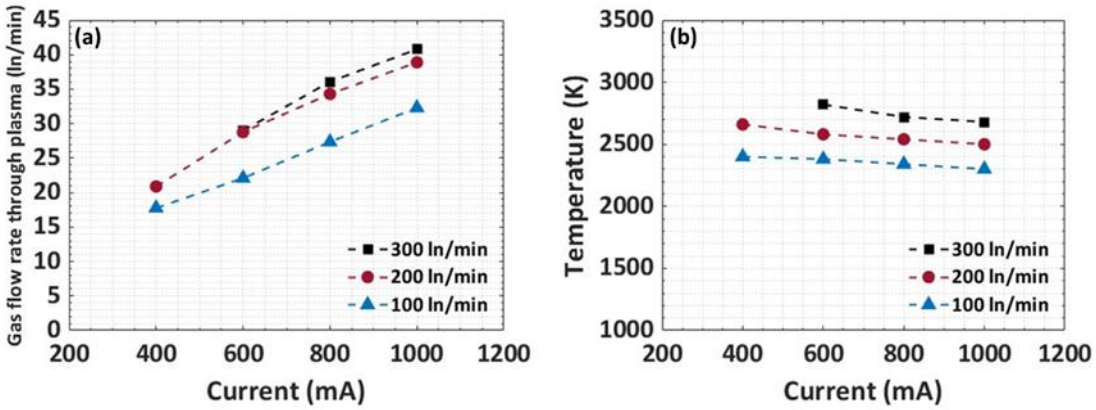

Figure 5.21. Calculated flow rate passing through the region with elevated temperature (a) and corresponding plasma temperature (b), as a function of current, for different flow rates for the torch configuration.

The torch configuration clearly provides better performance than the pin-to-pin reactor. The flow rate passing through the plasma is significantly higher, reaching nearly 30 ln/min for 100 ln/min total flow rate, and 40 ln/min for 300 ln/min total flow rate, both at the highest current, while the plasma temperature slightly drops as a function of current. This indicates that this torch design is suitable for upscaling, provided that the temperature after the plasma can drop sufficiently fast to avoid back-reactions (recombination of NO with O or N atoms). As mentioned before, removing the bottom electrode allows the arc to freely glide and rotate within the reactor, leading to a larger fraction of the gas heated to the desirable temperature. Despite this, the plasma is still relatively contracted, and thus, still a very small fraction of the gas is heated compared to the increase in flow rate that we have provided (i.e., only 30 – 40 ln/min, for a total flow rate of 100 – 300 ln/min; c.f., Figure 5.21 a). These results clearly indicate that the limited NO_x concentration in the large reactor is not caused by the chemistry, but by the fluid dynamics and plasma phenomena influencing the process.

The exact mechanisms of how the mixing process results in quenching of the back-reactions is a complicated computational fluid dynamics problem. However, similar observations were made by D'Isa et al., in a CO_2 microwave plasma in the low SEI region, where the thermodynamic limit was also reached [164]. We note that Birkland also reached to similar conclusions related to the plasma dynamics and the process of plasma-based NF. In order to operate their reactor efficiently, only ¼ of the gas had to pass through the plasma and the remaining ¾ acted as quenching gas. As a result, their NO concentration was lower but produced quite efficiently [162,165], just like in our upscaled reactor.

In general, our study shows that plasma reactors can be very efficiently scaled up, provided that the concentration of products is lower than the maximum based on thermodynamic equilibrium. Indeed, our model assumes that mixing of the unreacted gas with the produced NO_x stops the

back-reactions. We see that our model breaks down at the conditions of the large reactor, which indicates that back-reactions become too important. This is attributed to poor mixing between the gas surrounding the plasma and the hot gas inside the plasma, because there is so much gas surrounding the plasma in the large reactor, which is not in close contact with the hot plasma core.

5.4.10 Summary of the insights from the thermodynamic equilibrium calculations

Our thermodynamic equilibrium calculations show that we have almost reached the thermodynamic limit of the EC (estimated as 2.74 MJ/mol for NO_x production from air) in the small reactor, as well as in the large reactor, both in pin-to-pin and torch configuration. However, the contracted nature of the plasma leads to measured NO_x concentrations that are much lower than those predicted by the thermodynamic equilibrium calculations, due to dilution with non-reacted gas. Despite this, the fact that we are reaching EC values near the calculated thermodynamic minimum indicates that the same process responsible for the low concentrations (i.e., dilution with non-reacted gas) is also responsible for the low EC, because this dilution stops possible back-reactions. These insights can help us to design better upscaled reactors, overcoming these limitations. Finally, based on these thermodynamic calculations, we propose a method to estimate the plasma temperature and flow rate passing through the plasma. Our model illustrates that the flow rate passing through the plasma in the torch configuration is already significantly higher than in the pin-to-pin reactor, explaining the higher NO_x concentrations achieved in our experiments. We believe this can provide a strategy for energy-efficient upscaling of plasma-based NO_x production, as well as other plasma-based gas conversion applications.

5.5 Conclusions

In this chapter, the challenge of reactor engineering to design an efficient scaled-up plasma reactor for industrialization of plasma-based NF, was introduced as one of the main obstacles toward industrialization of plasma-based gas conversion processes. Hence, we tried to tackle this challenge by developing a low current, high flow rate plasma reactor, and we compared the results with its smaller counterpart, operating according to the same principle (pin-to-pin reactor, powered by DC current, operating in the arc regime), but at lower flow rates. This allowed us to scan a large range of SEI values and investigate the potential of reactor upscaling.

Experimentally, we studied the plasma-based NO_x production as a function of current and flow rate, ranging from 200 to 1000 mA and from 5 to 300 ln/min, respectively, for a small pin-to-pin reactor, a large pin-to-pin reactor, as well as the same reactor but in torch configuration, to overcome the limitations in upscaling of the pin-to-pin reactor. Varying the current and flow rate, together with operating the reactor at different configurations, indeed allowed us to study the plasma-based NO_x production in a wide range of SEI, i.e., between 0.1 and 7.6 kJ/l.

We showed that the EC and NO_x concentration depend on SEI, but also on the flow rate in conjunction with the interelectrode distance. The lowest EC achieved in our study was 2.8 MJ/mol, for an NO_x concentration of 1.72% at a flow rate of 20 ln/min and distance between the electrodes of 14 cm, for the small reactor. The highest NO_x concentration obtained in this reactor is 3.51% but corresponding to an EC of 4.8 MJ/mol. Note that these results were obtained for NO_x production simply from air, and that in oxygen-enriched air, the results are typically better. Care should be taken when comparing the results with literature (c.f., Figure 5.1 in section 5.1), where the best results are typically reported for oxygen-enriched air. However, we want to design an industrial process, where starting from air is more convenient, and otherwise the cost of producing oxygen-enriched air should also be accounted for, which is never done in literature.

In the large reactor with the same design (pin-to-pin), the NO_x concentration drops dramatically to 0.21%, for an EC of 4.5 MJ/mol, due to the much higher flow rate. The lowest EC in this configuration is 2.9 MJ/mol, for a NO_x concentration of only 0.11%. Due to this lower NO_x concentration, the PR is very similar as in the small reactor, despite the much higher flow rate. The reason for this is the contracted nature of the plasma, which results in producing low NO_x concentrations due to dilution of the produced NO_x with unreacted gas that has not passed through the plasma, but it improves the EC due to quenching of the back-reactions.

On the other hand, when changing the large reactor to a torch configuration, the NO_x concentrations are more than double the values obtained in the pin-to-pin reactor, for nearly the same EC. This illustrates the potential for upscaling this technology. Indeed, we achieved production rates of 80 g/h for an EC of 2.9 MJ/mol with this torch configuration, at a flow rate of 300 ln/min. This is ca. three times higher than the production rate in the small reactor. It demonstrates that the torch configuration is a better suited design for scale up, due to the somewhat larger plasma column, filling a larger fraction of the reactor volume, so that higher flow rates can pass through the plasma, as demonstrated by our calculations. Based on the study of Tsonev et al., increasing the pressure inside the reactor will substantially increase the NO_x concentration and should bring the process much closer to industrial applications [143].

Last but not least, we showed based on thermodynamic equilibrium calculations that we have nearly reached the thermodynamic minimum of the EC (i.e., 2.74 MJ/mol for NO_x production from air; note that it is lower for oxygen-enriched air). However, due to the contracted nature of the plasma, the measured NO_x concentrations are significantly lower than those predicted by the thermodynamic equilibrium calculations, due to the dilution with non-reacted gas, as mentioned above. In reality, the process is strongly dependent on the SEI effectively delivered to the plasma, rather than the overall (macroscopic, measured) SEI delivered to the reactor, which leads to the false impression that a lower macroscopic SEI (at constant NO_x concentration) should lead to a lower EC. Indeed, this lower macroscopic SEI can correspond to a high SEI inside the plasma, due to the contract nature of the plasma. The presented thermodynamic calculations allow us to estimate the plasma temperature and flow rate passing through the plasma, based on the

measured products. It can explain the better performance of the torch configuration, due to the larger flow rates passing through the plasma. This provides a strategy for potential energy-efficient scale up of the technology.

6 Overall conclusion and outlook

Plasma technology is attracting growing interest for NF toward the production of fertilizers because it enables efficient gas heating and high-throughput NF, and, depending on the operating conditions, it also allows to activate nitrogen molecules by vibrational excitations and electron impact reactions (i.e., through non-equilibrium pathways), which leads to an efficient process for gas conversion applications [17,42]. As mentioned above, due to the advantages offered by plasma technology, it is a potential solution for on-site production of fertilizers using air and renewable electricity [6,17,43]. In addition, the interaction of plasma with an appropriate catalyst, known as "*plasma catalysis*", can further enhance the efficiency of the processes by reducing energy cost and the selective production of desired chemicals [17,43].

However, the industrial application of plasma technology for NF is still facing several challenges on its way towards becoming an industrial process, such as challenges of plasma and catalyst interaction for the selective production of desired chemicals, the high energy consumption of plasma-based NF processes, and challenges of design and development of scaled up and energy-efficient plasma reactors for industrial purposes [6].

In this thesis, using a combined experimental and computational approach, we have tried to address these challenges in plasma-based NF. Throughout different chapters, we describe three different reactors and case studies: (I) a radio-frequency – inductively coupled plasma (RF-ICP; a cold plasma suitable for plasma-catalyst interaction studies), (II) a rotating gliding arc (RGA), and (III) a pin-to-pin arc reactor (both small and scaled-up; the latter also in torch configuration) for NF toward NO_x production. Each time, using one of these reactors, we tried to tackle one of the challenges on the way toward industrialization of plasma-based NF, as mentioned above, and we tried to answer some essential research questions. By doing so, we contribute to the existing SOTA and we deepen the understanding of plasma technology, which can lead to its future wide implementation. The research questions are outlined below.

- **How can we better understand plasma-catalyst interactions, and study the impact of operational parameters on the process efficiency and mechanisms that are responsible for NO_x production?**

In chapter 2, we discussed ideal chemical reactors and their deviations from ideal conditions, highlighting that conventional CSTR and PFR models, due to their idealized assumptions, fail to accurately predict a real reactor performance. We introduced the dimensionless Pe number to quantify these deviations and aimed to present a catalytic model with (I) reasonable accuracy, (II) flexibility, and (III) computational efficiency. The axial dispersion model enhances predictions in real reactors with significant axial mixing, offering flexibility while maintaining computational efficiency. Therefore, we introduced a 1D heterogeneous catalysis model for packed bed reactors, outlining its development and listing common correlations for physical parameters. In chapter 3, we applied this model to study the post-plasma catalytic production of NO in an RF-ICP reactor, as investigated by Ma et al. [99]. Our model provided valuable insights into different reaction

mechanisms, their roles, and their impact on NO production. Additionally, it suggested strategies, such as designing a catalytic reactor resembling a PFR, to further enhance the reactor performance where higher NO can be produced with a lower EC.

We acknowledge that the reliability of these modelling predictions should always be verified with experimental data. Conducting experiments to accurately measure the concentrations of various species (i.e., N_2, O_2, N, O, and NO) in the system, both post-plasma and at the reactor outlet, is essential, as these measurements serve as the boundary conditions for the governing equations used for describing the reactor behavior. This can be achieved by using a combination of a quadrupole mass spectrometer for measuring N_2, O_2, and NO, along with laser-induced fluorescence spectroscopy for determining the concentrations of N and O atoms. Furthermore, optical emission spectroscopy (OES) can be employed to provide reasonably accurate measurements of the vibrational temperature of the gas entering the catalytic stage, thereby enabling a more precise calculation of the distribution of the vibrational states. Additionally,, using OES, the species that exist inside the plasma can be identified and their concentrations measured by analyzing the emission spectra. This way a more accurate idea of the chemistry happening inside the plasma is obtained, and therefore, the model can be benchmarked more accurately against the experiments, enhancing the reliability of the provided strategies for further improving reactor performance. Furthermore, information obtained by OES measurements enables us to investigate the changes in the plasma behavior at different reactor sizes by monitoring how the plasma properties vary upon increasing reactor size, which is crucial for prediction of the gas phase chemistry, heat transfer dynamics and plasma confinement in scaled-up reactors.

This modelling approach is not only useful for investigation of the studied system but can also be applied for other plasma types coupled with a catalyst. While we studied in this thesis post-plasma catalysis, in-plasma catalysis could also be studied with such a model. The primary objective of coupling plasma with a catalyst is the selective production of desired products. In the case of plasma-based NF, this is NO/NO_2, rather than e.g., the formation of O_3 or N_2O, a highly undesirable potent greenhouse gas. Therefore, in the future, our plan is to expand the surface chemistry by including surface reactions that may result in the production of byproducts, (e.g., N_2O), due to the interaction of plasma with the catalyst surface. Additionally, this more comprehensive surface kinetics will be integrated with a reduced (to avoid the computational cost) yet more intricate and accurate gas-phase chemistry occurring in the plasma, aiming to gain a broader understanding of the reaction mechanisms responsible for producing different products. The end goal will be, first, to experimentally validate the model predictions, and second, to investigate conditions under which the process selectivity leans toward NO and NO_2 production and how the system can be improved or optimized to achieve higher NO_x production with a lower EC. Furthermore, investigation of plasma-catalyst interaction by combining such a model with comparative studies of various catalysts for NF in different plasma reactors can be a very interesting topic for future research, as it can open new windows of opportunity for the

simulation, improvement, and optimization of plasma-catalytic processes operating in fixed bed reactors.

- **How can improving the reactor design help enhance the energy efficiency of plasma-based NF for NO_x production?**

As mentioned above, to be competitive with current industrial processes, the EC of plasma-based NF needs to reach to 1.1-1.5 MJ/(mol N). Various plasma types are explored in literature for plasma-based NF aimed at NO_x production, with warm plasmas like MW and GA showing promise for this application. However, the energy efficiency of these processes requires substantial improvement to attain industrial viability. The RGA plasma reactor, as used in the study of Jardali et al. [59], demonstrated the best performance to date of its publication, achieving NO_x concentrations up to 5.5% with an energy consumption of 2.5 MJ/mol in an oxygen-enriched air plasma. In chapter 4, by improving its design, we aimed to further improve the performance of this reactor. To this goal, we integrated the RGA reactor with a specifically designed nozzle, referred to as the "effusion nozzle". The so-called effusion nozzle was designed in a collaboration between myself and my colleague James Creel. I was also responsible for the design of the experiments and the experimental investigation of the process performance in a relatively wide range of applied power, gas flow rates and N_2 fractions in the feed gas. To gain further insights in the improved performance of combining the RGA plasma reactor with the effusion nozzle, my colleague Senne Van Alphen developed a modelling strategy including four complementary models, i.e., a turbulent gas flow model, a fully coupled heat transfer model, streamline integration and a quasi-1D plasma chemistry model. The full description of his modelling results are presented in our joint paper published in the Chemical Engineering Journal [151].

By investigating this novel reactor/nozzle design across various operating conditions and distinct plasma regimes, we achieved an approximate 8% increase in NO_x production and, more importantly, an approximately 23% reduction in EC compared to the reactor without an effusion nozzle. One key factor contributing to this performance improvement was the effusion nozzle's ability to facilitate plasma ignition and sustainment at lower power levels while maintaining similar or slightly higher NO_x concentrations. Furthermore, the modeling study conducted by my colleague Senne Van Alphen identified rapid cooling as gas molecules collided with the effusion nozzle, effectively inhibiting the backward reactions in the Zeldovich mechanism and leading to higher NO_x concentrations after the plasma.

It is important to highlight that after these studies, other plasma types were also experimentally investigated, demonstrating highly impressive outcomes. For instance, NO_x concentrations as high as 3.8% and an energy cost as low as of 2 MJ/mol in a MW plasma was reported in the study of Kelly and Bogaerts for higher power and flow rate, which resulted to the highest achieved NO_x production rate of 85.9 g/h [147]. Very recently, Tsonev et al. showed that increasing the pressure leads to a further improvement of the performance in an RGA reactor, with EC as low as 1.8

MJ/mol, NO_x concentration of 4.8%, and PR of 69 g/h, in oxygen-enriched air, at a pressure of 3 barg [143]. Nevertheless, our findings continue to remain among the top documented outcomes in the literature.

Although not yet reaching the requirements for industrialization of plasma-based NO_x synthesis, these results clearly show that improving the energy efficiency of plasma reactors is feasible through optimization of the reactor design. However, several other research questions still need to be addressed in future work to further enhance the energy efficiency of this process. The first question is how to further improve the design of the effusion nozzle to maximize its cooling efficiency and enable plasma ignition at lower power levels, while maintaining constant NO_x production. To answer this research question, a systematic screening study with various nozzle geometries needs to be conducted. Another research question is how specific materials can be effectively integrated into the electrode, reactor, and effusion nozzle, to improve heat transfer properties and, consequently, enhance the performance of the system in terms of quenching the backward reactions.

Exploring opportunities for process integration with other stages is also part of the plan to enhance process efficiency. For instance, cooling the hot gas after plasma can lead to more effective quenching of the backward reactions. The recovered heat can subsequently be used for preheating the feed gas, thereby enhancing the gas heating efficiency of the process. Also, integrating plasmas with a catalyst, as described in chapter 3, can improve the process performance. The catalyst should be positioned as close as possible to plasma, so that it can both use the heat produced by plasma before it is dissipated and interact with the plasma-produced species before they are quenched. However, coupling such warm plasmas with a catalyst can be very challenging, due to their high temperature, potentially leading to catalyst degradation through sintering of the catalyst particles (which leads to a drastic drop in number of active sites) and even metal evaporation. Nevertheless, there are some catalyst materials that are expected to serve this purpose. For example, one can envisage a highly thermally stable catalyst, consisting of active metals like Pd and Rh (with melting point of 2041 and 2236 K, respectively), supported on temperature-resistant materials, like SiC or Si_3N_4 (with melting point of 3000 and 3100 K, respectively) positioned very close to the plasma. Thus, a comparative study using several different catalysts (e.g., those suggested above) may aid in achieving more efficient and more selective production of NO and NO_2 in such systems.

- **How can we design a scaled-up, energy-efficient reactor for plasma-based NF?**

Another challenge toward the industrialization of plasma-based NF is reactor engineering to build an efficient scaled-up plasma reactor. In chapter 5, in collaboration with my colleague Ivan Tsonev, we tried to tackle this challenge by studying the feasibility of direct volume upscaling of plasma-based NF, specifically in terms of process efficiency. To this goal, we developed two reactors of very different throughput, and we explored three different reactor configurations: (I) a small pin-

to-pin reactor, (II) a large pin-to-pin reactor, and (III) the same large pin-to-pin reactor in a torch configuration. Throughout our experiments we studied plasma-based NO_x production in a wide range of specific energy input (SEI) values from 0.1 to 7.6 kJ/l.

The large reactor in the pin-to-pin configuration was unsuccessful in upscaling the technology due to the fundamental limitation that the gas passing through the plasma remained unchanged. As a result, although the same amount of NO_x, as the small reactor, is produced by the plasma in the large reactor, it gets diluted with non-reacted gas, leading to a lower NO_x concentration at the reactor outlet. Nevertheless, the production rate remains nearly unchanged due to the significantly higher flow rate in the large reactor. Transitioning the large reactor to a torch configuration doubled NO_x concentrations, resulting in a production rate of 80 g/h, while maintaining nearly the same EC (2.9 MJ/mol). This demonstrates that successful scaling up is achievable if we pay more attention to reactor design. Furthermore, based on our thermodynamic equilibrium calculations, we approached the thermodynamic minimum of the EC (2.74 MJ/mol) for NO_x production from air at atmospheric pressure. Moreover, our model proposed an approximate way to calculate the flow rate of the gas passing through the plasma – a useful analysis point for future development of plasma reactors.

Expanding this work further, we expect that increasing the pressure inside the reactor can substantially boost the NO_x concentration and decrease the energy cost, bringing the process closer to industrial applications. Additionally, given the observed variations in EC with varying SEI, exploring high flow rate plasma reactors in the high SEI region (>1 kJ/l) holds promise for further improving the efficiency and production rate of plasma-based NF. Based on the thermodynamic equilibrium calculations, there are strong indications that including quenching, either in the form of supersonic expansion or active water cooling, can further increase the PR, while keeping the EC low. Due to the synergy between the increased pressure and metrics of the process, supersonic expansion quenching could be a viable route towards efficient scaling up of the process [166]. These research directions provide exciting opportunities for advancing the field and overcoming the challenges of industrializing plasma-based nitrogen fixation.

7 Appendix

7.1 Calculation of adsorption, desorption and surface reaction rate coefficients

In this section we give more detailed information on the calculation of adsorption reaction rates as discussed in chapter 3, section 3.2.2. The rate coefficients for adsorption, desorption and surface reactions on Pt are defined based on transition state (TS) theory [167].

$$k = A\ exp\left(-\frac{E_a}{k_B T}\right) \tag{7.1}$$

$$A = \frac{k_B T}{h}\ exp\left(\frac{\Delta S^{\circ}_{TS}}{k_B}\right) \tag{7.2}$$

Where h is the Planck constant, T is the absolute temperature, ΔS°_{TS} is the standard entropy difference between the transition state and the initial state, k_B is the Boltzmann constant, and E_a is the activation energy of the reaction, as listed in table 2 in the main paper. For adsorption reactions we used the entropy of gas molecules as reported in the thermochemical database of NIST JANAF [168]. As in the transition state almost no molecular characteristics are observed, we calculate the entropy of the transition states as the sum of the entropies of atoms that are forming the corresponding molecule [169]. The entropies of the atomic adsorbates over Pt(211) are taken from Ma et al. and Bajpai et al [170,171]. The surface reactions are assumed to be entropy conservative and thus, $A = \frac{k_B T}{h}$.

The Treanor equation is applied for calculation of densities of different vibrationally excited states [45,115]. Since the population of vibrationally excited states higher than 10 is very low, only the first ten excited states are included [99]. N_2 and O_2 are assumed to have the same vibrational temperature. Ma et al. estimated a plasma vibrational temperature of 10000 K based on [116], and chose 6000 K as the representative value for vibrational temperature of post-plasma gas flow to the catalyst bed [99]. Therefore, $T_v = 6000\ \mathrm{K}$ is also used in our model. The Treanor vibrational distribution function used in our model is expressed by equation (7.3) [115] and is presented in Figure 7.1 for both N_2 and O_2 molecules.

$$p_v(v, T_v, T_g) = \frac{exp\left(-\frac{\hbar\omega v}{T_v} + \frac{\hbar x_e \omega v^2}{T_g}\right)}{\sum_{v=0}^{10} exp\left(-\frac{\hbar\omega v}{T_v} + \frac{\hbar x_e \omega v^2}{T_g}\right)} \tag{7.3}$$

Where $\hbar$ is the reduced Planck's constant, ω is the vibrational frequency, and x_e is the anharmonicity coefficient. ω of N_2 and O_2 are 2358.57 and 1580.16 cm^{-1}, respectively, while $x_e\omega$ are 14.324 and 11.951 cm^{-1}, respectively [172].

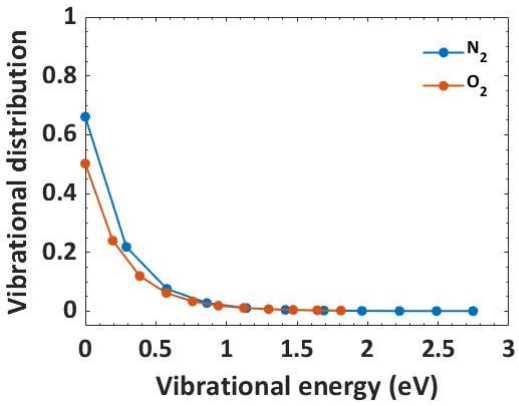

Figure 7.1. Treanor vibrational distribution function of N_2 and O_2 at $T_v = 6000\ K$ and $T_g = 873\ K$

The activation barrier of the reactions involving N_2 and O_2 molecules decreases upon vibrational excitation [45,117]. Therefore, the rate constant of each vibrational state, v, of the Zeldovich and dissociative adsorption of N_2 and O_2 on Pt are written as:

$$k_v = A \exp\left(-\frac{E_a - \alpha E_v}{k_B T}\right) \tag{7.4}$$

Where A is the pre-exponential factor as defined before, E_a is the activation energy of the ground vibrational state, E_v is the vibrational energy, α represents the effectiveness of vibrational excitation in surpassing the activation energy barrier, and it is estimated with the Fridman-Macheret α-model, $\alpha = \frac{E_a^{(f)}}{E_a^{(f)} + E_a^{(b)}}$, where $E_a^{(f)}$ and $E_a^{(b)}$ are the activation barriers for the forward and backward reactions, respectively (If $E_a - \alpha E_v \leq 0$ then $k_v = A$) [45].

The overall rate coefficient for the dissociative adsorption of N_2 and O_2 is calculated as the summation of the rates at different vibrationally excited states times the population of the corresponding state (as determined from the vibrational distribution function) as follows:

$$k_{ads} = \sum_{v=0}^{10} p_v k_v \tag{7.5}$$

7.2 Measured NO and calculated N_2, O_2, N and O concentrations entering the catalyst bed

In this section we provide more detailed information to support the discussion in chapter 3, section 3.3.1. The set of differential equations describing the catalytic system under study is very sensitive to the values set as initial and boundary conditions. This is specifically true for the NO and N post-plasma concentration, entering the catalyst bed. Therefore, selecting appropriate

initial conditions is highly important for the model to predict reliable results. The post-plasma, as well as post-catalytic NO concentration is measured by Ma et al. [99] and their measured values as function of O_2 fraction in the feed gas are listed in Table 7.1.

Table 7.1. Measured post-plasma and post-catalytic NO concentrations as a function of O_2 fraction in the feed gas [99].

x_{O_2}	$C_{NO}^{after\ plasma}$ $(\mathrm{mol\ m^{-3}})$	$C_{NO}^{after\ catalyst}$ $(\mathrm{mol\ m^{-3}})$
0.17×10^{-3}	1.53×10^{-7}	0.024×10^{-3}
0.35×10^{-3}	2.70×10^{-7}	0.049×10^{-3}
0.52×10^{-3}	4.13×10^{-7}	0.061×10^{-3}
0.7×10^{-3}	4.4×10^{-7}	0.059×10^{-3}
0.87×10^{-3}	5.73×10^{-7}	0.058×10^{-3}
1.04×10^{-3}	5.99×10^{-7}	0.055×10^{-3}
1.22×10^{-3}	6.12×10^{-7}	0.053×10^{-3}
1.39×10^{-3}	6.24×10^{-7}	0.052×10^{-3}
1.74×10^{-3}	5.59×10^{-7}	0.047×10^{-3}
2.09×10^{-3}	5.41×10^{-7}	0.042×10^{-3}
2.79×10^{-3}	5.13×10^{-7}	0.035×10^{-3}
3.48×10^{-3}	4.79×10^{-7}	0.027×10^{-3}
4.18×10^{-3}	4.12×10^{-7}	0.02×10^{-3}
5.57×10^{-3}	6.4×10^{-7}	0.013×10^{-3}
6.96×10^{-3}	8.74×10^{-7}	0.01×10^{-3}
0.01	29.12×10^{-7}	0.013×10^{-3}
0.014	68.56×10^{-7}	0.022×10^{-3}
0.017	0.13×10^{-4}	0.03×10^{-3}

0.021	0.23×10^{-4}	0.05×10^{-3}
0.035	0.75×10^{-4}	0.17×10^{-3}
0.1	1.94×10^{-4}	0.48×10^{-3}
0.15	2.15×10^{-4}	0.53×10^{-3}
0.2	2.21×10^{-4}	0.57×10^{-3}

Knowing the post-plasma concentration of NO, the $\mathrm{estimated\ N}$ radical concentration, and assuming that the $\mathrm{O_2}$ dissociation fraction in plasma is normally one order of magnitude greater than for $\mathrm{N_2}$ [116,123–126], we can calculate the post-plasma concentration of each species, as described below.

Knowing the $\mathrm{O_2}$ fraction in the feed gas, the $\mathrm{N_2}$ fraction in the feed gas can be calculated as follows:

$$x_{N_2} = 1 - x_{O_2} \tag{7.6}$$

Where x_{N_2} and x_{O_2} are the $\mathrm{N_2}$ and $\mathrm{O_2}$ mole fractions in the feed gas, respectively. Therefore the partial pressures of $\mathrm{N_2}$ and $\mathrm{O_2}$ in the feed gas can be calculated based on the total pressure, p_t, inside the plasma (i.e., 0.005 bar) as follows:

$$\bar{p}^0_{N_2} = x_{N_2} p_t \tag{7.7}$$

$$\bar{p}^0_{O_2} = x_{O_2} p_t \tag{7.8}$$

Clearly, the overall reaction of NO production ($\mathrm{N_2 + O_2 \leftrightarrow 2NO}$), does not increase the pressure of the system. Therefore, the instantaneous total pressure, $p_t^{ins.}$, after dissociation of $\mathrm{N_2}$ and $\mathrm{O_2}$ in the plasma, given by the dissociation degrees g_{N_2} and g_{O_2}, respectively, is given by:

$$p_t^{inst.} = \bar{p}^0_{N_2}\left(1 + g_{N_2}\right) + \bar{p}^0_{O_2}\left(1 + g_{O_2}\right) \tag{7.9}$$

The dissociation degrees are defined as $g_{N_2} = p_N / 2P^0_{N_2}$, and similar for $\mathrm{O_2}$. The dissociation degree of $\mathrm{O_2}$ is assumed 10 times higher than for N_2:

$$g_{O_2} = 10 g_{N_2} \tag{7.10}$$

As the post-plasma concentration of NO is known from the experiments, its instantaneous partial pressure can be calculated as:

$$\bar{p}_{NO}^{inst.} = C_{NO}^{ppm} p_t^{inst.} \times 10^{-6} \tag{7.11}$$

Where $C_{NO}^{ppm}$is the measured post-plasma concentration of NO in ppm and the factor 10^{-6} is used to convert the ppm concentration into NO fraction. The instantaneous partial pressure of other species (i.e., N_2, O_2, N and O) after dissociation and conversion in the plasma can be calculated based on the assumed dissociation degrees and the instantaneous partial pressure of NO calculated based on its measured concentration, as follows:

$$\bar{p}_{N_2}^{inst.} = \bar{p}_{N_2}^0 - \left(g_{N_2}\bar{p}_{N_2}^0\right) - \left(\frac{\bar{p}_{NO}^{inst.}}{2}\right) \qquad \bar{p}_{O_2}^{inst.} = \bar{p}_{O_2}^0 - \left(g_{O_2}\bar{p}_{O_2}^0\right) - \left(\frac{\bar{p}_{NO}^{inst.}}{2}\right)$$
$$\bar{p}_N = 2g_{N_2}\bar{p}_{N_2}^0 \qquad \bar{p}_O = 2g_{O_2}\bar{p}_{O_2}^0 \tag{7.12}$$

From equation (7.9 it is apparent that the pressure increases after dissociation. Therefore, we define a gas expansion factor, α, which enables us to calculate the post-plasma partial pressures of each species, while keeping the total pressure of the system constant (e.g., at 0.005 bar). The gas expansion factor can be calculated as follows:

$$\alpha = \frac{p_t}{p_t^{inst.}} \tag{7.13}$$

As a result, the post-plasma partial pressure of each species, $\bar{p}_i$, can be calculated as the product of the gas expansion factor and its corresponding instantaneous partial pressure as follows:

$$\bar{p}_i = \alpha \bar{p}_i^{inst.} \times 10^5 \tag{7.14}$$

Where the factor 10^5 is used to convert the partial pressures from bar to Pa. Finally, the post-plasma concentration of each species, C_i (i.e., the initial conditions used in our model for the gas phase species, (c.f., section 3.2.3), in units of $\mathrm{mol\ m^{-3}}$) can be calculated using the ideal gas law as follows:

$$C_i = \frac{\bar{p}_i}{RT_g} \tag{7.15}$$

Where R and T_g are the gas universal constant and temperature, respectively.

7.3 Dominant mechanisms toward NO production

In Figure 7.2. we plot the reaction rates as a function of time of the main reactions leading to NO production, at different positions of the catalyst bed. The results are calculated at $x_{O_2} = 20\%$ (and $T_g = 873\ K, P = 5\ mbar, Q = 1.67 \times 10^{-6}\ m^3 s^{-1}$, N_2 dissociation fraction $= 3.5 \times$

10^{-3}), which is one of the operating conditions for which the model was validated. An O_2 fraction of 20% was chosen, mimicking dry air composition, and therefore of special interest for industrial purposes.

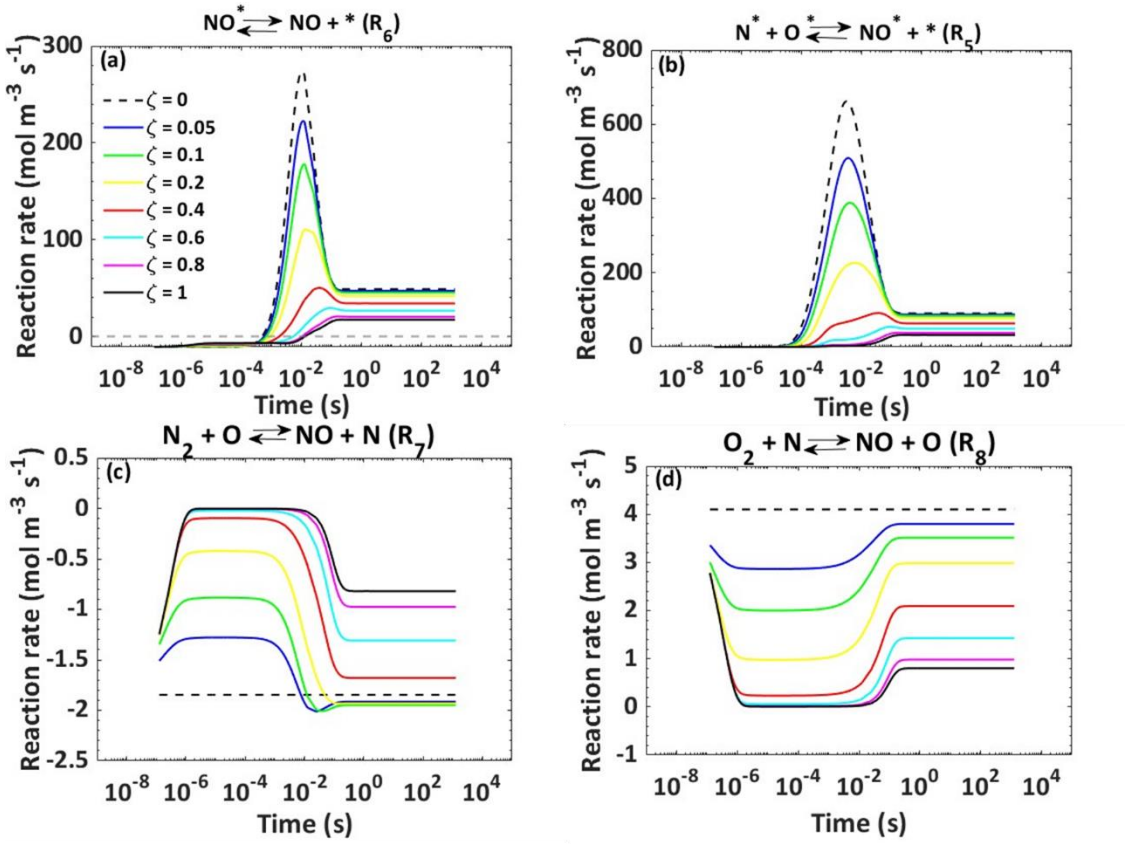

Figure 7.2. Temporal behavior of the net reaction rates of (a) NO desorption (R_6), (b) associative recombination of N^* and O^*radicals adsorbed at the catalyst surface (R_5), (c and d) the gas phase Zeldovich mechanisms (R_7, and R_8) at different positions across the catalyst bed (indicated in the legend by the dimensionless parameter ζ).

To obtain a complete picture of the reaction mechanisms, the temporal behavior of the net rates of the other reactions are presented in section 7.5. Note that the reactions are written as equilibrium reactions; if the net rate is positive, the reaction proceeds in the forward direction; vice versa, when it is negative, it proceeds in the backward direction.

At time zero, when the post-plasma gas enters the catalyst bed, the active sites on the catalyst surface are all free and therefore, the species in the gas phase become adsorbed on the surface. As a consequence of adsorption of gas phase NO on the surface, the net rate of NO desorption (R_6) from the surface is negative at the startup of the process ($t < 10^{-3}$ s), until its surface concentration reaches the amounts that can push the equilibrium toward the desorption of NO from the surface (Figure 7.2 a). Due to the lack of N and O radicals on the catalyst surface in the beginning, the rate of associative recombination (R_5) is almost zero at the startup of the process

(Figure 7.2 b). However, as soon as N and O radicals become adsorbed on the catalyst surface, they start to recombine to form NO. Therefore, the reaction rate of associative recombination (R_5) toward NO production on the surface starts to increase at around 10^{-4} s. Nevertheless, the NO desorption rate (R_6) rises a little bit later (around 10^{-3} s) as it takes some time for the NO concentration on the surface to be high enough to shift the equilibrium toward its desorption. As time passes, the rates of both associative recombination (R_5) and NO desorption (R_6) rise until they reach a maximum at t $\cong 10^{-2}$ s. At this maximum, the amount of produced NO through surface reactions is so high that it again promotes the adsorption of NO and its subsequent dissociation on the catalyst surface. Therefore, the net reaction rates of both associative recombination (R_5) and NO desorption (R_6) from the surface drop again until they reach a constant value at steady state (t $\geq 10^{-1}$ s). It should be noted that the associative recombination reaction (R_5), due to its lower activation energy (c.f., Table 3.3 in chapter 3, section 3.2.4), is always faster than NO desorption (R_6) (c.f. Figure 7.2 a and b).

A detailed analysis of the concentration and net reaction rate of each species in the gas phase in the catalytic bed and at the catalyst surface as a function of time and at different positions across the catalyst bed is presented in sections 7.4 and 7.6. In addition, analysis of the heat transfer in the catalyst bed is presented in section 7.7. According to Figure 7.3 a, the gas phase NO concentration rises in the axial direction. Simultaneously, a drop is observed in the axial direction for the surface concentrations of NO^*, N^*, and O^* (c.f., Figure 7.3 b, d, and g, respectively). The rise in the gas phase concentration of NO in the axial direction, promotes its adsorption on the surface. This, in addition to the drop in the concentrations of N^*, and O^*, which results in a drop in the net rate of associative recombination (R_5) in the axial direction (c.f. Figure 7.2 b), also leads to a drop in the net rate of NO desorption (R_6) from the surface in the axial direction (c.f. Figure 7.2 a).

Besides the associative recombination of N and O radicals at the catalyst surface and the subsequent desorption of the produced NO from the catalyst surface, which are the most important NO production mechanisms (c.f. their high reaction rates), NO can also be produced in the gas phase by the so-called Zeldovich reactions. However, the rates of these reactions are much lower, as can be observed from Figure 7.2 c and d.

The temporal behavior of the first Zeldovich reaction (R_7) is shown in Figure 7.2 c. It is clear that this reaction favors NO consumption throughout the whole period of the process. When the post-plasma gas flows into the catalyst bed, at first the reaction rate starts to increase until it reaches a maximum at around 10^{-6} s, after which its net rate stays constant until around 10^{-2} s. Subsequently, the net reaction rate drops again until it reaches a constant value at steady state (at around 0.1 s). The second Zeldovich reaction (R_8) on the other hand, experiences the opposite behavior (Figure 7.2 d). When the post-plasma gas enters the catalyst bed, the net rate of this reaction starts to drop at t $< 10^{-6}$ and it reaches a minimum at around 10^{-6} s, after which its net rate stays constant until around 10^{-2} s, when the net rate starts to slightly increase again,

until it reaches a constant value at steady state (at around 0.1 s). Note that, because the concentrations of all the gas phase species are constant at the inlet of the catalyst bed (i.e., they are equal to the post-plasma concentrations of species entering the catalyst bed) the net reaction rate of both Zeldovich reactions, at the inlet of the catalyst bed, (i.e., $\zeta = 0$) is constant throughout the whole period of the process.

According to Figure 7.2 c, the first Zeldovich reaction (R_7) favors the NO consumption throughout the whole period of the process, as well as in the axial direction. In contrast, the second Zeldovich reaction (R_8) always favors the NO production, both as function of time and position across the catalyst bed (c.f., Figure 7.2 d). The drop in the gas phase concentration of N radicals in the axial direction (c.f., Figure 7.3 c) slows down the rate of backward and forward pathways of the first and second Zeldovich reactions (R_7, R_8), respectively. As a result, we observe a rise (i.e., becoming less negative) and a drop (i.e., becoming less positive) in the net rate of the first and second Zeldovich reaction (R_7, R_8) in the axial direction, respectively.

In general, the total rate of both gas phase Zeldovich mechanisms (R_7, R_8) acts in favor of NO production (i.e., the sum of the net rate of both reactions is positive at steady state, meaning that they proceed towards NO production). However, the gas phase Zeldovich reactions play a negligible role, compared to the surface reactions (R_5, R_6) towards NO production. Indeed, this is obvious when comparing the net reaction rates of surface reactions that are in average between 1-2 orders of magnitude higher than those of gas phase Zeldovich reactions. This clearly indicates that the presence of the catalyst helps to significantly improve the NO production at the conditions under study.

7.4 Species concentrations to explain the NO production mechanisms

To better understand the temporal and spatial behavior of the reaction rates and how the presence of the catalyst helps to improve the process, we plot in Figure 7.3 the concentrations of all the species, both in the gas phase and at the catalyst surface, as a function of time at different positions in the catalyst bed.

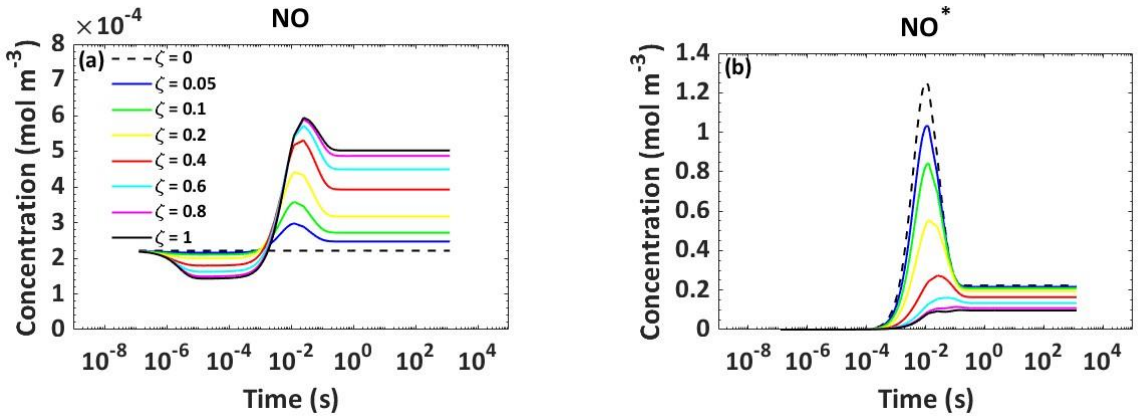

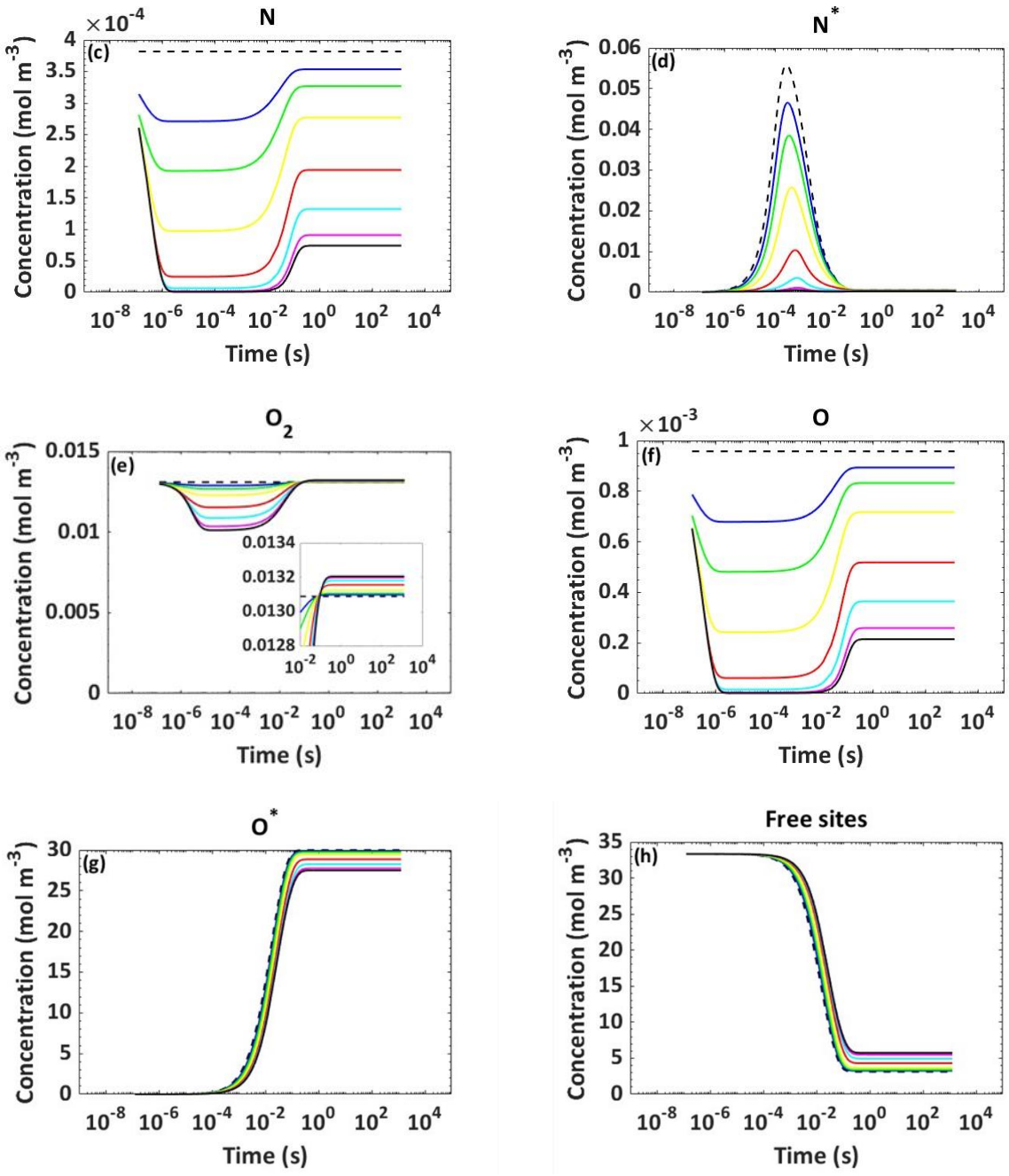

Figure 7.3. Temporal behavior of the concentrations of the system's different species in the gas phase (a, c, e, f) and at the catalyst surface (b, d, g, h) at different positions across the catalyst bed (Indicated in the legend by the dimensionless parameter, $\zeta = \frac{z}{L}$). $\mathrm{x_{O_2}} = 20\%, \mathrm{T_g} = 873\ \mathrm{K}, \mathrm{P} = 5\ \mathrm{mbar}, \mathrm{Q} = 1.67 \times 10^{-6}\ \mathrm{m^3 s^{-1}}, \mathrm{T_v} = 6000\ \mathrm{K}., \mathrm{N_2}$ dissociation fraction $= 3.5 \times 10^{-3}$

When the post-plasma gas enters the catalyst bed, some of the NO molecules already formed in the plasma are quickly adsorbed on the catalyst surface (the adsorption of NO on the surface is barrierless, c.f., Table 3.3 in chapter 3, section 3.2.4). Therefore, a slight initial decrease in the gas

phase NO concentration is observed ($t < 10^{-4}$ s, Figure 7.3 a). As time passes and the gas flows through the catalyst bed, the rate of associative recombination reaction (R_5) becomes more and more dominant due to adsorption of N and O radicals on the surface, starting at around 10^{-4} s (Figure 7.2 b). As a result, the NO concentration on the catalyst surface increases (Figure 7.3 b) until the NO adsorption/desorption process (R_6) shifts toward its desorption from the surface (at around 10^{-3} s, Figure 7.2 a), and the NO concentration on the catalyst surface starts to drop, until it reaches a constant value at steady state (at around 0.1 s, Figure 7.3 b). Subsequently, the NO concentration in the gas phase gradually increases, until it reaches a maximum at around 10^{-2} s (Figure 7.3 a). At this maximum the NO concentration in the gas phase slightly drops again, until it reaches constant steady state value as well at around 0.1 s (Figure 7.3 a). The reason is that the amount of produced NO through surface reactions, and its subsequent desorption from the surface, and therefore its gas phase concentration is high enough to promote its adsorption on the catalyst surface. As a result, the net rate of NO desorption (R_6) decreases.

Adsorption of N radicals on the surface (R_3) is a barrierless process (c.f., Table 3.3, in chapter 3, section 3.2.4). When the post-plasma gas enters the catalyst bed, the gas phase N radicals quickly adsorb on the free active catalyst sites. Therefore, the N radical gas phase concentration drops, until around 10^{-6}s, (Figure 7.3 c) and its concentration increases on the catalyst surface (Figure 7.3 d) until it reaches a maximum at around 10^{-4} s. At this maximum, due to the high concentration of N radicals on the catalyst surface, the associative desorption reaction (R_1) of N radicals on the catalytic surface gets promoted (c.f., Figure 7.4 a) and the concentration of N_2 in the gas phase slightly increases (not shown in Figure 7.3, because the effect is barely visible). This, in addition to the contribution of N radicals in the associative recombination reaction (R_5) and its direct desorption from the catalyst surface (R_3), results in a drop of N radicals on the surface after the maximum is reached (10^{-4} s). Finally, as a consequence of direct desorption of N radicals from the catalyst surface, the N radical concentration in the gas phase starts to increase again at around 10^{-2} s until it reaches steady state (0.1 s).

Additionally, the temporal behavior of the N radical gas phase concentration also affects the behavior of the gas phase Zeldovich mechanisms. The drop in the gas phase concentration of N radicals at around 10^{-6} s slows down the backward pathway of the first Zeldovich and the forward pathway of the second Zeldovich reactions (R_7, and R_8, respectively). As a result, the first and second Zeldovich reaction rates exhibit a rise and drop, respectively (Figure 7.2 c and d). During the period in which the gas phase concentration of N radicals is constant (i.e., until around 10^{-2} s), the net rate of both Zeldovich reactions also stays constant. After this period, when the N radical gas phase concentration slightly increases at around 10^{-2} s, the first and second Zeldovich reaction rates are again characterized by a drop and a rise, respectively, until their net rate reaches a constant value at steady state (around 0.1 s), when the gas phase concentration of N radicals also reaches a constant value. Furthermore, this drop in the net rate of the first Zeldovich reaction (Figure 7.2 c) also contributes to the slight increase in the concentration of N_2 in the gas phase until it reaches a constant value at steady state (0.1 s).

Simultaneously, due to a very low energy barrier for O_2 dissociative adsorption (i.e., 0.17 eV, R_2) and zero energy barrier for O radical adsorption (c.f., R_4 in Table 3.3), the concentrations of both O_2 and O radicals in the gas phase decrease over time (Figure 7.3 e and f), and the concentration of O radicals on the surface dramatically increases (Figure 7.3 g). As time passes, the surface gets more and more covered by O radicals, and at steady state, almost all the catalyst active surface sites are covered by O radicals (c.f. the opposite profiles of Figure 7.3 g and h). As a result, when steady state is reached, the associative desorption of O radicals (R_2) as well as its direct desorption (R_4) from the catalyst surface become the dominant mechanisms within the system, due to the very high concentration of O radicals on the surface (c.f., Figure 7.4 c and d). Therefore, the concentrations of both O_2 and O in the gas phase increase again through O radical associative desorption and direct desorption from the surface, respectively (Figure 7.3 e and f) and they reach constant values at steady-state (around 0.1 s).

The spatial behavior of the species concentrations across the catalyst bed, which also explains the spatial behavior of the NO production reactions, is explained in detail in section 7.6, where we plot the production and loss rates of all the species, both in the gas phase and at the catalyst surface, as a function of axial position in the catalyst bed.

7.5 Temporal behavior of the net reaction rates at different positions across the catalyst bed

In section 7.3, we plotted the rates of the main reactions leading to NO production as a function of time, at different positions of the catalyst bed, i.e., reactions R_5, R_6, R_7 and R_8. To obtain a complete picture of the reaction mechanisms, the temporal behavior of the net reaction rates for N_2 and O_2 dissociative adsorption (R_1 and R_2), as well as N and O radical adsorption on the surface (R_3 and R_4) are presented in Figure 7.4 a-d. At the startup of the process, almost no dissociative adsorption of N_2 on the catalyst surface (R_1) happens, due to its very high activation energy barrier, and its net rate stays almost zero until around 10^{-6} s (Figure 7.4 a). As the concentration of N radicals on the catalyst surface starts to increase (at around 10^{-6} s, Figure 7.3 d), due to its fast adsorption on the surface (N radical adsorption is a barrierless process, c.f., Table 3.3 in chapter 3, section 3.2.4), associative desorption of N radicals gets promoted, and therefore, the net rate of N_2 dissociative adsorption (R_1) is negative until it reaches a minimum at around 10^{-4} s. Between 10^{-4} and 10^{-2} s, due to the higher rate of associative recombination on the surface (R_5) and direct desorption of N radicals from the surface, the rate of associative desorption of N radicals from the surface decreases and therefore, the net rate of N_2 dissociative adsorption (R_1) increases (i.e., becomes less negative) until it goes back to zero at steady state (around 0.1 s).

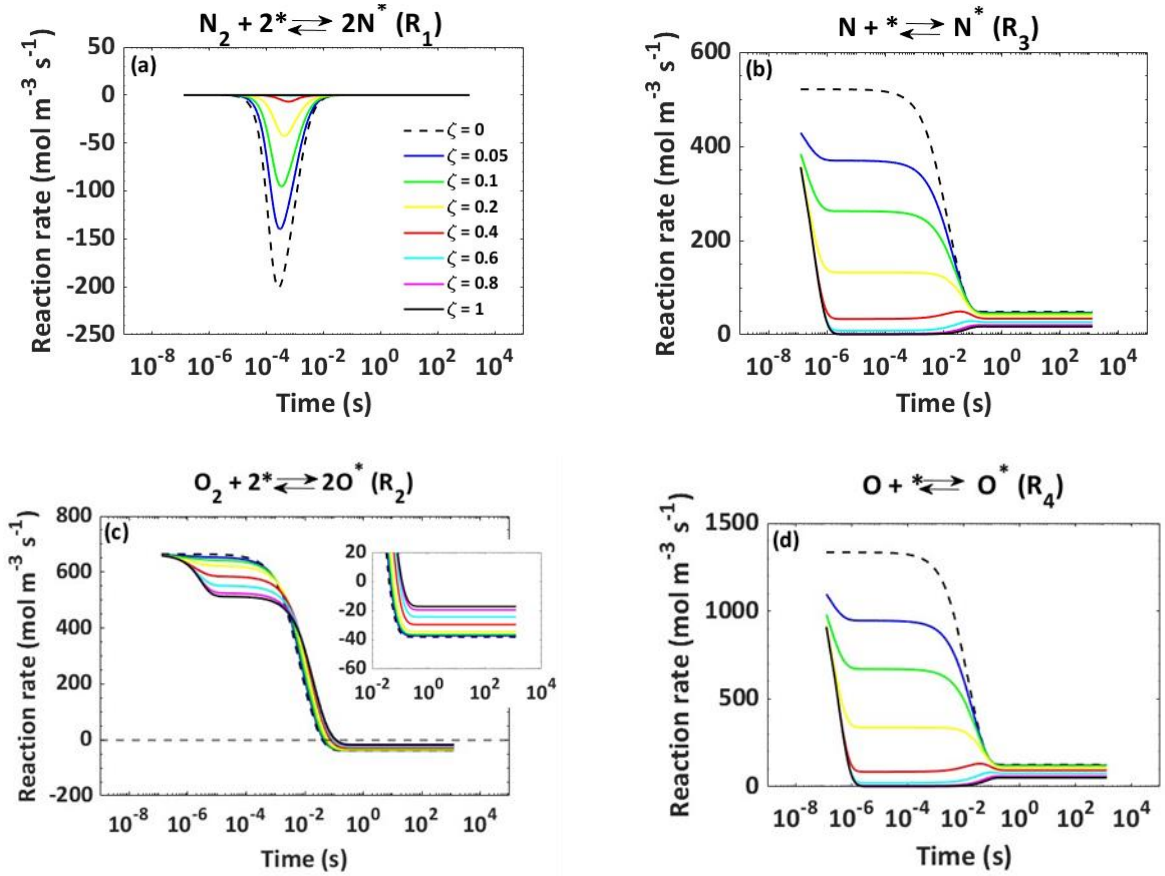

Figure 7.4. Temporal behavior of the net reaction rate of (a) dissociative adsorption of N_2 (R_1), (b) N radical adsorption (R_3), (c) dissociative adsorption of O_2 (R_2), and (d) O radical adsorption (R_4), at different positions across the catalyst bed (indicated in the legend by the dimensionless parameter $\zeta = \frac{z}{L}$). $x_{O_2} = 20\%, T_g = 873\ K, P = 5\ mbar, Q = 1.67 \times 10^{-6}\ m^3 s^{-1}, T_v = 6000\ K, N_2$ dissociation fraction $= 3.5 \times 10^{-3}$

At the startup of the process, the N radical adsorption (R_3) on the surface occurs at a relatively high rate (Figure 7.4 b). However, as a result, its concentration in the gas phase decreases until around 10^{-6}s. Therefore, the net rate of this process decreases until around 10^{-6} s. Between 10^{-6} and 10^{-3}s, the concentration of N radicals in the gas phase stays constant and therefore, their net rate of adsorption on the surface also stays constant. From 10^{-3}s the enhanced direct desorption of N radicals from the surface, due to their higher surface concentration, results in a lower net rate of N radical adsorption (R_3) on the surface, until it reaches a constant value at steady state (at around 0.1 s).

Due to a very low energy barrier for O_2 dissociative adsorption (i.e., 0.17 eV reaction barrier for R_2), and the high concentration of O_2 in the gas phase, this process occurs with high rates at the startup of the process (Figure 7.4 c). As a result of the drop in concentration of O_2 in the gas phase until 10^{-5} s, the net rate of O_2 dissociative adsorption drops. As the concentration of O_2 in the

gas phase stays almost constant until around 10^{-3} s (Figure 7.3 e), almost no variation is observed in the net rate of O_2 dissociative adsorption. Starting from 10^{-3} s, the dramatic increase in the surface concentration of O radicals (Figure 7.3 g), increases the rate of their associative desorption from the surface, and the net rate of O_2 dissociative adsorption (R_2) drops significantly until it reaches a constant negative value at steady state (around 0.1 s), meaning that when steady state is reached, no O_2 dissociative adsorption occurs in the catalyst bed and the process mostly works in favor of associative desorption of O radicals from the surface.

Finally, as O radical adsorption is a barrierless process (c.f., Table 3.3 in chapter 3, section 3.2.4), this process occurs with very high rates at the startup of the process, due to the relatively high concentration of O radicals in the post-plasma gas entering the catalyst bed (Figure 7.4 d). The drop in the concentration of O radicals in the gas phase until 10^{-6} s results in a drop in the net rate of the O radical adsorption (R_2). From 10^{-6} to around 10^{-3} s the concentration of O radicals in the gas phase stays constant and therefore no variations in the net rate of O radical adsorption (R_2) is observed. Starting from 10^{-3} s, the rate of direct desorption of O radicals from the surface increases, due to the dramatic rise of their surface concentration, which results in a significant drop in the net rate of O radical adsorption (R_2) until it reaches a constant value at steady state (around 0.1 s).

7.6 Species formation and loss rates in the axial direction

A big advantage of our model is that it provides information on the axial profiles of the species concentrations and reaction rates, which can give more insight in the actual mechanisms. Therefore, in this section we plot the steady state production and loss rates of each species as a function of dimensionless position ($\zeta = \frac{z}{L}$) across the catalyst bed in Figure 7.5.

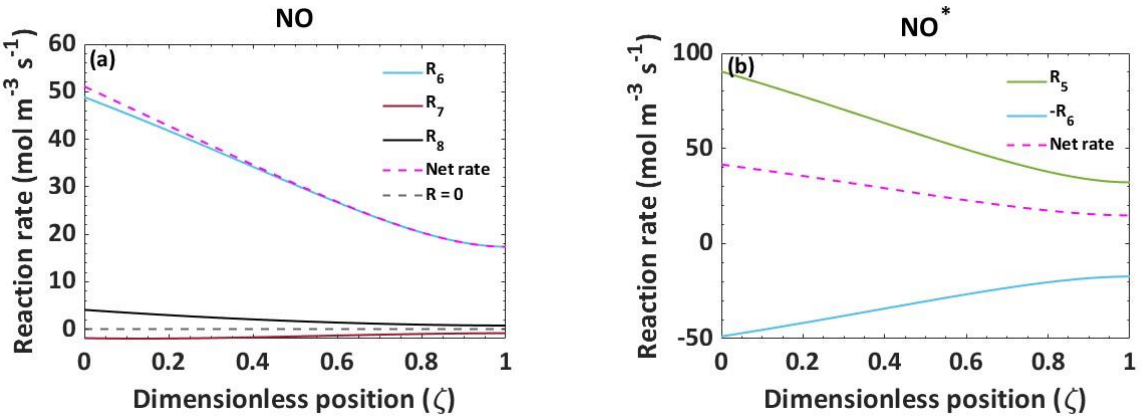

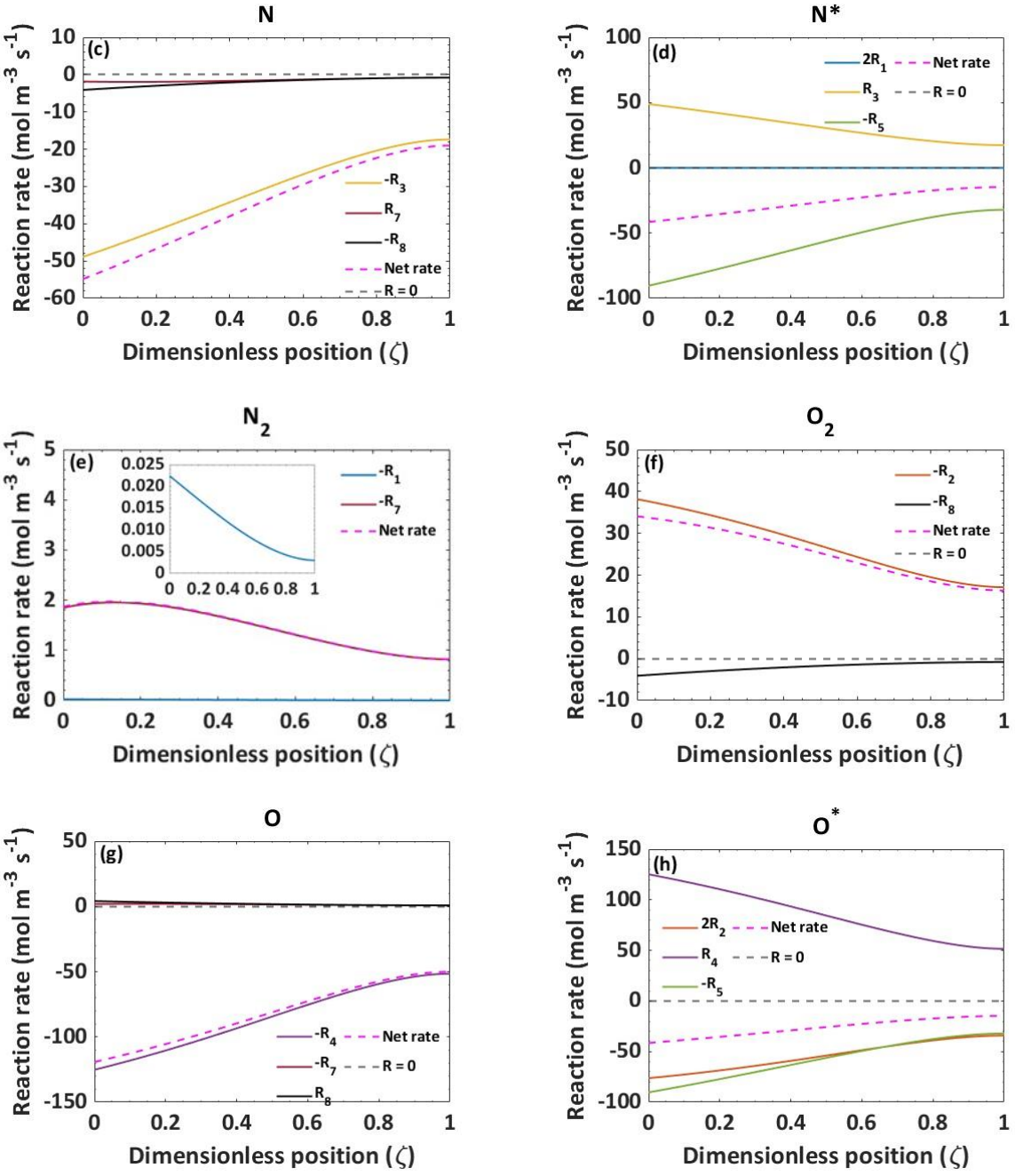
N
(c)
Reaction rate (mol m-3 s-1)
Dimensionless position (ζ)
-R3
R7
-R8
Net rate
R = 0
N*
(d)
2R1
Net rate
R3
R = 0
-R5
N2
(e)
-R1
-R7
Net rate
O2
(f)
-R2
-R8
Net rate
R = 0
O
(g)
-R4
Net rate
-R7
R = 0
R8
O*
(h)
2R2
Net rate
R4
R = 0
-R5

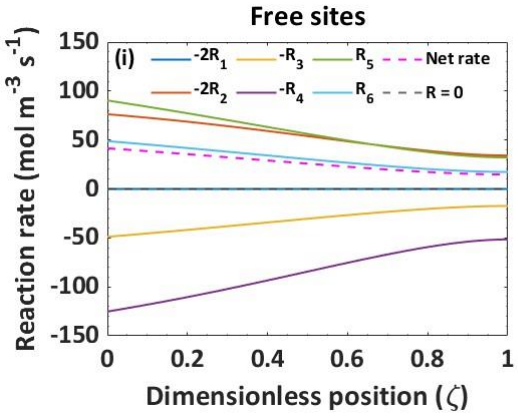

Figure 7.5. Axial profiles of the various production and loss rates of the different species in the gas phase (a, c, e, f, g), and on the catalyst surface (b, d, h, i) as a function of dimensionless position (ζ) from the catalyst bed inletat $\mathrm{x_{O_2}} = 20\%, \mathrm{T_g} = 873\ \mathrm{K}, \mathrm{P} = 5\ \mathrm{mbar}, \mathrm{Q} = \ 1.67 \times 10^{-6}\ \mathrm{m^3 s^{-1}}, \mathrm{T_v} = 6000\ \mathrm{K}, \mathrm{N_2}$ dissociation fraction $= \ 3.5 \times 10^{-3}$. A positive or negative reaction rate stands for production and loss, respectively. A negative sign for "R" in the legend represents the consumption of a species through the reaction listed in table 2 or 3.

As observed by Ma et al. [99] both experimentally and through their model, the coupled plasma and catalyst promotes the process towards higher overall production of NO. Additionally, we showed in section 7.3 (Figure 7.2), that in such a system the mechanisms happening due to the presence of the catalyst have much higher rates than the gas phase Zeldovich reactions ($\mathrm{R_7}$ and $\mathrm{R_8}$). The rate of production or destruction of NO through different mechanisms in the axial direction of the catalyst bed is shown in Figure 7.5 a. As can be seen, in the gas phase, NO is consumed through the first Zeldovich reaction ($\mathrm{R_7}$) and it is produced through the second Zeldovich reaction ($\mathrm{R_8}$), but by far the most important production is by desorption from the catalyst surface ($\mathrm{R_6}$). The same effect was observed by Ma et al. [99]. As the net production rate of NO is always positive throughout the whole catalyst bed, its gas phase concentration increases across the catalyst bed (Figure 7.3 a). However, as we get closer to the outlet of the catalyst bed, a drop in the NO net production rate is observed (see Figure 7.5 a). The reason is the drop in the net rate of NO desorption ($\mathrm{R_6}$), due to the lower surface concentration of NO in the axial direction (Figure 7.3 b), which is the most important mechanism that controls the net production rate of NO in the gas phase.

At the catalyst surface, NO is produced through associative recombination ($\mathrm{R_5}$), and it is consumed through desorption from the surface ($\mathrm{R_6}$). The NO desorption, due to its higher energy barrier (c.f., Table 3.2 in chapter 3, section 3.2.4), is always slower than its production on the catalyst surface through associative recombination ($\mathrm{R_5}$). As a result, the net production rate of NO on the catalyst surface is always positive (Figure 7.5 b). As the flowing gas gets closer to the outlet of the catalyst bed, the rates of both recombination ($\mathrm{R_5}$) and desorption ($\mathrm{R_6}$) decrease. As the NO desorption from the surface ($\mathrm{R_6}$) is the mechanism that controls the net NO production

rate in the gas phase (Figure 7.5 a), its decrease results in a drop of the net rate of NO production across the catalyst bed.

In the gas phase the N radicals are consumed through the Zeldovich mechanism (R_7 and R_8), but especially by adsorption on the catalyst surface (R_3). Therefore, the net rate of the N radicals is always negative (i.e., they are always consumed) throughout the catalyst bed (Figure 7.5 c). As a result, their gas phase concentration decreases as the flowing gas gets closer to the outlet of the catalyst bed (Figure 7.3 c). The drop in gas phase concentration of N radicals in the axial direction slows down their adsorption. Therefore, their net consumption rate becomes lower as the gas approaches the outlet of the catalyst bed.

As can be seen in Figure 7.5 d, on the catalyst surface, the N radicals are produced through adsorption from the gas phase (R_3) as well as N_2 dissociative adsorption (R_1), although the latter turns out to be negligible due to a very high energy barrier. Simultaneously, it is consumed through associative recombination (R_5). As dissociative adsorption on the surface is negligible, the production of N radicals on the surface is only controlled by the amount of N radicals produced by the plasma that adsorb on the catalyst surface. At the same time, at steady state the surface is mostly covered by O radicals (Figure 7.3 g). As a result, as soon as N radicals are adsorbed on the catalyst surface, they quickly react with the O radicals on the surface and form NO through associative recombination (R_5). Hence, the rate of associative recombination (R_5) is always higher than N radical adsorption (R_3). Therefore, the net rate of N radicals on the catalyst surface is always negative (i.e., they are always consumed) throughout the catalyst bed, which leads to a drop in their concentration on the catalyst surface in the axial direction (Figure 7.3 d).

N_2 is produced through associative desorption of N radicals from the catalyst surface (R_1), as well as the first Zeldovich reaction (R_7). As a result, its net rate is always positive (i.e., it is produced, Figure 7.5 e), and its concentration increases throughout the catalyst bed. However, at steady state, the rate of the first Zeldovich reaction (R_7) is much higher than that of associative desorption of N radicals from the surface (R_1). As the flowing gas gets closer to the catalyst bed outlet, the amount of N radicals decreases both in the gas phase and on the catalyst surface (Figure 7.3 c and d). Therefore, the rates of both associative desorption of N radicals from the surface (R_1) and the first Zeldovich reaction (R_7) drop closer towards the catalyst bed outlet.

Simultaneously, O_2 in the gas phase is produced through associative desorption of O radicals (R_2) and it is consumed through the second Zeldovich reaction (R_8). However, the effect of the latter is much smaller than for associative desorption (R_2). As a result, the net rate of O_2 in the gas phase is always positive (i.e., it is produced, Figure 7.5 f), and its steady state concentration increases throughout the catalyst bed (Figure 7.3 e).

In the gas phase, O radicals are produced by the reverse process of the first Zeldovich reaction and by the forward second Zeldovich reaction (R_7, R_8), and consumed through direct adsorption on the catalyst surface (R_4). The latter reaction is much more important, and therefore, the net

rate of O radicals in the gas phase is always negative (i.e., it is always consumed, Figure 7.5 g), and thus, its concentration decreases throughout the catalyst bed (Figure 7.3 f). The drop in the amount of O radicals in the gas phase at positions closer to the catalyst bed outlet results in a drop in its adsorption rate on the surface and subsequently its net rate decreases.

At the catalyst surface, O radicals are produced through adsorption from the gas phase (R_4) and consumed through associative desorption from the surface (R_2) as well as associative recombination with N radicals (R_5) on the catalyst surface (Figure 7.5 h). The rate of O radicals on the catalyst surface is controlled by their consumption mechanisms, hence, their net rate is always negative (i.e., they are consumed), and their concentration decreases towards the outlet of the catalyst bed (Figure 7.3 g).

According to Figure 7.5 h, the rate of O radical adsorption (R_4) is 3-3.6 times higher than its net rate of consumption, as well as that of N radical adsorption on the catalyst surface (Figure 7.5 c). This results in accumulation of O radicals on the catalyst surface in steady state. This, in addition to the lower amount of N radicals on the catalyst surface at positions closer to the outlet of the catalyst bed, as well as NO desorption from the surface, results in a lower steady state surface concentration of NO in the axial direction (Figure 7.3 b).

All the surface reactions in Table 3.3 (Chapter 3, section 3.2.4) affect the active free sites on the catalyst surface as well (Figure 7.5 i). More free surface sites become available through associative recombination (R_5), associative desorption of O radicals (R_2), and NO desorption from the surface (R_6). At the same time, the surface sites become occupied through N and O radical adsorption (R_3, R_4, respectively). As the sum of the production rates of free active sites is greater than the sum of their consumption rates, the net rate of free active sites stays positive throughout the catalyst bed. As the O radicals are the dominant species that cover the free catalyst sites, the drop in their concentration in the axial direction results in a larger amount of active free sites at the catalyst surface (Figure 7.3 h).

7.7 Heat transfer analysis

Our model also accounts for the heat transfer in the catalyst bed. Therefore, in this section we present a detailed heat transfer analysis to investigate the temporal and spatial behavior of gas phase temperature inside the catalyst bed. The temporal behavior of the net heat flux in the system and the gas temperature, at different positions of the catalyst bed, is presented in Figure 7.6 a and b. Additionally, to better understand the behavior of gas temperature across the catalyst bed, the steady state heat fluxes due to each reaction, as well as the net heat flux of the whole process as a function of dimensionless position, are shown in Figure 7.6 c.

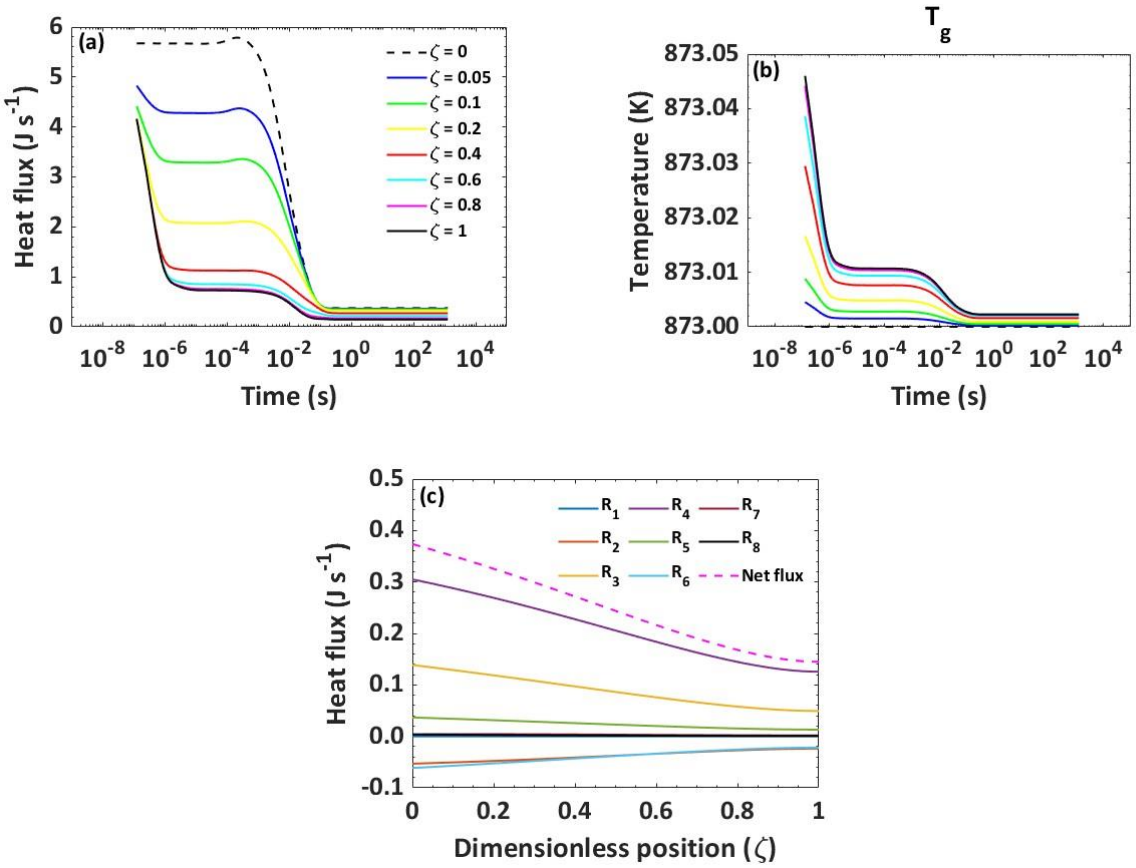

Figure 7.6. Net heat flux in the system (a), and gas temperature (b) as a function of time at different positions across the catalyst bed, and steady state heat flux due to each reaction, as well as the net heat flux of the system (c) as function of dimensionless position ($\zeta = \frac{z}{L}$) from the catalyst bed inlet at $x_{O_2} = 20\%, T_g = 873\ K, P = 5\ mbar, Q = 1.67 \times 10^{-6}\ m^3 s^{-1}, T_v = 6000\ K, N_2$ dissociation fraction $= 3.5 \times 10^{-3}$.

At the startup of the process ($t < 10^{-6}$ s), heat is released through all the reactions, except by dissociative adsorption of N_2 (R_1) and associative recombination of N and O radicals at the surface (R_5), as their rate at the process startup is almost zero. Therefore, a considerable heat flux is observed at the startup of the process (Figure 7.6 a). However, the net heat flux drops quickly until around 10^{-6} s, due to the drop in the rate of heat released in the reactions. In the time interval from 10^{-6} to around 10^{-2} s, the dissociative adsorption of N_2 (R_1) first starts to release heat until around 10^{-4} s, as it proceeds in the backward direction. Afterwards, the released heat by this reaction drops until it again becomes zero at around 10^{-2}, when its net rate becomes zero again (Figure 7.5 a). During this period of time, the rate of dissociative adsorption of O_2 (R_2) drops (Figure 7.5 c), and as a result, the released heat through this reaction drops as well. Simultaneously, the net rates of adsorption of N and O radicals (R_3 and R_4) and of the gas phase Zeldovich mechanism (R_7 and R_8) stay constant (Figure 7.4 b and d, and Figure 7.2 c and d, respectively), and therefore the released heat from these reactions stays constant. The rise in

the rate of associative recombination (R_5) results in an increase in heat released by this reaction (Figure 7.2 b). Finally, due the increase of the rate of NO desorption (R_6) from the catalyst surface, this process gradually becomes heat absorbing (Figure 7.2 a). In general, the variation in the released or absorbed heat by different reactions in the system is such that it keeps the net heat flux constant in the time period from 10^{-6} to around 10^{-2} s. Afterwards, the net heat flux of the system decreases again, due to the lower net rate of heat-releasing reactions until it reaches a constant value at steady state (around 0.1 s).

Due to the considerable heat flux (Figure 7.6 a) at the startup of the process ($t < 10^{-6}$ s), the gas temperature slightly increases (Figure 7.6 b). As time passes (until around 10^{-6} s) the gas temperature decreases again due to the drop in the net heat flux of the system, but still its temperature is slightly higher than its temperature at the inlet of the catalyst bed. During the period that the net heat flux of the system stays at a constant value (i.e., from 10^{-6} s to $t < 10^{-2}$ s), the gas temperature also stays constant. Afterwards, the gradual drop in the net heat flux of the system until it reaches a constant value at steady state (around 0.1 s), results in a drop in the gas temperature until it reaches a constant value at steady state. Overall, the gas temperature in the system is always negligibly higher than its temperature at the outlet of the reactor. The reason is that the net heat flux of the system is always positive throughout the whole catalyst bed. However, the increase in the temperature is so small that the whole process can be considered isothermal (c.f., the small variation in y-axis in Figure 7.6 b).

Throughout the whole catalyst bed, at steady state, heat is absorbed through associative desorption of O radicals from the surface (R_2) and through NO desorption (R_6). The other reactions release heat throughout the whole catalyst bed (Figure 7.6 c). However, the heat released through dissociative adsorption of N_2 (R_1), and the gas phase Zeldovich mechanism (R_7 and R_8), is negligible compared to the released heat through the adsorption of N and O radicals (R_3 and R_4) and associative recombination (R_5). The net heat flux throughout the catalyst bed is controlled by heat releasing reactions, as they release more heat compared to the heat absorbed by the associative desorption of O radicals from the surface (R_2) and the NO desorption process (R_6). As a result, the net heat flux of the system of reactions is always positive throughout the catalyst bed. Therefore, the gas temperature slightly increases in the axial direction (Figure 7.6 b). Additionally, due to the drop in the rate of all the reactions in the axial direction, the amount of released heat decreases closer to the catalyst bed outlet.

7.8 Effect of the catalyst bed characteristics length on the contact time of the gas with the catalyst, as well as surface and gas phase reactions

In Figure 7.7 a, we plot the effect of catalyst bed characteristic length on the contact time of the gas with the catalyst. An increase in the catalyst bed characteristic length results in a linear increase in the total volume of the catalyst bed. As a result, the contact time of the gas with the catalyst linearly increases with increasing catalyst bed characteristic length (c.f., the relationship

of the catalyst bed characteristic length with total volume of the catalyst bed and the contact time of the gas with catalyst in Table 3.1

Table 3.1 in chapter 3, section 3.2.2).

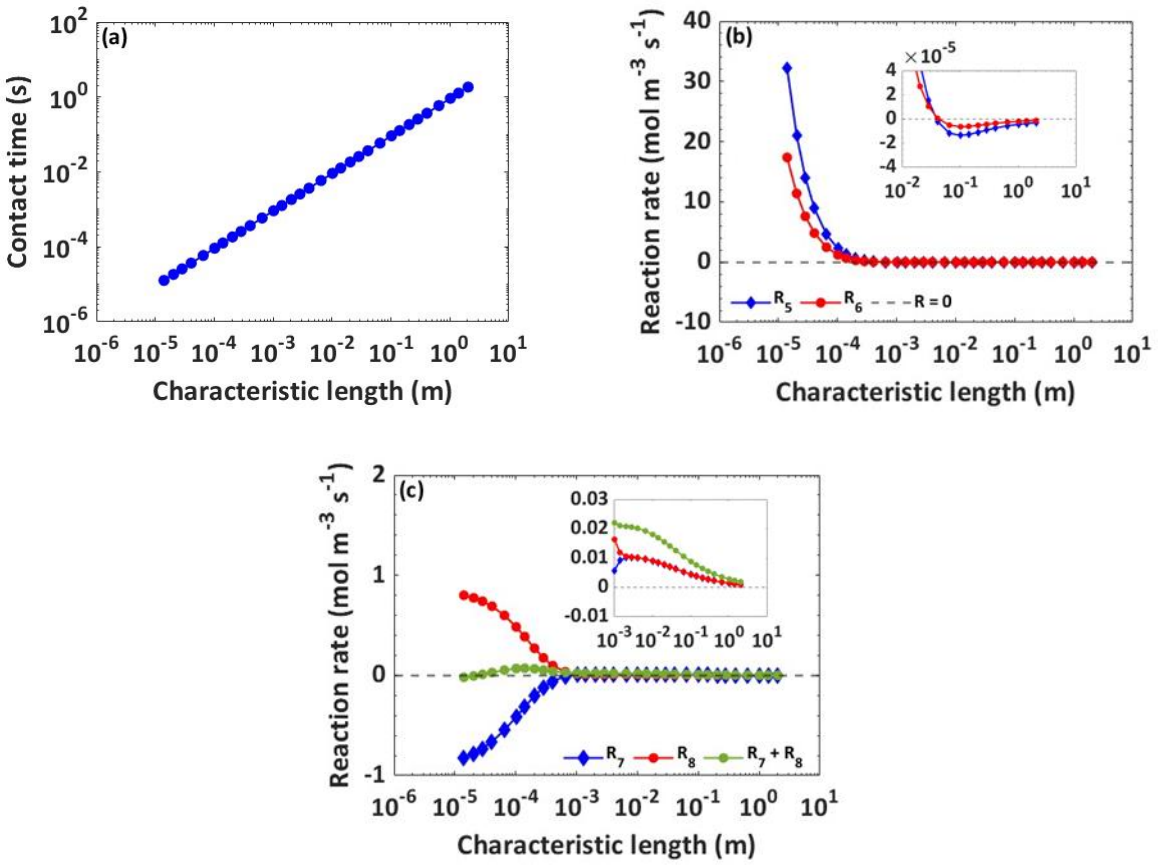

Figure 7.7. Effect of the catalyst bed characteristic length on (a) the contact time of the gas with the catalyst, (b) the net reaction rate of associative recombination of N and O radicals on the surface and NO desorption from the surface (R_5 and R_6), and (c) the net reaction rate of the gas-phase Zeldovich mechanisms (R_7 and R_8) and sum of both.

As the characteristic length of the catalyst bed increases, the net rate of associative recombination (R_5) and subsequent desorption of the produced NO (R_6) decrease dramatically, due to the enhanced NO adsorption on the surface and its subsequent dissociation into N and O radicals on the catalyst surface. This drop is that much that at characteristic lengths around 0.05 m and longer, not only the surface reactions have no contribution in NO production, but also the surface processes proceed toward NO destruction (c.f., inset in Figure 7.7 b).

A higher rate of NO adsorption and its subsequent dissociation on the surface, due to an increase in the catalyst bed characteristic length, results in a lower net reaction rate of N and O radical adsorption (R_3 and R_4, respectively) through their desorption from the catalyst surface. It is also observed in section 7.4 that at steady state the catalyst surface is mostly covered by O radicals and the O radical direct desorption is one of the dominant mechanisms. Therefore, the concentration of O radicals in the gas phase increases due to the higher rate of its direct desorption. The higher concentration of O radicals in the gas phase promotes the first Zeldovich reaction (R_7) towards production of NO, and as a result its net rate increases with increasing catalyst bed characteristic length (Figure 7.7 c). The net rate of the second Zeldovich reaction (R_8) on the other hand, decreases due to the promotion of its backward reaction as a result of the higher concentration of O radicals in the gas phase. However, its net rate stays toward NO production in the whole studied range of catalyst bed characteristic length (Figure 7.7 c).

Comparing the net reaction rate of NO desorption from the surface and the net reaction rate of gas phase Zeldovich reactions (green curve in Figure 7.7 c), we can observe that at low catalyst bed characteristic lengths ($< 10^{-4}$), the surface reactions are the dominant mechanisms that are controlling the NO production. However, at longer catalyst bed characteristic lengths, the gas phase Zeldovich reactions are the mechanisms that keep the process in favor of NO production, due to their higher net reaction rate.

7.9 Effect of catalyst bed diameter on the porosity and characteristic length of the catalyst bed

We plot the characteristic length and the porosity of the catalyst bed as a function of catalyst bed diameter in Figure 7.8 a and b, respectively. Increasing the diameter of the catalyst bed results in a higher catalyst bed cross section area, and thus the catalyst bed characteristic length decreases (Figure 7.8 a; c.f., the relationship of the catalyst bed characteristic length with the cross-section area of the catalyst bed in Table 3.1

Table 3.1 of chapter 3, section 3.2.2). The drop in characteristic length of the catalyst bed, due to the larger diameter of the catalyst bed, results in a smaller total volume of the catalyst bed (c.f.,

Table 3.1 Table 3.1 of chapter 3, section 3.2.2 for the relationship between the total volume of the catalyst bed and catalyst bed characteristic length), and therefore, the catalyst bed porosity drops (Figure 7.8 b; see also equation (2.37 in Chapter 2, section 2.6.2).

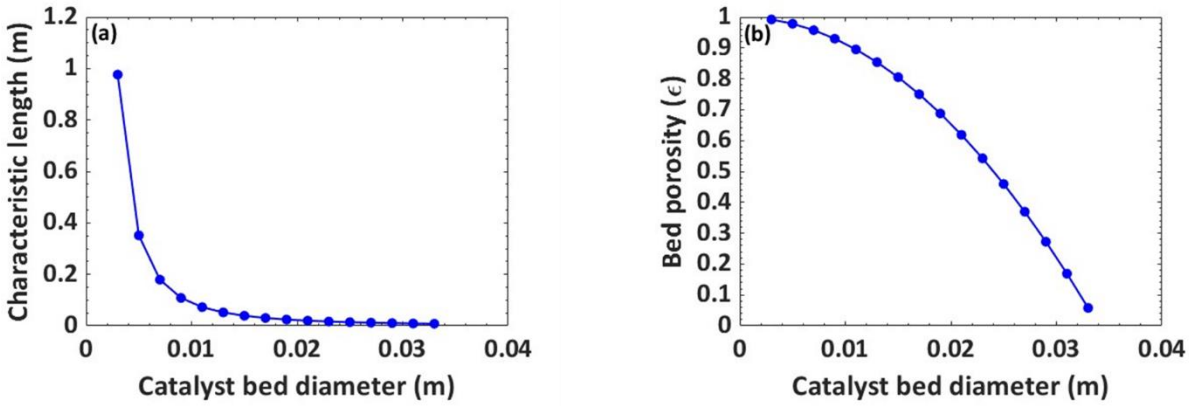

Figure 7.8. Effect of catalyst bed diameter on (a) characteristic length, and (b) porosity of the catalyst bed.

7.10 Experimental details of chapter 4

7.10.1 Experimental data for all operating conditions

Table 7.2 -Table 7.5. show the measured plasma power, NO and NO_2 concentration and EC for the experiments in the RGA with effusion nozzle (chapter 4), over a wide range of operating conditions, i.e., N_2/O_2 ratios ranging from 0.25 to 4, volumetric flow rates ranging from 1 to 10 ln/min and electrical currents from 60 to 200 mA. Each experiment was performed three times for each condition.

Figure 7.9 shows the time evolution of the measured NO_x concentration over a 65 min measurement for the best performing condition in chapter 4, i.e., a 50/50 N_2/O_2 gas composition at a flow rate of 2 ln/min in the steady arc regime (see Figure 4.5 in chapter 4, section 4.3.2). As demonstrated by this figure, the NO_x production in the RGA is quite reliable, reaching a steady NO_x concentration within 30 seconds, which remains stable for the full 65 min time period. Given the very steady NO_x production, all experiments were performed over a 5 min time period.

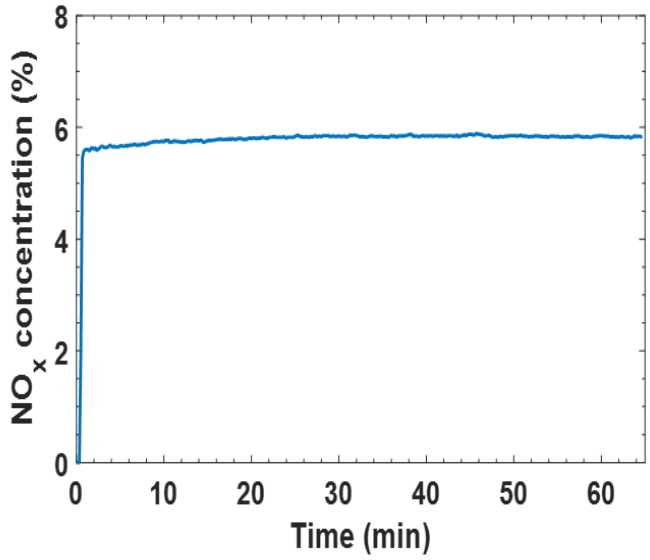

Figure 7.9. Time evolution of the measured NO_x concentration over a 65 min time period for a 50/50 N_2/O_2 gas composition at a flow rate of 2 ln/min in the steady arc regime.

Table 7.2. Total flow rate, applied current, plasma power, measured NO and NO_2 concentrations, and EC, as a function of gas composition, for the RGA with effusion nozzle operating in rotating arc regime.

	Gas composition (N_2/O_2)	Flow rate (ln/min)	Current (mA)	Plasma power (W)	Concentration (%)		EC (MJ/mol)
					NO	NO_2	
Measurement 1	20/80	2	56	99.73	0.74	1.16	3.79
	40/60	2	56	97.88	1.01	1.60	2.71
	50/50	2	56	96.43	1.14	1.55	2.58
	60/40	2	60	101.66	1.28	1.49	2.64
	70/30	2	64	106.43	1.43	1.27	2.84
	80/20	2	69	110.66	1.52	0.82	3.41
Measurement 2	20/80	2	56	96.75	0.77	1.11	3.69
	40/60	2	56	99.07	1.1	1.70	2.55
	50/50	2	60	103.26	1.25	1.73	2.49
	60/40	2	63	107.81	1.41	1.63	2.56
	70/30	2	68	109.97	1.53	1.31	2.79
	80/20	2	69	110.46	1.56	0.82	3.34
Measurement 3	20/80	2	55	97.47	0.77	1.07	3.81
	40/60	2	58	100.16	1.1	1.64	2.63
	50/50	2	60	103.32	1.25	1.70	2.52
	60/40	2	63	107.56	1.41	1.58	2.59
	70/30	2	68	116.64	1.55	1.30	2.95
	80/20	2	69	111.78	1.59	0.87	3.27

Table 7.3. Total flow rate, applied current, plasma power, measured NO and NO_2 concentrations, and EC as a function of gas composition, for the RGA with effusion nozzle operating in steady arc regime.

	Gas composition (N_2/O_2)	Flow rate (ln/min)	Current (mA)	Plasma power (W)	Concentration (%)		EC (MJ/mol)
					NO	NO_2	
Measurement 1	20/80	2	130	205.26	1.15	3.36	3.28
	40/60	2	135	214.27	1.52	4.01	2.79
	50/50	2	135	203.42	1.80	4.16	2.45
	60/40	2	135	188.81	1.98	3.54	2.46
	70/30	2	135	172.56	2.18	2.74	2.53
	80/20	2	135	155.85	2.25	1.64	2.89
Measurement 2	20/80	2	135	207.19	1.15	3.40	3.28
	40/60	2	135	219.13	1.55	4.15	2.77
	50/50	2	135	202.18	1.76	4.09	2.49
	60/40	2	135	188.58	1.97	3.55	2.46
	70/30	2	135	171.76	2.16	2.70	2.55
	80/20	2	135	158.41	2.26	1.64	2.51
Measurement 3	20/80	2	135	213.61	1.15	3.39	3.38
	40/60	2	135	216.13	1.56	4.29	2.66
	50/50	2	135	209.11	1.76	4.09	2.57
	60/40	2	135	185.95	1.98	3.53	2.43
	70/30	2	135	169.33	2.18	2.69	2.51
	80/20	2	135	162.48	2.27	1.60	3.03

Table 7.4. Total flow rate, applied current, plasma power, measured NO and NO_2 concentrations, and EC, as a function of gas composition, for the RGA without effusion nozzle operating in rotating arc regime.

	Gas composition (N_2/O_2)	Flow rate (ln/min)	Current (mA)	Plasma power (W)	Concentration (%)		EC (MJ/mol)
					NO	NO_2	
Measurement 1	20/80	2	60	102.64	0.81	1.07	3.94
	40/60	2	60	102.20	1.12	1.52	2.79
	50/50	2	60	100.60	1.25	1.48	2.66
	60/40	2	60	99.92	1.35	1.30	2.71
	70/30	2	65	94.96	1.47	1.07	2.69
	80/20	2	65	102.49	1.46	0.62	3.55
Measurement 2	20/80	2	60	104.42	0.85	1.11	3.84
	40/60	2	60	103.25	1.15	1.57	2.74
	50/50	2	60	103.03	1.27	1.54	2.64
	60/40	2	60	102.35	1.39	1.33	2.71
	70/30	2	64	104.33	1.49	1.02	2.99
	80/20	2	68	107.24	1.51	0.62	3.63
Measurement 3	20/80	2	60	101.51	0.83	1.08	3.83
	40/60	2	60	101.96	1.15	1.54	2.73
	50/50	2	60	102.34	1.28	1.49	2.66
	60/40	2	60	100.49	1.38	1.28	2.72
	70/30	2	64	112.98	1.48	1.03	2.23
	80/20	2	68	106.71	1.51	0.62	3.62

Table 7.5. Total flow rate, applied current, plasma power, measured NO and NO_2 concentrations, and EC, as a function of gas composition, for the RGA without effusion nozzle operating in steady arc regime.

	Gas composition (N_2/O_2)	Flow rate (ln/min)	Current (mA)	Plasma power (W)	Concentration (%)		EC (MJ/mol)
					NO	NO_2	
Measurement 1	20/80	2	135	204.33	1.2	3.15	3.38
	40/60	2	135	211.99	1.58	3.76	2.86
	50/50	2	135	226.28	1.80	3.64	2.99
	60/40	2	135	221.55	2.01	3.19	3.07
	70/30	2	135	195.73	2.19	2.48	3.02
	80/20	2	135	193.43	2.28	1.46	3.72
Measurement 2	20/80	2	135	217.61	1.19	3.02	3.72
	40/60	2	135	239.52	1.61	3.78	3.20
	50/50	2	135	231.71	1.82	3.63	3.06
	60/40	2	135	225.81	2.05	3.24	3.08
	70/30	2	135	214.70	2.21	2.45	3.31
	80/20	2	135	205.59	2.29	1.49	3.91
Measurement 3	20/80	2	135	224.90	1.18	2.99	3.88
	40/60	2	135	235.79	1.63	3.86	3.09
	50/50	2	135	225.05	1.83	3.70	2.93
	60/40	2	135	212.41	2.03	3.12	2.92
	70/30	2	135	208.78	2.23	2.47	3.20
	80/20	2	135	196.73	2.28	1.48	3.77

7.10.2 Diagnostic device specification, calibration and standard curves used for NO_x measurements of chapter 4

In all gas conversion experimental setups, diagnostic devices are always one of the key components for measuring the amounts of desired products in the outlet stream of the process. For quantitative analysis of the desired species (NO, NO_2), a non-dispersive infrared (NDIR) continuous gas analyzer (EMERSON-Rosemount X-STREAM enhanced XEGP) was used as the diagnostic device in our experiments. The NDIR analyzer is designed to continuously determine the concentration of NO and NO_2 in the flowing gaseous mixtures fed to the device. The measured concentrations can be extracted from the device in ppm or volume percent scales.

Like all other conventional diagnostic devices, NDIR needs regular calibration to achieve the best and most proper measuring results. The calibration procedure for the NDIR in general consists of three different steps that are separately explained below:

Zero calibration is a requirement to set the zero point of the measurement for the device. In this step a background gas recommended by the producer company (in our case pure nitrogen) is fed to the device and a zero-cal procedure will be followed according to the user manuals of the device.

Span calibration is the other important step in the calibration of the device to set the maximum point of measurement for the device. In this step a gaseous mixture with concentrations of 80 to 110% of the upper measuring range limit of the gas analyzer sensor is fed to the device and a span-cal procedure is followed according to the user manuals provided by the producer company

Generation of the standard curves is the third and the last step in the calibration procedure of the device. In this step different gaseous flows with different concentrations from zero to the upper measuring range limit of the gas analyzer are fed to the device and the measured values by the device are recorded. By plotting the measured values by the device as function of actual fed gaseous mixtures, a standard curve is generated which can then be used for accurate measurements of the desired products in the outlet stream of the experimental reactor set-up. The standard curves used for NO and NO_2 measurements in our experiments are presented in Figure 7.10.

Sampling flow rate fed to the device is also important in accurate measurements of the concentrations of components in the outlet stream of the process. The recommended sample flow rate by the device producer company is 500 to 1000 SCCM. Based on the manuals of the device, a lower flow sample should not affect the measured values by the device but may result in an undesirable time lag in the measurements. However, according to our experiences, a lower flow rate results in an overestimation of the measured concentrations. Therefore, sampling flow rates in the range of 980 to 1000 SCCM were fed to the device in all experiments to measure the concentrations of the products as accurately as possible. It should also be noted that excessive

sampling flow rates can produce increased cell pressurization which results in reading errors and damages the sensors.

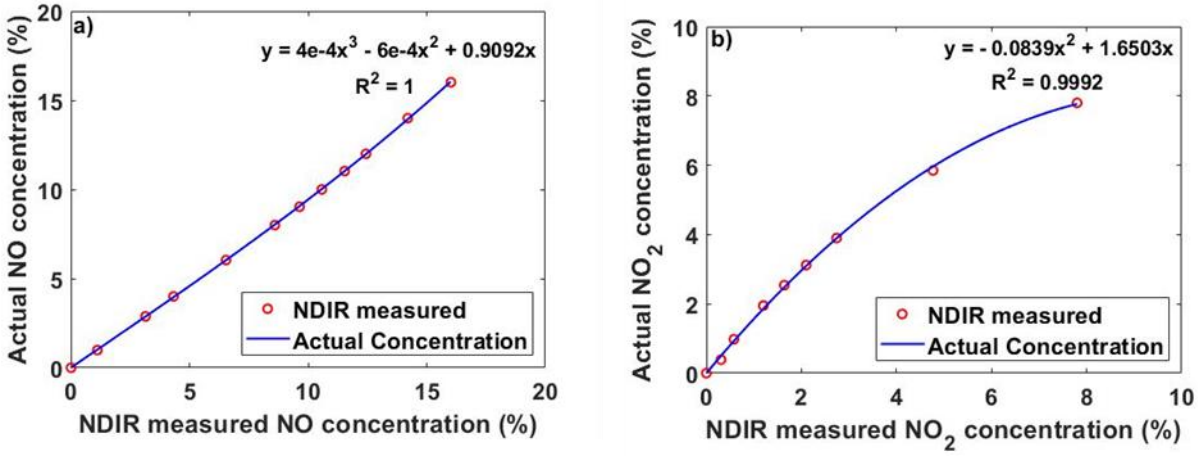

Figure 7.10. Standard calibration curves used for measuring actual concentrations of a) NO and b) NO_2 using NDIR.

References

[1] N. Greenwood, A. Earnshaw, Chemistry of the elements (second eddition), in: Butterworth-Heinemann, Oxford, 1997: pp. 406–472. https://doi.org/https://doi.org/10.1016/B978-0-7506-3365-9.50017-1.

[2] T.S. Ritchie, K.E. Riegner, R.J. Seals, C.J. Rogers, D.E. Riegner, Evolution of Medieval Gunpowder: Thermodynamic and Combustion Analysis., ACS Omega. 6 (2021) 22848–22856. https://doi.org/10.1021/acsomega.1c03380.

[3] M.E. Weeks, The discovery of the elements. IV. Three important gases, J. Chem. Educ. 9 (1932) 215. https://doi.org/10.1021/ed009p215.

[4] S. Li, J.A. Medrano, V. Hessel, F. Gallucci, Recent Progress of Plasma-Assisted Nitrogen Fixation Research: A Review, Processes. 6 (2018). https://doi.org/10.3390/pr6120248.

[5] A. Bernhard, The Nitrogen Cycle: Processes, Players, and Human Impact, Nat. Educ. Knowl. 3 (2010) 10–25.

[6] N. Cherkasov, A.O. Ibhadon, P. Fitzpatrick, A review of the existing and alternative methods for greener nitrogen fixation, Chem. Eng. Process. Process Intensif. 90 (2015) 24–33. https://doi.org/https://doi.org/10.1016/j.cep.2015.02.004.

[7] J.A. Manion, R.E. Huie, R.D. Levin, D.R.B. Jr., V.L. Orkin, W. Tsang, W.S. McGivern, J.W. Hudgens, V.D. Knyazev, D.B. Atkinson, E. Chai, A.M. Tereza, C.-Y. Lin, T.C. Allison, W.G. Mallard, F. Westley, J.T. Herron, R.F. Hampson, D.H. Frizzell, NIST Chemical Kinetics Database, NIST Standard Reference Database 17, Version 7.0 (Web Version), Release 1.6.8, Data version 2015.09, National Institute of Standards and Technology, Gaithersburg, Maryland, 20899-8320. Web address: https://kinetics.nist.go, (n.d.).

[8] S. Fields, Global nitrogen: cycling out of control., Environ. Health Perspect. 112 (2004) A556-63. https://doi.org/10.1289/ehp.112-a556.

[9] M. Roser, H. Ritchie, E. Ortiz-Ospina, L. Rodés-Guirao, World Population Growth, Our World Data. (2013). https://ourworldindata.org/world-population-growth.

[10] J.W. Erisman, M.A. Sutton, J. Galloway, Z. Klimont, W. Winiwarter, How a century of ammonia synthesis changed the world, Nat. Geosci. 1 (2008) 636–639. https://doi.org/10.1038/ngeo325.

[11] H. Liu, Ammonia synthesis catalyst 100 years: Practice, enlightenment and challenge, Cuihua Xuebao/Chinese J. Catal. 35 (2014) 1619–1640. https://doi.org/10.1016/S1872-2067(14)60118-2.

[12] FAO, Fertilizer use by crops, 2006. http://www.fao.org/tempref/docrep/fao/009/a0787e/A0787E00.pdf.

[13] L. Wang, M. Xia, H. Wang, K. Huang, C. Qian, C.T. Maravelias, G.A. Ozin, Greening Ammonia toward the Solar Ammonia Refinery, Joule. 2 (2018) 1055–1074. https://doi.org/https://doi.org/10.1016/j.joule.2018.04.017.

[14] C. Fúnez Guerra, L. Reyes-Bozo, E. Vyhmeister, M. Jaén Caparrós, J.L. Salazar, C. Clemente-Jul, Technical-economic analysis for a green ammonia production plant in Chile and its subsequent transport to Japan, Renew. Energy. 157 (2020) 404–414. https://doi.org/https://doi.org/10.1016/j.renene.2020.05.041.

[15] Y. Bicer, I. Dincer, C. Zamfirescu, G. Vezina, F. Raso, Comparative life cycle assessment of various ammonia production methods, J. Clean. Prod. 135 (2016) 1379–1395. https://doi.org/https://doi.org/10.1016/j.jclepro.2016.07.023.

[16] M. Thiemann, E. Scheibler, K.W. Wiegand, Nitric Acid, Nitrous Acid, and Nitrogen Oxides, in: Ullmann's Encycl. Ind. Chem., 2000. https://doi.org/https://doi.org/10.1002/14356007.a17_293.

[17] K.H.R. Rouwenhorst, F. Jardali, A. Bogaerts, L. Lefferts, From the Birkeland–Eyde process towards energy-efficient plasma-based NO_X synthesis: a techno-economic analysis, Energy Environ. Sci. 14 (2021) 2520–2534. https://doi.org/10.1039/D0EE03763J.

[18] M.A. Sutton, O. Oenema, J.W. Erisman, A. Leip, H. van Grinsven, W. Winiwarter, Too much of a good thing, Nature. 472 (2011) 159–161. https://doi.org/10.1038/472159a.

[19] J.N. Galloway, J.D. Aber, J.W. Erisman, S.P. Seitzinger, R.W. Howarth, E.B. Cowling, B.J. Cosby, The Nitrogen Cascade, Bioscience. 53 (2003) 341–356. https://doi.org/10.1641/0006-3568(2003)053[0341:TNC]2.0.CO;2.

[20] J.N. Galloway, A.R. Townsend, J.W. Erisman, M. Bekunda, Z. Cai, J.R. Freney, L.A. Martinelli, S.P. Seitzinger, M.A. Sutton, Transformation of the Nitrogen Cycle: Recent Trends, Questions, and Potential Solutions, Science (80-.). 320 (2008) 889–892. https://doi.org/10.1126/science.1136674.

[21] J.W. Erisman, J.N. Galloway, S. Seitzinger, A. Bleeker, N.B. Dise, A.M.R. Petrescu, A.M. Leach, W. de Vries, Consequences of human modification of the global nitrogen cycle, Philos. Trans. R. Soc. B Biol. Sci. 368 (2013) 20130116. https://doi.org/10.1098/rstb.2013.0116.

[22] C. Smith, A.K. Hill, L. Torrente-Murciano, Current and future role of Haber-Bosch ammonia in a carbon-free energy landscape, Energy Environ. Sci. 13 (2020) 331–344. https://doi.org/10.1039/c9ee02873k.

[23] C. Yoo, J. hoon Joo, S. young Jang, J.H. Yu, H.-N. Jeong, C.H. Hyeong, H.C. Yoon, J.-N. Kim, Electrochemical Ammonia Synthesis from Water and Nitrogen using Solid State Ion Conductors, in: NH_3 Fuel Conf., Ammonia energy association, Washington DC, USA, 2013. https://www.ammoniaenergy.org/paper/electrochemical-ammonia-synthesis-from-

water-and-nitrogen-using-solid-state-ion-conductors/.

[24] S.-J. Li, D. Bao, M.-M. Shi, B.-R. Wulan, J.-M. Yan, Q. Jiang, Amorphizing of Au Nanoparticles by CeO_x–RGO Hybrid Support towards Highly Efficient Electrocatalyst for N_2 Reduction under Ambient Conditions, Adv. Mater. 29 (2017). https://doi.org/10.1002/adma.201700001.

[25] C. Singer, E.J. Holmyard, A.R. Hall, T.I. Williams, E. Jaffé, R.H.G. Thomson, J.M. Donaldson, N.L. Clow, Y. Peel, J.R. Petty, M. Reeve, R. Raper, A history of technology, Clarendon Press Oxford University, London, Great Britain, Oxford University, London, Great Britain SE -, 1954. https://doi.org/LK - https://worldcat.org/title/751509.

[26] H.E. Wulff, The traditional crafts of persia, MIT press, Cambridge Mass, USA, 1966.

[27] B. Sørensen, A history of renewable energy technology, Energy Policy. 19 (1991) 8–12. https://doi.org/https://doi.org/10.1016/0301-4215(91)90072-V.

[28] M. A. and M, Applied solar energy, Addison-Wesley Reading, London, UK, 1976.

[29] L. Sprague de Camp, Ancient engineers, Tamdem Ltd., London, UK, 1977.

[30] D.S. Landes, The Unbound Prometheus: Technological Change and Industrial Development in Western Europe from 1750 to the Present, 2nd ed., Cambridge University Press, Cambridge, 2003. https://doi.org/DOI: 10.1017/CBO9780511819957.

[31] E. Kranakis, David A. Hounshell, From the American System to Mass Production, 1800–1932: The Development of Manufacturing Technology in the United States. Baltimore: Johns Hopkins University Press, 1984. xxi + 411 pp. illus., Int. Labor Work. Hist. 29 (1986) 127–130. https://doi.org/DOI: 10.1017/S014754790000065X.

[32] Z. KHAN, Creating the Twentieth Century: Technical Innovations of 1867–1914 and Their Lasting Impact. By Vaclav Smil. New York: Oxford University Press, 2005., J. Econ. Hist. 66 (2006) 535–536. https://doi.org/DOI: 10.1017/S0022050706270244.

[33] I. Bojanova, The Digital Revolution: What's on the Horizon?, IT Prof. 16 (2014) 8–12. https://doi.org/10.1109/MITP.2014.11.

[34] R.T. Wadanambi, L.S. Wandana, K.K.G.L. Chathumini, N.P. Dassanayake, D.D.P. Preethika, U.S.P.R. Arachchige, The effects of industrialization on climate change, J. Res. Technol. Eng. 1 (2020) 86–88.

[35] F. Ahmed, I. Ali, S. Kousar, S. Ahmed, The environmental impact of industrialization and foreign direct investment: empirical evidence from Asia-Pacific region, Environ. Sci. Pollut. Res. 29 (2022) 29778–29792. https://doi.org/10.1007/s11356-021-17560-w.

[36] S.A. Qadir, H. Al-Motairi, F. Tahir, L. Al-Fagih, Incentives and strategies for financing the

renewable energy transition: A review, Energy Reports. 7 (2021) 3590–3606. https://doi.org/https://doi.org/10.1016/j.egyr.2021.06.041.

[37] S. Hall, T.J. Foxon, R. Bolton, Investing in low-carbon transitions: energy finance as an adaptive market, Clim. Policy. 17 (2017) 280–298. https://doi.org/10.1080/14693062.2015.1094731.

[38] N. Howarth, M. Galeotti, A. Lanza, K. Dubey, Economic development and energy consumption in the GCC: an international sectoral analysis, Energy Transitions. 1 (2017) 6. https://doi.org/10.1007/s41825-017-0006-3.

[39] E. Parliament: Fit for 55, 2021.

[40] K.M. Van Geem, V. V Galvita, G.B. Marin, Making chemicals with electricity., Science. 364 (2019) 734–735. https://doi.org/10.1126/science.aax5179.

[41] K.M. Van Geem, B.M. Weckhuysen, Toward an e-chemistree: Materials for electrification of the chemical industry, MRS Bull. 46 (2021) 1187–1196. https://doi.org/10.1557/s43577-021-00247-5.

[42] R. Snoeckx, A. Bogaerts, Plasma technology – a novel solution for CO_2 conversion?, Chem. Soc. Rev. 46 (2017) 5805–5863. https://doi.org/10.1039/C6CS00066E.

[43] A. Bogaerts, E.C. Neyts, Plasma Technology: An Emerging Technology for Energy Storage, ACS Energy Lett. 3 (2018) 1013–1027. https://doi.org/10.1021/acsenergylett.8b00184.

[44] P.K. Chu, X. Lu, Low Temperature Plasma Technology: Methods and Applications, 1st ed., CRC Press, 2013. https://doi.org/https://doi.org/10.1201/b15153.

[45] A. Fridman, Plasma chemistry, Cambridge University Press, Cambridge, U.K., 2008. https://doi.org/10.1017/CBO9780511546075.

[46] J. Albo, M. Alvarez-Guerra, P. Castaño, A. Irabien, Towards the electrochemical conversion of carbon dioxide into methanol, Green Chem. 17 (2015) 2304–2324. https://doi.org/10.1039/C4GC02453B.

[47] E.N. Eremin, A.N. Mal'tsev, Thermodynamic equilibrium concentrations of nitrogen oxide, Russ. J. Phys. Chem. 30 (1956) 1179–1181.

[48] L. Hollevoet, F. Jardali, Y. Gorbanev, J. Creel, A. Bogaerts, J.A. Martens, Towards Green Ammonia Synthesis through Plasma-Driven Nitrogen Oxidation and Catalytic Reduction, Angew. Chemie Int. Ed. 59 (2020) 23825–23829. https://doi.org/https://doi.org/10.1002/anie.202011676.

[49] P.W. (Peter W. Atkins, J. De Paula, Atkins' Physical chemistry , 10th ed., Oxford University Press, Oxford, 2014.

[50] J.P. Trelles, Nonequilibrium Phenomena in (Quasi-)thermal Plasma Flows, Plasma Chem. Plasma Process. 40 (2020) 727–748. https://doi.org/10.1007/s11090-019-10046-1.

[51] A Gicquel, S Cavadias, J Amouroux, Heterogeneous catalysis in low-pressure plasmas, J. Phys. D. Appl. Phys. 19 (1986) 2013. https://doi.org/10.1088/0022-3727/19/11/003.

[52] J. Van Durme, J. Dewulf, C. Leys, H. Van Langenhove, Combining non-thermal plasma with heterogeneous catalysis in waste gas treatment: A review, Appl. Catal. B Environ. 78 (2008) 324–333. https://doi.org/https://doi.org/10.1016/j.apcatb.2007.09.035.

[53] L. Potočňáková, J. Šperka, P. Zikán, J.J.W.A. van Loon, J. Beckers, V. Kudrle, Experimental study of gliding arc plasma channel motion: buoyancy and gas flow phenomena under normal and hypergravity conditions, Plasma Sources Sci. Technol. 26 (2017) 45014. https://doi.org/10.1088/1361-6595/aa5ee8.

[54] T. Nunnally, K. Gutsol, A. Rabinovich, A. Fridman, A. Gutsol, A. Kemoun, Dissociation of CO_2 in a low current gliding arc plasmatron, J. Phys. D. Appl. Phys. 44 (2011) 274009. https://doi.org/10.1088/0022-3727/44/27/274009.

[55] Y.P. Raizer, M. Schneider, N.A. Yatsenko, Radio-Frequency Capacitive Discharges, Nauka (Science), Moscow, and CRC Press, New York, 1995.

[56] M.A. Lieberman, A.J. Lichtenberg, Principles of Plasma Discharges and Material Processing, JohnWiley & Sons, New York, 1994.

[57] E. P.J. Linstrom and W.G. Mallard, NIST Chemistry WebBook, NIST Standard Reference Database Number 69, National Institute of Standards and Technology, Gaithersburg MD, n.d. https://doi.org/https://doi.org/10.18434/T4D303.

[58] J.M. Smith, H.C. Van Ness, M.M. Abbott, Introduction to chemical engineering thermodynamics, 7th ed., McGraw-Hill Boston, Boston SE - xviii, 817 pages : illustrations ; 25 cm., 2005. https://doi.org/LK - https://worldcat.org/title/56491111.

[59] F. Jardali, S. Van Alphen, J. Creel, H. Ahmadi Eshtehardi, M. Axelsson, R. Ingels, R. Snyders, A. Bogaerts, NO_x production in a rotating gliding arc plasma: potential avenue for sustainable nitrogen fixation, Green Chem. 23 (2021) 1748–1757. https://doi.org/10.1039/D0GC03521A.

[60] J. Li, S. Yao, Z. Wu, NO_x production in plasma reactors by pulsed spark discharges, J. Phys. D. Appl. Phys. 53 (2020). https://doi.org/10.1088/1361-6463/ab946a.

[61] E. Vervloessem, M. Aghaei, F. Jardali, N. Hafezkhiabani, A. Bogaerts, Plasma-Based N_2 Fixation into NO_x: Insights from Modeling toward Optimum Yields and Energy Costs in a Gliding Arc Plasmatron, ACS Sustain. Chem. Eng. 8 (2020) 9711–9720. https://doi.org/10.1021/acssuschemeng.0c01815.

[62] B. Mutel, O. Dessaux, P. Goudmand, Energy cost improvement of the nitrogen oxides synthesis in a low pressure plasma, Rev. Phys. Appliquée. 19 (1984) 461–464. https://doi.org/10.1051/rphysap:01984001906046100.

[63] T. Kim, S. Song, J. Kim, R. Iwasaki, Formation of NOx from air and N_2/O_2 mixtures using a nonthermal microwave plasma system, Jpn. J. Appl. Phys. 49 (2010). https://doi.org/10.1143/JJAP.49.126201.

[64] R.I. Asisov, V.K. Givotov, V.D. Rusanov, A. Fridman, Synthesis of nitrogen oxides in a nonequilibrium UHF discharge under electron-cyclotron resonance conditions, High Energy Chem. 14 (1980) 366.

[65] F.B. Polak, L. S., Ovsiannikov, A. A., Slovetsky, D. I. & Vurzel, Theoretical and Applied Plasma Chemistry, Physical Society of the GDR, German Democratic Republic, 1975. http://inis.iaea.org/search/search.aspx?orig_q=RN:11500694.

[66] J. Creel, H. Ahmadi Eshtehardi, A. Bogaerts, Plasma reactor for plasma-based gas conversion comprising an effusion nozzle, World Intellectual Property Organization (WIPO), 2022, IP-No: WO 2022/234039 A1, 2022. https://data.epo.org/publication-server/document?iDocId=6952518&iFormat=0.

[67] Perry's Chemical engineers handbook, Sixth edit, McGraw-Hill, New York, 1984. https://search.library.wisc.edu/catalog/999552107102121.

[68] O. Levenspiel, Chemical Reaction Engineering, 17th ed., 1980. https://www.worldcat.org/title/chemical-reaction-engineering/oclc/299184407.

[69] H.S. Fogler, Elements of chemical reaction engineering, 5th ed., Prentice Hall, Philadelphia, PA, 2016.

[70] S. Gultekin, A. Kalbekov, Effect of backmixing on the performance of bubble column reactors, Int. J. Dev. Res. 7 (2017) 2. https://doi.org/10.1016/0009-2509(74)80081-3.

[71] I.M. Abu Reesh, Acrylonitrile process enhancement through waste minimization: Effect of reaction conditions and degree of backmixing, Sustain. 13 (2021) 7923. https://doi.org/10.3390/su13147923.

[72] R. Prichard, M. Gibson, C. Joseph, W. Strasser, Chapter 13 - A review of fluid flow in and around the brain, modeling, and abnormalities, in: R. Prabhu, M.B.T.-M.B.M. of the B. Horstemeyer (Eds.), Academic Press, 2022: pp. 209–238. https://doi.org/https://doi.org/10.1016/B978-0-12-818144-7.00015-3.

[73] S. Mishra, R.K. Upadhyay, Chapter 7 - Mass transfer by molecular diffusion, in: T. Sharma, K.R. Chaturvedi, J.J.B.T.-N. for C.U. in O.A. Trivedi (Eds.), Gulf Professional Publishing, 2022: pp. 99–125. https://doi.org/https://doi.org/10.1016/B978-0-323-90540-4.00003-X.

[74] O. Levenspiel, K.B. Bischoff, Patterns of Flow in Chemical Process Vessels, Adv. Chem. Eng. 4 (1964) 95–198. https://doi.org/10.1016/S0065-2377(08)60240-9.

[75] S.Z. Abbas, V. Dupont, T. Mahmud, Kinetics study and modelling of steam methane reforming process over a NiO/Al_2O_3 catalyst in an adiabatic packed bed reactor, Int. J. Hydrogen Energy. 42 (2017) 2889–2903. https://doi.org/10.1016/j.ijhydene.2016.11.093.

[76] F. Maqbool, S.Z. Abbas, S. Ramirez-Solis, V. Dupont, T. Mahmud, Modelling of one-dimensional heterogeneous catalytic steam methane reforming over various catalysts in an adiabatic packed bed reactor, Int. J. Hydrogen Energy. 46 (2021) 5112–5130.

https://doi.org/10.1016/j.ijhydene.2020.11.071.

[77] D. Nemec, J. Levec, Flow through packed bed reactors: 1. Single-phase flow, Chem. Eng. Sci. 60 (2005) 6947–6957. https://doi.org/10.1016/j.ces.2005.05.068.

[78] Unit operations of chemical engineering, Choice Rev. Online. 30 (1993) 30-6200-30–6200. https://doi.org/10.5860/choice.30-6200.

[79] E. Erdim, Ö. Akgiray, İ. Demir, A revisit of pressure drop-flow rate correlations for packed beds of spheres, Powder Technol. 283 (2015) 488–504. https://doi.org/https://doi.org/10.1016/j.powtec.2015.06.017.

[80] P.C. Carman, Fluid flow through granular beds, Trans. Inst. Chem. Eng. London. 15 (1937) 150–156.

[81] H.E. Rose, A.M.A. Rizk, Further researches in fluid flow through beds of granular material, Proc. Inst. Mech. Eng. 160 (1949) 493–511.

[82] B. Eisfeld, K. Schnitzlein, The influence of confining walls on the pressure drop in packed beds, Chem. Eng. Sci. 56 (2001) 4321–4329. https://doi.org/https://doi.org/10.1016/S0009-2509(00)00533-9.

[83] E. Reichelt, M. Jahn, Generalized correlations for mass transfer and pressure drop in fiber-based catalyst supports, Chem. Eng. J. 325 (2017) 655–664. https://doi.org/https://doi.org/10.1016/j.cej.2017.05.119.

[84] G. Cj., Transport processes and unit operations, Chem. Eng. J. 20 (1993) 82. https://doi.org/10.1016/0300-9467(80)85013-1.

[85] A. Kołodziej, J. Łojewska, Engineering Aspects of Catalytic Converters Designs for Cleaning of Exhaust Gases, in: New Futur. Dev. Catal., Elsevier, 2013: pp. 257–279. https://doi.org/10.1016/B978-0-444-53870-3.00010-1.

[86] N. Wakao, S. Kaguei, Heat and Mass Transfer in Packed Beds, Gordon and Breach Science Publisher, New York, 1982., Gordon & Breach, London, 1982.

[87] P.J. Handley, D., Heggs, the Effect Packing of Thermal Conductivity Bed of the Material on Transient in a Fixed, Int. J. Heat Mass Transf. 12 (1969) 549–570.

[88] M.F. Edwards, J.F. Richardson, Gas dispersion in packed beds, Chem. Eng. Sci. 23 (1968) 109–123. https://doi.org/10.1016/0009-2509(68)87056-3.

[89] R.T. Driessen, S.R.A. Kersten, D.W.F. Brilman, A Thiele Modulus Approach for Nonequilibrium Adsorption Processes and Its Application to CO_2 Capture, Ind. Eng. Chem. Res. 59 (2020) 6874–6885. https://doi.org/10.1021/acs.iecr.9b05503.

[90] J.M. smith Ch. wang, Tortuosity Factors for Diffusion in catalyst pellets, 29 (1983) 132–136. https://doi.org/https://doi.org/10.1002/aic.690290118.

[91] J.W.Beeckman, Mathematical description of Heterogeneous Materials, Chem. Eng. Sci. 45 (1990) 2603–2610.

[92] A. Blanc, Recherches sur les mobilités des ions dans les gaz, J. Phys. Théorique Appliquée. 7 (1908) 825–839. https://doi.org/10.1051/jphystap:019080070082501.

[93] E.N. Fuller, P.D. Schettler, J.C. Giddings, A new method for prediction of binary gas-phase diffusion coefficients, Ind. Eng. Chem. 58 (1966) 18–27. https://doi.org/10.1021/ie50677a007.

[94] B.E. Poling, J.M. Prausnitz, J.P. O'Connell, The Properties of Gases and Liquids, McGraw-Hill Education, 2000. https://books.google.com/books?id=9tGclC3ZRX0C.

[95] P. Fang, J. Wang, X. Li, S. Wu, W. Zhang, S. Li, Effect of platinum on sintering morphology of porous YSZ ceramics, Microsc. Res. Tech. 80 (2017) 889–897. https://doi.org/10.1002/jemt.22878.

[96] S. Yagi, D. Kunii, N. Wakao, Studies on axial effective thermal conductivities in packed beds, AIChE J. 6 (1960) 543–546. https://doi.org/10.1002/aic.690060407.

[97] E.W. Thiele, Relation between Catalytic Activity and Size of Particle, Ind. Eng. Chem. 31 (1939) 916–920. https://doi.org/10.1021/ie50355a027.

[98] A. Rutherford, Introduction to the analysis of chemical reactors, Englewood Cliffs, N.J., Prentice-Hall, 1965.

[99] H. Ma, R.K. Sharma, S. Welzel, M.C.M. van de Sanden, M.N. Tsampas, W.F. Schneider, Observation and rationalization of nitrogen oxidation enabled only by coupled plasma and catalyst, Nat. Commun. 13 (2022) 402. https://doi.org/10.1038/s41467-021-27912-2.

[100] E.C. Neyts, K. Ostrikov, M.K. Sunkara, A. Bogaerts, Plasma Catalysis: Synergistic Effects at the Nanoscale, Chem. Rev. 115 (2015) 13408–13446. https://doi.org/10.1021/acs.chemrev.5b00362.

[101] J.M. Henis, Nitrogen oxide decomposition process., U.S. Patent 3983021, 1976.

[102] D. Rapakoulias, S. Cavadias, J. Amouroux, Processus catalytiques dans un réacteur à plasma hors d'équilibre II. Fixation de l'azote dans le système N_2-O_2, Rev. Phys. Appliquée. 15 (1980) 1261–1265. https://doi.org/10.1051/rphysap:019800015070126100.

[103] Q. Sun, A. Zhu, X. Yang, J. Niu, Y. Xu, Formation of NO_x from N_2 and O_2 in catalyst-pellet filled dielectric barrier discharges at atmospheric pressure, Chem. Commun. (2003) 1418–1419. https://doi.org/10.1039/B303046F.

[104] A.N.M. V.M. Belova, E.N. Eremin, Heterogeneous catalytic oxidation of nitrogen in a glow discharge II 1:1 nitrogen-oxygen mixture., Russ. J. Phys. Chem. 52 (1978) 968–970.

[105] A.N.M. E.N. Eremin, V.M. Belova, Heterogeneous catalytic oxidation ofnitrogen in a glow discharge III. N_2:O_2∼1:4 nitrogen-oxygen mixture, Russ. J. Phys. Chem. 52 (1978) 970–972.

[106] D.S.P. Franco, J.L.S. Fagundes, J. Georgin, N.P.G. Salau, G.L. Dotto, A mass transfer study considering intraparticle diffusion and axial dispersion for fixed-bed adsorption of crystal violet on pecan pericarp (Carya illinoensis), Chem. Eng. J. 397 (2020) 125423. https://doi.org/10.1016/j.cej.2020.125423.

[107] A.H. Sulaymon, K.W. Ahmed, Competitive adsorption of furfural and phenolic compounds onto activated carbon in fixed bed column, Environ. Sci. Technol. 42 (2008) 392–397. https://doi.org/10.1021/es070516j.

[108] W. Reynolds, H. Singer, S. Schug, I. Smirnova, Hydrothermal flow-through treatment of wheat-straw: Detailed characterization of fixed-bed properties and axial dispersion, Chem. Eng. J. 281 (2015) 696–703. https://doi.org/10.1016/j.cej.2015.06.117.

[109] P.G. Aguilera, F.J. Gutiérrez Ortiz, Prediction of fixed-bed breakthrough curves for H_2S adsorption from biogas: Importance of axial dispersion for design, Chem. Eng. J. 289 (2016) 93–98. https://doi.org/10.1016/j.cej.2015.12.075.

[110] A. Bittante, J. García-Serna, P. Biasi, F. Sobrón, T. Salmi, Residence time and axial dispersion of liquids in Trickle Bed Reactors at laboratory scale, Chem. Eng. J. 250 (2014) 99–111. https://doi.org/10.1016/j.cej.2014.03.062.

[111] M. V. Ferreira, A.M. Ribeiro, J.M. Loureiro, Experimental and simulation studies of TAME synthesis in a fixed-bed reactor, Ind. Eng. Chem. Res. 46 (2007) 1105–1113. https://doi.org/10.1021/ie060788f.

[112] J. Voggenreiter, A. Ferre, J. Burger, Scale-up of the Continuous Production of Poly(oxymethylene) Dimethyl Ethers from Methanol and Formaldehyde in Tubular Reactors, 61 (2022) 10034–10046. https://doi.org/10.1021/acs.iecr.2c01468.

[113] G. He, Performance degradation and recovery of YSZ membrane under the sulphuric acid

thermal decomposition, The university of Sheffield, 2013.

[114] H. Falsig, J. Shen, T.S. Khan, W. Guo, G. Jones, S. Dahl, T. Bligaard, On the structure sensitivity of direct NO decomposition over low-index transition metal facets, Top. Catal. 57 (2014) 80–88. https://doi.org/10.1007/s11244-013-0164-5.

[115] C.E. Treanor, J.W. Rich, R.G. Rehm, Vibrational relaxation of anharmonic oscillators with exchange-dominated collisions, J. Chem. Phys. 48 (1968) 1807–1813. https://doi.org/10.1063/1.1668914.

[116] A. Ricard, J.P. Sarrette, S.G. Oh, Y.K. Kim, Comparison of the Active Species in the RF and Microwave Flowing Discharges of N_2 and Ar–20 % N_2, Plasma Chem. Plasma Process. 36 (2016) 1559–1570. https://doi.org/10.1007/s11090-016-9739-9.

[117] P. Mehta, P. Barboun, F.A. Herrera, J. Kim, P. Rumbach, D.B. Go, J.C. Hicks, W.F. Schneider, Overcoming ammonia synthesis scaling relations with plasma-enabled catalysis, Nat. Catal. 1 (2018) 269–275. https://doi.org/10.1038/s41929-018-0045-1.

[118] A.I.O. Mario Capitelli, Carlos M. Ferreira, Boris F. Gordiets, Plasma Kinetics in Atmospheric Gases, 31st ed., Springer-Verlag Berlin Heidelberg, 2000. https://link.springer.com/book/10.1007/978-3-662-04158-1.

[119] J. Zeldovich, The oxidation of nitrogen in combustion and explosions, Eur. Phys. J. A. Hadron. Nucl. 21 (1946) 577–628.

[120] J. Nahorny, C.M. Ferreira, B. Gordietsi, D. Pagnon, M. Touzeau, M. Vialle, Experimental and theoretical investigation of a N_2-O_2 DC flowing glow discharge, J. Phys. D. Appl. Phys. 28 (1995) 738. https://doi.org/10.1088/0022-3727/28/4/017.

[121] C.D. Pintassilgo, J. Loureiro, V. Guerra, Modelling of a N_2-O_2 flowing afterglow for plasma sterilization, J. Phys. D. Appl. Phys. 38 (2005) 417–430. https://doi.org/10.1088/0022-3727/38/3/011.

[122] K. Kutasi, C.D. Pintassilgo, J. Loureiro, P.J. Coelho, Active species in a large volume N_2-O_2 post-discharge reactor, J. Phys. D. Appl. Phys. 40 (2007) 1990–2001. https://doi.org/10.1088/0022-3727/40/7/022.

[123] S. De Benedictis, G. Dilecce, Time resolved diagnostics for kinetic studies in N_2/O_2 pulsed RF discharges, J. Phys. III. 6 (1996) 1189–1204. https://doi.org/10.1051/jp3:1996178.

[124] A. Ricard, J.P. Sarrette, B. Jeon, Y.K. Kim, Discharge source-dependent variation in the densities of active species in the flowing afterglows of N_2 RF and UHF plasmas, Curr. Appl. Phys. 17 (2017) 945–950. https://doi.org/10.1016/j.cap.2017.04.006.

[125] E. Kemaneci, J.P. Booth, P. Chabert, J. Van Dijk, T. Mussenbrock, R.P. Brinkmann, A computational analysis of the vibrational levels of molecular oxygen in low-pressure

stationary and transient radio-frequency oxygen plasma, Plasma Sources Sci. Technol. 25 (2016) 25025. https://doi.org/10.1088/0963-0252/25/2/025025.

[126] P. Vašina, V. Kudrle, A. Tálský, P. Botoš, M. Mrázková, M. Meško, Simultaneous measurement of N and O densities in plasma afterglow by means of NO titration, Plasma Sources Sci. Technol. 13 (2004) 668–674. https://doi.org/10.1088/0963-0252/13/4/016.

[127] V. Chandra, D. Vogels, E.A.J.F. Peters, J.A.M. Kuipers, A multi-scale model for the Fischer-Tropsch synthesis in a wall-cooled packed bed reactor, Chem. Eng. J. 410 (2021) 128245. https://doi.org/10.1016/j.cej.2020.128245.

[128] H. Harode, M. Ramteke, Axial dispersion modeling of industrial hydrocracking unit and its multiobjective optimization, Chem. Eng. Res. Des. 121 (2017) 57–68. https://doi.org/10.1016/j.cherd.2017.02.033.

[129] M.J. Palys, A. McCormick, E.L. Cussler, P. Daoutidis, Modeling and optimal design of absorbent enhanced ammonia synthesis, Processes. 6 (2018) 91. https://doi.org/10.3390/PR6070091.

[130] I. Krop, J.; Pollo, I. Chemical reactors for synthesis of nitrogen oxide in a stream of low-temperature plasma. III. Reactor to freeze reaction products by injection of water., Chemia. 678 (1981) 51–59.

[131] W. Bian, X. Song, J. Shi, X. Yin, Nitrogen fixed into HNO_3 by pulsed high voltage discharge, J. Electrostat. 70 (2012) 317–326. https://doi.org/10.1016/j.elstat.2012.03.010.

[132] H. Patel, R.K. Sharma, V. Kyriakou, A. Pandiyan, S. Welzel, M.C.M. van de Sanden, M.N. Tsampas, Plasma-Activated Electrolysis for Cogeneration of Nitric Oxide and Hydrogen from Water and Nitrogen, ACS Energy Lett. 4 (2019) 2091–2095. https://doi.org/10.1021/acsenergylett.9b01517.

[133] A. V Pipa, T. Bindemann, R. Foest, E. Kindel, J. Röpcke, K.-D. Weltmann, Absolute production rate measurements of nitric oxide by an atmospheric pressure plasma jet (APPJ), J. Phys. D. Appl. Phys. 41 (2008) 194011. https://doi.org/10.1088/0022-3727/41/19/194011.

[134] X. Pei, D. Gidon, Y.-J. Yang, Z. Xiong, D.B. Graves, Reducing energy cost of NO production in air plasmas, Chem. Eng. J. 362 (2019) 217–228. https://doi.org/10.1016/j.cej.2019.01.011.

[135] B.S. Patil, N. Cherkasov, J. Lang, A.O. Ibhadon, V. Hessel, Q. Wang, Low temperature plasma-catalytic NO_x synthesis in a packed DBD reactor: Effect of support materials and supported active metal oxides, Appl. Catal. B Environ. 194 (2016) 123–133. https://doi.org/10.1016/j.apcatb.2016.04.055.

[136] A.A. Abdelaziz, H.-H. Kim, Temperature-dependent behavior of nitrogen fixation in

nanopulsed dielectric barrier discharge operated at different humidity levels and oxygen contents, J. Phys. D. Appl. Phys. 53 (2020) 114001. https://doi.org/10.1088/1361-6463/ab5c78.

[137] D. Rapakoulias, S. Cavadias, J. Amouroux, Catalytic processes in a non-equilibrium plasma reactor II. Nitrogen fixation in the N_2-O_2 system, Rev. Phys. Appl. 15 (1980) 1261–1265. https://doi.org/DOI: 10.1051/rphysap:019800015070126100.

[138] E. Vervloessem, Y. Gorbanev, A. Nikiforov, N. De Geyter, A. Bogaerts, Sustainable NO_x production from air in pulsed plasma: elucidating the chemistry behind the low energy consumption, Green Chem. 24 (2022) 916–929. https://doi.org/10.1039/D1GC02762J.

[139] M. Janda, V. Martišovitš, K. Hensel, Z. Machala, Generation of Antimicrobial NO_x by Atmospheric Air Transient Spark Discharge, Plasma Chem. Plasma Process. 36 (2016) 767–781. https://doi.org/10.1007/s11090-016-9694-5.

[140] M.J. Pavlovich, T. Ono, C. Galleher, B. Curtis, D.S. Clark, Z. Machala, D.B. Graves, Air spark-like plasma source for antimicrobial NO_x generation, J. Phys. D. Appl. Phys. 47 (2014) 505202. https://doi.org/10.1088/0022-3727/47/50/505202.

[141] B.S. Patil, F.J.J. Peeters, G.J. van Rooij, J.A. Medrano, F. Gallucci, J. Lang, Q. Wang, V. Hessel, Plasma assisted nitrogen oxide production from air: Using pulsed powered gliding arc reactor for a containerized plant, AIChE J. 64 (2018) 526–537. https://doi.org/https://doi.org/10.1002/aic.15922.

[142] W. Wang, B. Patil, S. Heijkers, V. Hessel, A. Bogaerts, Nitrogen Fixation by Gliding Arc Plasma: Better Insight by Chemical Kinetics Modelling, ChemSusChem. 10 (2017) 2110. https://doi.org/https://doi.org/10.1002/cssc.201700611.

[143] I. Tsonev, C. O'Modhrain, A. Bogaerts, Y. Gorbanev, Nitrogen Fixation by an Arc Plasma at Elevated Pressure to Increase the Energy Efficiency and Production Rate of NO_x, ACS Sustain. Chem. Eng. 11 (2023) 1888–1897. https://doi.org/10.1021/acssuschemeng.2c06357.

[144] X. Hao, A.M. Mattson, C.M. Edelblute, M.A. Malik, L.C. Heller, J.F. Kolb, Nitric Oxide Generation with an Air Operated Non-Thermal Plasma Jet and Associated Microbial Inactivation Mechanisms, Plasma Process. Polym. 11 (2014) 1044–1056. https://doi.org/https://doi.org/10.1002/ppap.201300187.

[145] R. Ingels, Energy efficient process for producing nitrogen oxide, Norw, Norway, 2012.

[146] X.Y. Lei, H. Cheng, L.L. Nie, X.P. Lu, Nitrogen Fixation as NO_x Enabled by a Three-Level Coupled Rotating Electrodes Air Plasma at Atmospheric Pressure, Plasma Chem. Plasma Process. 42 (2022) 211–227. https://doi.org/10.1007/s11090-021-10222-2.

[147] S. Kelly, A. Bogaerts, Nitrogen fixation in an electrode-free microwave plasma, Joule. 5

(2021) 3006–3030. https://doi.org/10.1016/j.joule.2021.09.009.

[148] X. Pei, D. Gidon, D.B. Graves, Specific energy cost for nitrogen fixation as NO_x using DC glow discharge in air, J. Phys. D. Appl. Phys. 53 (2020). https://doi.org/10.1088/1361-6463/ab5095.

[149] P.R. Ammann, R.S. Timmins, Chemical reactions during rapid quenching of oxygen-nitrogen mixtures from very high temperatures, AIChE J. 12 (1966) 956–963. https://doi.org/10.1002/aic.690120522.

[150] B.S. Patil, Q. Wang, V. Hessel, J. Lang, Plasma N_2-fixation: 1900–2014, Catal. Today. 256 (2015) 49–66. https://doi.org/https://doi.org/10.1016/j.cattod.2015.05.005.

[151] S. Van Alphen, H.A. Eshtehardi, C. O'Modhrain, J. Bogaerts, H. Van Poyer, J. Creel, M.-P. Delplancke, R. Snyders, A. Bogaerts, Effusion nozzle for energy-efficient NO_x production in a rotating gliding arc plasma reactor, Chem. Eng. J. 443 (2022) 136529. https://doi.org/10.1016/j.cej.2022.136529.

[152] Y.P. Raizer, Gas discharge physics, Springer-Verlag Berlin Heidelberg, Berlin, 1991.

[153] G. V Naidis, Simulation of convection-stabilized low-current glow and arc discharges in atmospheric-pressure air, Plasma Sources Sci. Technol. 16 (2007) 297. https://doi.org/10.1088/0963-0252/16/2/012.

[154] S.A. Wutzke, E. Pfender, E.R.G. Eckert;, Study of electric arc behavior with superimposed flow., AIAA J. 5 (1967) 707–713. https://doi.org/10.2514/3.4051.

[155] J.P. Trelles, E. Pfender, J. Heberlein, Multiscale Finite Element Modeling of Arc Dynamics in a DC Plasma Torch, Plasma Chem. Plasma Process. 26 (2006) 557–575. https://doi.org/10.1007/s11090-006-9023-5.

[156] COMSOL Multiphysics® v. 6.0, COMSOL AB: Stockholm, Sweden., (n.d.).

[157] B.J.. McBride, M.J.. Zehe, S.Gordon, NASA Glenn Coefficients for Calculating Thermodynamic Properties of Individual Species; National Aeronautics and Space Administration, Cleveland, MD, USA, 2002.

[158] N L Aleksandrov, E M Bazelyan, I V Kochetov, N A Dyatko, The ionization kinetics and electric field in the leader channel in long air gaps, J. Phys. D. Appl. Phys. 30 (1997) 1616. https://doi.org/10.1088/0022-3727/30/11/011.

[159] D.L. Baulch, C.T. Bowman, C.J. Cobos, R.A. Cox, T. Just, J.A. Kerr, M.J. Pilling, D. Stocker, J. Troe, W. Tsang, R.W. Walker, J. Warnatz, Evaluated Kinetic Data for Combustion Modeling: Supplement II, J. Phys. Chem. Ref. Data. 34 (2005) 757–1397. https://doi.org/10.1063/1.1748524.

[160] Z. Machala, C. Laux, C. Kruger, G. Candler, Atmospheric air and nitrogen DC glow discharges with thermionic cathodes and swirl flow, in: 42nd AIAA Aerosp. Sci. Meet. Exhib., American Institute of Aeronautics and Astronautics, 2004. https://doi.org/doi:10.2514/6.2004-355.

[161] I. Tsonev, J. Boothroyd, S. Kolev, A. Bogaerts, Simulation of glow and arc discharges in nitrogen: effects of the cathode emission mechanisms, Plasma Sources Sci. Technol. 32 (2023) 54002. https://doi.org/10.1088/1361-6595/acc96c.

[162] S. Eyde, Oxidation of Atmospheric Nitrogen and Development of Resulting Industries in Norway., J. Ind. Eng. Chem. 4 (1912) 771–774. https://doi.org/10.1021/ie50046a025.

[163] K. Birkeland, On the oxidation of atmospheric nitrogen in electric arcs, Trans. Faraday Soc. 2 (1906) 98–116. https://doi.org/10.1039/TF9060200098.

[164] F.A. D'Isa, E.A.D. Carbone, A. Hecimovic, U. Fantz, Performance analysis of a 2.45 GHz microwave plasma torch for CO_2 decomposition in gas swirl configuration, Plasma Sources Sci. Technol. 29 (2020) 105009. https://doi.org/10.1088/1361-6595/abaa84.

[165] F.M. PERKIN, The Oxidation of Atmospheric Nitrogen in the Electric Arc, Nature. 74 (1906) 444–446. https://doi.org/10.1038/074444c0.

[166] L. Chiappetta, M.B. Colket III, Design Considerations for Aerodynamically Quenching Gas Sampling Probes, J. Heat Transfer. 106 (1984) 460–466. https://doi.org/10.1115/1.3246694.

[167] T.B. J.K. Norskov, F. studt, F. Abild-pedersen, Fundamental Concepts in Heterogeneous Catalysis, Wiley & Sons, 2014.

[168] M.W. Chase Jr., NIST-JANF Thermochemical Tables, National Institute of Standards and Technology, New York, 1998.

[169] J.K. Nørskov, T. Bligaard, A. Logadottir, S. Bahn, L.B. Hansen, M. Bollinger, H. Bengaard, B. Hammer, Z. Sljivancanin, M. Mavrikakis, Y. Xu, S. Dahl, C.J.H. Jacobsen, Universality in heterogeneous catalysis, J. Catal. 209 (2002) 275–278. https://doi.org/10.1006/jcat.2002.3615.

[170] H. Ma, W.F. Schneider, Structure- and Temperature-Dependence of Pt-Catalyzed Ammonia Oxidation Rates and Selectivities, ACS Catal. 9 (2019) 2407–2414. https://doi.org/10.1021/acscatal.8b04251.

[171] A. Bajpai, P. Mehta, K. Frey, A.M. Lehmer, W.F. Schneider, Benchmark First-Principles Calculations of Adsorbate Free Energies, ACS Catal. 8 (2018) 1945–1954. https://doi.org/10.1021/acscatal.7b03438.

[172] K.K. Irikura, Experimental vibrational zero-point energies: Diatomic molecules, J. Phys. Chem. Ref. Data. 36 (2007) 389–397. https://doi.org/10.1063/1.2436891.

List of publications

As first author

1. **H. Ahmadi Eshtehardi***, S. Van Alphen*, C. O'Modhrain, J. Bogaerts, H. Van Poyer, J. Creel, M.-P. Delplancke, R. Snyders, A. Bogaerts, Effusion nozzle for energy-efficient NO_x production in a rotating gliding arc plasma reactor, Chem. Eng. J. 443 (2022) 136529. https://doi.org/10.1016/j.cej.2022.136529. (* shared first authors)

2. **H. Ahmadi Eshtehardi**, K. Van 't Veer, M.-P. Delplancke, F. Reniers, A. Bogaerts, Postplasma Catalytic Model for NO Production: Revealing the Underlying Mechanisms to Improve the Process Efficiency, ACS Sustain. Chem. Eng. 11 (2023) 1720 - 1733, https://doi.org/10.1021/acssuschemeng.2c05665.

3. **H. Ahmadi Eshtehardi***, I. Tsonev*, M.P. Delplancke, A. Bogaerts, Scaling up energy-efficient plasma-based nitrogen fixation, Sustain. Energy & Fuels (submitted in Dec. 2023). (* shared first authors)

As Co-author

4. F. Jardali, S. Van Alphen, J. Creel, **H. Ahmadi Eshtehardi**, M. Axelsson, R. Ingels, R. Snyders, A. Bogaerts, NO_x production in a rotating gliding arc plasma: potential avenue for sustainable nitrogen fixation, Green Chem. 23 (2021) 1748 – 1757, https://doi.org/10.1039/D0GC03521A.

Conference contributions

- Poster presentation at Solvay workshop on Plasma Technology and Other Green Methods for Nitrogen Fixation, Brussels, Belgium (Nov. 2021), presenting, "NO_x production in a rotating gliding arc plasma reactor: potential avenue for sustainable nitrogen fixation".

- Poster presentation at Solvay workshop on Plasma Technology and Other Green Methods for Nitrogen Fixation, Brussels, Belgium (Nov. 2021), presenting, "Effusion nozzle for energy efficient NO_x production in rotating gliding arc plasma reactor".

- Oral presentation at the International Conference on Plasma Surface Engineering (PSE) 2022, Erfurt, Germany (Sep. 2022), presenting "Effusion nozzle for energy efficient NO_x production in rotating gliding arc plasma reactor".

Patent application

- J. Creel, H. Ahmadi Eshtehardi, A. Bogaerts, Plasma reactor for plasma-based gas conversion comprising an effusion nozzle, World Intellectual Property Organization (WIPO), 2022, IP-No: WO 2022/234039 A1, 2022. https://data.epo.org/publication-server/document?iDocId=6952518&iFormat=0.

Other activities

Thesis supervision

- Supervisor for the bachelor's thesis of Helder Van Poyer at PLASMANT (2021)